Photolithographic and Replication Techniques for Nanofabrication and Photonics

A thesis submitted in fulfillment of the requirements for the degree of Doctor of Philosophy

Gorgi Kostovski
B.Eng. / B.App.Sci.

School of Electrical and Computer Engineering
Science, Engineering and Technology Portfolio
RMIT University
March 2008

Declaration

I certify that except where due acknowledgement has been made, the work is that of the author alone; the work has not been submitted previously, in whole or in part, to qualify for any other academic award; the content of the thesis is the result of work which has been carried out since the official commencement date of the approved research program; and, any editorial work, paid or unpaid, carried out by a third party is acknowledged.

Gorgi Kostovski

Abstract

In the pursuit of economical and rapid fabrication solutions on the micro and nano scale, polymer replication has proven itself to be a formidable technique, which despite zealous development by the research community, remains full of promise.

This thesis explores the potential of elastomers in what is a distinctly multidisciplinary field. The focus is on developing innovative fabrication solutions for planar photonic devices and for nanoscale devices in general. Innovations are derived from treatments of master structures, imprintable substrates and device applications.

Major contributions made by this work include fully replicated planar integrated optical devices, nanoscale applications for photolithographic standing wave corrugations (SWC), and a biologically templated, optical fiber based, surface-enhanced Raman scattering (SERS) sensor. The planar devices take the form of dielectric rib waveguides which for the first time, have been integrated with long-period gratings by replication. The heretofore unemployed SWC is used to demonstrate two innovations. The first is a novel demonstration of elastomeric sidewall photolithographic mask, which exploits the capacity of elastomers to cast undercut structures. The second demonstrates that the corrugations themselves in the absence of elastomers, can be employed as shadow masks in a directional flux to produce vertical stacks of straight lines and circles of nanowires and nanoribbons. The thesis then closes by conceptually combining the preceding demonstrations of waveguides and nanostructures. An optical fiber endface is employed for the first time as a substrate for patterning by replication, wherein the pattern is a nanostructure derived from a biological template. This replicated nanostructure is used to impart a SERS capability to the optical fiber, demonstrating an ultra-sensitive, integrated photonic device realized at great economy of both time and money, with very real potential for mass fabrication.

Acknowledgements

I would like to take this opportunity to express my sincerest gratitude to all of the people who have supported me in my pursuit of this degree.

Foremost, my thanks go to my supervisors. Professor Michael Austin provided me with this research opportunity and supervised my activities, while Dr Anthony Holland gave me my introduction to photolithography and provided valuable technical support. My deepest gratitude goes to Associate Professor Arnan Mitchell for his inspiring discussions and invaluable introductions, to both people and ideas, which opened doors to fascinating areas of research. To all, thank you for giving me the freedom to explore and develop my own ideas.

I thank Dr Paul Stoddart and Daniel White of Swinburne University, for welcoming me into their labs and for providing an introduction to SERS and cicadas. Their assistance with performing SERS measurements was invaluable.

My thanks also go to Paul Jones and Miroslav Milajnic, for their friendship, their instruction in clean-room procedure and for their dogged enforcement of clean-room protocol. My gratitude also goes to Mr Yuxun Cao for his endless technical support and maintenance of equipment, and to Phil Francis from our Microscopy facility, for his assistance and instruction.

For their steadfast friendship and camaraderie, I would like to thank fellow students and colleagues Ernest Fardin, Vijay Sivan, Andreas Perentos, Simon Mutzenich and Lam Bui. My appreciation also goes to Sharath, Madhu, Damien, Jayantha, Yuvaraja, Eika, Geeth, Shumitra, Hossein, Dean and Thach for helping to generate a lively, welcoming and intellectually stimulating research environment.

To my friend Paul Hubbard, I am deeply indebted for his companionship and for providing me with the inspiration to pursue this degree.

Finally and most importantly, my deepest gratitude goes to my parents Nick and Zora, and to my brother and sister, Petar and Marija, They have provided me with all manner of support throughout my life, and have shown me unconditional love and patience. I dedicate this thesis to them.

Contents

Table of Symbols and Abbreviations

Symbols

Λ	Grating period
n	Refractive index
λ	Optical wavelength

Abbreviations and Acronyms

BCB	Benzocyclobutene
CCD	Charge Coupled Device
CWDM	Coarse Wavelength Division Multiplexing
DI	De-ionized
DRIE	Deep Reactive Ion Etching
h-PDMS	hard polydimethylsiloxane
HEPA	High Efficiency Particulate Air
HMDS	Hexamethyldisilazane
ICP	Inductively Coupled Plasma
LPG	Long Period Grating
LPWG	Long Period Waveguide Grating
PDMS	Polydimethylsiloxane
PM	Polarization Maintaining
PMMA	Polymethylmethacrylate
RIE	Reactive Ion Etching
rpm	revolutions per minute
s-PDMS	soft polydimethylsiloxane
SAM	Self Assembled Monolayer
SEM	Scanning Electron Microscope
SERS	Surface-Enhanced Raman Scattering
SMSERS	Single Molecule Surface-Enhanced Raman Scattering
SWC	Standing Wave Corrugations
TE	Transverse Electric
UV	Ultra-Violet

List of Figures

Chapter 1.

Introduction

1.1 Introduction

Commercial micro and nano-fabrication is presently dominated by photolithographic and beam steering techniques. The former is the work-horse of the semiconductor industry, and can be traced through successive generations back to the 1960's, while beam steering techniques are represented by such tools as electron beam lithography and focused ion-beam milling. Both of these classes of fabrication derive their dominance of this field from their impressive resolutions, which are presently in the range of 10s of nanometers.

However, the routine application of these techniques outside of the semiconductor industry is rather restricted. Their expense prevents them from being employed in environments such as small research labs, while the mechanisms by which they perform patterning make them unsuited to many applications. The serial nature of beam steering for instance, limits its usefulness to prototyping, while many of the steps inherent to both are too severe for the patterning of delicate biological materials.

As a result, the past decade has seen the development of many alternative micro and nano fabrication techniques. One approach that has been gathering momentum in research communities is that of polymer replication. The fundamental concept behind this approach is the use of surface relief molds to quickly and economically replicate a

surface relief master structure. This replication can be implemented via a process of stamping, masking or molding, and is represented by techniques such as soft lithography, hot embossing and nanoimprint lithography.

Conceptually, polymer replication is one of the simplest fabrication techniques available, and yet it offers extraordinarily high resolution, often exceeding that offered by photolithography and beam steering. This high resolution is derived mostly from material properties, since it is not hampered by optical diffraction limits such as those that limit photolithography. Additionally, much of the cost that is commonly associated with such precise fabrication is absent from replication. This is because the use of expensive high resolution techniques such as beam steering is limited to the fabrication of a single master template, while the replication steps themselves incur little to no overhead costs or operational expense.

This combination of conceptual simplicity and low cost makes replication a highly accessible technique. It has readily found application in fields as diverse as electronics, photonics and biology. When considered together with their impressive resolution and parallel approach to fabrication, it is easy to understand why they are widely considered contenders for next-generation lithography technique. However for the present time, many replication techniques fall within the more general class of 'unconventional' nanofabrication techniques. This broad class of techniques shares a philosophy of simplicity and low cost, while delivering exceptional resolution. It is this ideology which best describes the undertakings of this thesis.

1.2 Thesis overview

The aim of this thesis is to explore and develop the potential of elastomer based replication techniques by investigating opportunities in device applications, master template fabrication, biological templates and choices of imprintable substrate. This thesis consists of six chapters and one appendix. A brief summary of each is given as follows.

Chapter 2 gives a brief overview of the micro/nano replication techniques in use today, and discusses their merits and limitations. The pursuit of elastomer based replication techniques throughout this thesis is justified here.

Chapter 3 serves as an introduction to micro/nano fabrication, and demonstrates the use of photolithography for fabricating master structures, and soft imprint lithography for fabricating planar optical devices. A single step imprint is used to first demonstrate planar, polymer rib waveguides, after which a two step imprinting process is used to integrate the waveguides with long period gratings, which enable the waveguides to perform wavelength rejection. Optical mode profiles are presented to demonstrate the functionality of the waveguides, while a transmission spectrum is used to demonstrate optical resonance of the waveguide grating device. This demonstrates for the first time the fabrication of a planar long-period waveguide grating structure by replication.

Chapter 4 makes the transition from micron scale structures to nanoscale fabrication, and does so by identifying a nanoscale artifact in photolithographically produced master patterns. These artifacts are the standing wave corrugations that are native to photolithography. Two novel nanolithography techniques are demonstrated by exploiting these artifacts. The first employs the nanoscale depths of the corrugations, and is reliant on the capacity of elastomers to cast undercut structures. The sidewall corrugations are thus transferred to a PDMS bulk where they are used to intercept and scatter incident light, demonstrating a novel elastomeric edge-lithography mask. In the second technique, the nanoscale offsets of the corrugations relative to one another are employed to demonstrate even smaller features than the first technique. Here, the vertically stacked corrugations are used as shadow masks in the path of an incident flux of evaporated material, to produce vertical stacks of straight lengths and circles of nanowires and nanoribbons. This technique stands independent of elastomers, however the potential exists for its transfer to an elastomeric platform. Analysis with a scanning electron microscope demonstrates that the first technique is capable of photoresist features as small as 80 nm, while the second is capable of 16 nm.

Chapter 5 draws the thesis to a close by conceptually combining the preceding demonstrations of waveguides and nanostructures. An optical fiber is employed as an analog to planar waveguides, and its endface is used for the first time as a substrate for patterning by replication. This demonstrates a novel platform for replication which inherently allows for optical interrogation. The replicated pattern is derived from a nanostructured biological template, in accordance with the spartan philosophy of

unconventional nanofabrication techniques. The directional deposition of silver is then used to impart a SERS capability to the optical fiber. This demonstration attempts to address the market need for an affordable, robust SERS sensor by demonstrating an ultra sensitive implementation that has been realized at great economy of both time and money. Additionally, the size disparity between mold and endface presents the very real potential for mass fabrication. SERS spectra are provided as proof of functionality. These are acquired by performing a through-fiber interrogation of the imprinted endface, on which is adsorbed a monolayer analyte.

A closing chapter then summarizes the work undertaken in this thesis, and the conclusions that have been drawn. The potential for future work is then briefly discussed.

1.3 Original contributions made by this thesis

The original contributions made by this thesis are:

- Replicated planar optical devices:
    - Fabrication of single-mode shallow-rib polymer waveguides using soft imprint lithography.
    - Fabrication and demonstration of a soft imprinted long period waveguide grating device.
- Demonstration of the utility of photolithographic standing wave corrugations:
    - A novel nanoscale PDMS edge-photolithography mask that derives 80 nm line-widths from micron sized photoresist features.
    - A novel three dimensional nanofabrication technique that derives vertical stacks of nanowires, nanoribbons and nanorings with widths as narrow as 16 nm from micron scale photoresist features.
- A novel implementation of an optical fiber SERS sensor:
    - Application of nanoimprint lithography to the endface of an optical fiber.
    - Derivation of a functional optical fibre SERS device from a biological nanostructure.

Chapter 2.

Replication Overview

2.1 Introduction

The polymer replication techniques employed in this thesis are all derived from the use of elastomers. However elastomeric replication techniques are only one branch of a larger collective of micro and nanoscale polymer replication techniques. These are divided into three general categories – soft imprinting, hot embossing and nanoimprint lithography. This chapter will give a brief overview of these general classes of polymer replication in use today, for the purpose of contextualizing the work in this thesis.

2.2 Overview of replication techniques

Replicating a surface relief pattern into a bulk or thin film material is achieved by the selective displacement of material. In achieving this displacement, the concept that is common to soft imprinting, hot embossing and nanoimprint lithography is their use of high precision surface relief molds. These molds retain their structural integrity during imprinting, while the imprinted material acquiesces to the molds topography and retains it after the mold is removed, as illustrated in Figure 2.1. Where the aforementioned

techniques diverge is in the mold materials that they use, which in turn dictate the manner in which the molds are applied and the materials that they can be applied to.

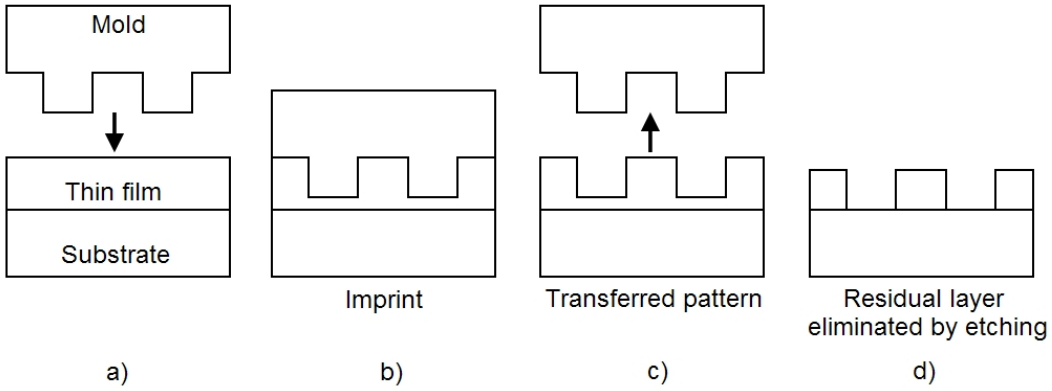

Figure 2.1: Illustration of a generic imprinting process, where a mold pattern is replicated into a thin film.

Soft imprint lithography, in its most general definition describes the use of soft mold materials, which are typically elastomers, to imprint liquid monomer solutions. The most common elastomer in use today is polydimethylsiloxane (PDMS), with a modulus of ~2 N/mm^2 [1]. PDMS is commercially available from Dow Corning as Sylgard 184 Elastomer, however alternatives with different rigidities and resolutions have been formulated [2,3]. The nomenclature 'soft' can be extended to describe the conditions of imprinting, wherein the liquid polymer flows to fill the mold without the application of high pressures. This is a critical limitation, since high imprinting pressures would result in mold compression.

Hot embossing is typified by the use of rigid mold materials and is in many ways the converse of soft imprinting. Here, high pressures are used to emboss materials that have been thermally softened [4], wherein higher temperatures result in greater reduction of material viscosity and thus less resistance to deformation. However upper limits are placed on this temperature by thermal expansion coefficients and material evaporation.

Nanoimprint lithography (NIL) was originally demonstrated by Chou [5] as a thermal technique akin to hot embossing. Today this name is largely used as an umbrella term to describe any imprinting technique that produces nanoscale features. It is thus not uncommon to see this name applied to instances of soft imprinting and hot embossing.

Other titles that fall under the banner of NIL, and may overlap with soft imprinting and hot embossing, include ultra-violet nanoimprint lithography, thermal imprinting and laser assisted direct imprinting. The latter technique uses rigid molds to imprint challenging materials such as silicon [6]. Other materials that have been imprinted by rigid molds include glass, quartz [7] and aluminium [8].

2.3 Fabrication of molds

The methods for fabricating molds largely depends on the mold material that is being used. The typical route is to first create a surface relief master pattern, and to then cast a mold against it.

For PDMS, this is a very simple process which consists of preparing a liquid PDMS solution, pouring it over the master structure, and then thermally curing it. In the case of a rigid mold material, the master pattern can be coated with a metallic seed layer and then back-plated by electroplating to create a metallic mold [9], typically of nickel. This process is more involved than the elastomeric case since it requires the use of vacuum coating systems and electroplating chemicals. An alternative is to use the master pattern itself as a mold, wherein an appropriate material such as silicon [10] or quartz [6] is patterned directly. Transparent mold materials such as quartz allow optical illumination to be employed in the imprinting process, for purposes such as optical curing [11] and alignment.

2.4 Benefits and challenges associated with molds

The manner in which these elastomeric and rigid molds are applied to imprinting is a source of further differentiation. Elastomeric casts, in particular PDMS, are possessed of a fortuitous combination of material properties that lead to a very simple imprinting process. Concerns such as the careful handling of molds before and during imprinting in order to avoid mechanical damage, and the contamination of the mold by residual imprinted material are almost completely eliminated by the use of PDMS. This is because its pliability allows it to deform elastically in most scenarios, in particular during separation from master and imprinted structures, without sustaining or imparting damage,

while its low surface energy of ~21.6 dyn/cm [3] and its general chemical inertness mean that it releases easily from a large range of polymers with little chance of contamination. This has resulted in the majority of PDMS imprinting being performed by hand, eliminating the need for an imprinting press. Additionally, its optical transparency down to ~300 nm [12] makes it very well suited to patterning optically curable polymers.

Rigid molds on the other hand require careful and precise handling to avoid mechanical damage before and during the replication process. They also require the addition of anti-adhesion layers [13], either on the mold itself or on the imprintable material, to facilitate separation after imprinting. Additionally, commercial mechanical presses are commonly employed in order to achieve precise control of thermal energy and to uniformly distribute forces [14]. However, this account is not intended to discount the use of rigid molds entirely. Other than being applicable to a range of challenging materials that are not accessible to soft molds, rigid molds are significantly more amenable to alignment with existing structures than flexible elastomers, and they are not subject to the surface tension problems associated with flexible materials, which can result in corner rounding.

2.5 Applications of molds

Regardless of whether a rigid or soft mold is used, patterning by imprinting produces surface relief features rather than discrete features. This is characterized by the presence of residual material in between features, which may be acceptable for applications such as optical structures and microfluidics, but is problematic if the intention is to transfer the imprinted pattern to substrate layers. In this case, a directional etching technique is employed as a post-imprinting step to remove this residual layer [15], as illustrated in Figure 2.1d.

However, the applications of imprint molds extend far beyond the creation of surface relief features and etch masks. This versatility is especially evident in the myriad uses that elastomeric molds have demonstrated, as derived form their material properties. To begin with, the flexibility of these molds allows them to deform to accommodate substrates. This localizes the impact of particulate contaminants on the one hand, while allowing for the patterning [16] and even the creation of nonplanar substrates [17] on the

other. This mechanical flexibility also allows for the casting and replication of undercut structures [18], which would otherwise lock rigid molds in place. When the transparency of PDMS is exploited, a mold can be used as a photolithographic mask. These masks automatically achieve conformal contact with photoresist, providing mechanical mating of unparalleled stability, while posing little risk of damage due to abrasion, as well as providing access to the optical near field of the mask [19]. Finally, when the low surface energy of the elastomer is exploited, molds can be readily employed as stamps to transfer material which most often prefers to adhere to surfaces other than the PDMS [20]. This collection of applications is commonly referred to as Soft Lithography [21].

2.6 Conclusions

It is clear that both rigid and soft molds offer advantages and limitations in their approaches to replication. However from the perspective of simplicity, versatility and accessibility, elastomeric molds are arguably superior. It is precisely this simplicity and versatility that has made elastomers an attractive candidate for the work in this thesis.

In the chapters that follow, more specific and in-depth literature reviews will be conducted in relation to the material at hand.

2.7 References

1. T. W. Odom, J. C. Love, D. B. Wolfe, K. E. Paul, G. M. Whitesides, *Improved pattern transfer in soft lithography using composite stamps*, Langmuir, 18, p. 5314, 2002.
2. F. Hua, Y. Sun, A. Gaur, M. A. Meitl,, L. Bilhaut, L. Rotkina, J. Wang, P. Geil, M. Shim and J. A. Rogers, *Polymer imprint lithography with molecular-scale resolution*, Nano Letters, 4, p. 2467, 2004.
3. S-J. Choi, P. J. Yoo, S. J. Baek, T. W. Kim, H. H. Lee, *An ultraviolet-curable mold for sub-100-nm lithography*, J. Am. Chem. Soc., 126, p. 7744, 2004.
4. H. Becker, U. Heim, *Hot embossing as a method for the fabrication of polymer high aspect ratio structures*, Sensors and Actuators, 83, p. 130, 2000.
5. S. Y. Chou, P. R. Krauss, P. J. Renstrom, *Imprint of Sub-25 nm vias and trenches in polymers*, Applied Physics Letters, 67, p. 3114, 1995.
6. S. Y. Chou, C. Keimel, J. Gu, *Ultrafast and direct imprint of nanostructures in silicon*, Nature, 417(6891), p. 835, 2002.
7. M. Takahashi, K. Sugimoto, R. Maeda, *Nanoimprint of glass materials with glassy carbon molds fabricated by focused ion beam etching*, Japanese Journal of Applied Physics Part 1-Regular papers brief communications & review papers, 44(7B), p. 5600, 2005.
8. H. Masuda, H. Yamada, M. Satoh, H. Asoh, M. Nakao, T. Tamamura, *Highly ordered nanochannel-array architecture in anodic alumina*, App. Phys. Lett., 71, p. 2770, 1997.
9. H. -D. Bauer, W. Ehrfeld, M. Harder, T. Paatzsh, M. Popp, I. Smaglinski *Polymeric waveguide devices with passive pigtailing: an application of LIGA technology*, Synthetic Metals, 115, p. 13, 2000.
10. J. T. Kim, C-G. Choi, H-K, Sung, *Polymer planar-lightwave-circuit type variable optical attenuator fabricated by hot embossing process*, ETRI Journal, 27, p. 122, 2005.

11. M. Komuro, J. Raniguchi, S. Inoue, N. Kimura, Y, Tokano, H. Hiroshima, S. Matsu, *Imprint characteristics by photo-induced solidification of liquid polymer*, Japanese Journal of Applied Physics, 39, p.7075, 2000.
12. S. J. Clarson,, J. A. Semlyen, *Siloxane Polymers*, Prentice Hall, Englewood Cliffs, NJ, 1993.
13. M. Keil, M. Beck, T. G. I. Ling, M. Graczyk, l. Montelius, B. Heidari, *Development and characterization of silane antisticking layers on nickel-based stamps designed for nanoimprint lithography*, Journal of Vacuum Science & Technology B, 23, p. 575, 2005.
14. http://www.evgroup.com/
15. S-W. Ahn, K-D. Lee, J-S. Kim, S. H. Kim, S. H. Lee, J-D. Park, P-W. Yoon, *Fabrication of subwavelength aluminium wire grating using nanoimprint lithography and reactive ion etching*, Microelectronic Engineering, 78, p. 314, 2005.
16. Y. Xia, E. Kim, X. -M. Zhao, J. A. Rogers, M. Prentiss, G. M. Rogers, *Complex optical surfaces formed by replica molding against elastomeric masters*, Science, 273, p. 347, 1996.
17. K. H. Jeong, J. Kim, L. P. Lee, *Biologically inspired artificial compound eyes*, Science, 312, p.557, 2006.
18. C. N. LaFratta, T. Baldacchini, R. A. Farrer, J. T. Fourkas, M. C. Teich, B. E. A. Saleh, M. J. Naughton, *Replication of two-photon-polymerized structures with extremely high aspect ratios and large overhangs*, J. Phys. Chem. B, 108, p. 11256, 2004.
19. J. A. Rogers, K. E. Paul, R. J. Jackman, G. M. Whitesides, *Using an elastomeric phase mask for sub-100 nm photolithography in the optical near field*, Appl. Phys. Lett., 70, p. 2658, 1997.
20. R. J. Jackman, J. L. Wilbur, G. M. Whitesides, *Fabrication of submicrometer features on curved substrates by microcontact printing*, Science, 26, p. 664, 1995.
21. X.-M, Zhao, Y. Xia, G. M. Whitesides, *Soft lithographic methods for nano-fabrication*, J. Mat. Chem., 7, p. 1069, 1997.

Chapter 3.

Photolithography and Replication: Planar Polymer Waveguides and Gratings

3.1 Introduction

In this chapter the technique of contact photolithography is demonstrated in its capacity as a fundamental microfabrication technique. The resulting structures are employed as templates for replication via the soft imprinting technique, to demonstrate some simple yet functional optical structures. Both planar waveguides and waveguides with optical gratings are demonstrated, with the latter as a logical progression in complexity of the former, and as a demonstration of the suitability of both polymers and replication to be used in optical applications. Mode profiles and transmission spectra are provided as proof of functionality.

This chapter begins with an overview of waveguide replication techniques, the replication of Bragg gratings, and fabrication techniques for long period gratings.

3.1.1 Planar Waveguides

Optical fibers are a ubiquitous waveguiding technology in today's communications industry. However planar waveguiding architectures offer a route to performing complex manipulations of light which are otherwise difficult to achieve with optical fibers. The planar nature of these waveguides makes them amenable to complex geometrical design which can be implemented by parallel fabrication techniques such as the traditional photolithography of the semiconductor industry.

Typical planar waveguide geometries include strip, embedded strip, rib and inverted rib structures, as shown in Figure 3.1. The materials employed for the fabrication of planar optical waveguides depend on the intended application, and range from silica and polymers, through to semiconductors and nonlinear media such as lithium niobate. Of these, polymers are a class of material that offers benefits which include low cost and simplicity, in both the fabrication of devices and the modification of the materials' optical properties.

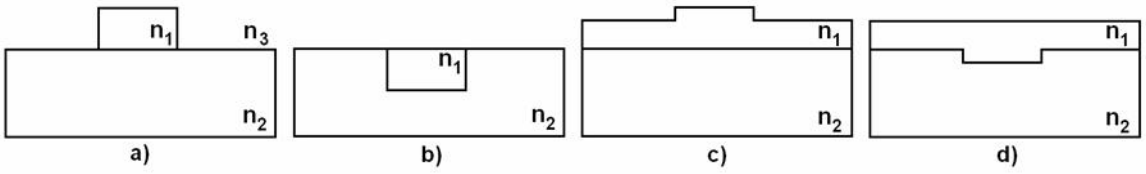

Figure 3.1: Typical integrated waveguide geometries, showing (a) strip, (b) embedded strip, (c) rib and (d) inverted rib waveguide cross-sections. Material refractive indices are designated as n_1, n_2 and n_3, where $n_1 > n_2$ and $n_1 > n_3$.

A popular approach to defining waveguides in polymer thin films has been photolithographic masking followed by etching [1,2]. However, these etch steps are often time consuming and can produce a less than ideal surface-roughness. The fabrication of planar polymer optical structures is thus especially well served by polymer replication techniques. Demonstrations in the literature can typically be divided into two camps, wherein either a rigid or elastomeric mold material has been employed.

3.1.2 Waveguides replicated using rigid molds

Chapter 2 explained that the use of rigid molds typically lends itself to the hot embossing of polymers, wherein polymers are thermally softened before they are deformed under high pressure by a normally incident mold. In the embossing of waveguides, molds have typically been silicon wafers that have been patterned by reactive ion etching (RIE) [3], although SU8 photoresist structures [4] as well as metal molds derived by the electroplating of photoresist patterns [5] have also been used.

Waveguides formed by hot embossing have typically been formed by embossing channels into a cladding polymer, which are then filled in with a higher index core polymer [3-7]. Presumably, widely spaced channels have been preferred over the embossing of widely spaced ribs because they displace a smaller volume of polymer.

The simplest waveguide architectures fabricated in this manner have been straight line, large core multimode waveguides [7]. However, more sophisticated optical structures have also been demonstrated, including optical power splitters [6], flow sensors, star couplers and optical switches [5]. Other demonstrations include luminescent waveguides, which were created by doping the core polymer with organo-lanthanide complexes [4], while double sided hot embossing has been demonstrated to simultaneously fabricate waveguides on both the top and bottom faces of a free standing sheet of polymer [8]. Multi-level structures have also been demonstrated, wherein a waveguide and optical fiber dock are defined simultaneously in order to create passive pigtailing structures for fiber coupling [4,5]. Notably, and in divergence with the definition of hot embossing, RIE defined silicon molds have been used to displace a liquid core polymer layer to create waveguiding ribs, wherein the polymer was then UV cured by exposure through a transparent glass substrate. The device fabricated in this instance was a thermo-optic optical attenuator [3,9].

3.1.3 Waveguides replicated using elastomeric molds

Compared to the hot embossing of waveguides, the material properties of elastomeric molds have enabled greater versatility in their approach to replicating waveguides, as

discussed in Chapter 2. To begin with, optically curable liquid polymers have been the staple material, rather than thermally softened polymers. These are preferred because they more readily fill the topography of the soft mold, while the optical transparency of PDMS allows for their convenient curing through the mold itself. However, the mechanism of pattern transfer also varies significantly.

Microtransfer molding with elastomeric molds is one approach that has been used to define waveguides. Here, the mold features are filled with a liquid core polymer and the polymer is then transferred to a solid substrate. This technique has been used to demonstrate both small core waveguides [10] and large core optical interconnects [11], and is known to minimize the presence of residual polymer between replicated features [11]. An alternative approach has demonstrated that liquid polymer can be drawn along mold features using a vacuum [12], while yet another has demonstrated that the elastomeric cast itself can be integrated into the final device, where its recesses form air core waveguides [13, 14]. Of course imprinting in the traditional sense has also been employed, wherein a film of liquid core polymer is deposited on a substrate and then deformed by the incident elastomeric mold [15-17]. The devices formed by these techniques include optical couplers and interferometers [18], Mach-Zehnder modulators [17], micro-ring resonators [16,19] and arrayed waveguide gratings [20].

By and large these waveguides have been approximations of strip waveguides, regardless of whether they were fabricated by rigid or elastomeric molds, wherein they have been largely symmetrical in height and width, but some degree of residual layer has been present between features.

3.1.4 Replicated Bragg gratings

In an effort to increase the utility of optical waveguides, polymer replication has also been used to integrate waveguides with optical structures such as Bragg gratings.

These waveguide gratings have been replicated in a single step, wherein both waveguide and grating have been defined on the same quartz mold [22]. However the trend has been to create the gratings and waveguides independently of one another. In this approach, two instances initially replicated the grating onto a cladding layer of polymer, after which waveguides were added on top. These waveguides have taken the

form of both PDMS air core waveguides [14], and etched higher index benzocylcobutene (BCB) polymer waveguides [21]. An alternative approach has reversed the process, first defining the waveguides in glass by etching, after which a thin layer of active polymer was added and imprinted with an elastomeric grating mold, in a demonstration of imprinting onto a non-planar substrate [23]. These varying architectures have demonstrated functionality as optical filters [21,22] and distributed feedback resonators [23].

3.1.5 Long period gratings

An alternative form of optical grating that has not been demonstrated by replication is the long-period grating (LPG), which has periods of tens of microns. These gratings were originally implemented in optical fibers, where they have typically been employed as mode converters [24], optical filters [25,26], amplifier flatteners [27], sensors [28], and dispersion compensators [29]. Their popularity has been derived from their simple geometry and modest resolution requirements, which makes them good candidates for low-cost photonic applications such as coarse wavelength-division multiplexing (CWDM) [30]. However, implementation on a fiber platform imposes restrictions on material choices, geometry and device throughput as a result of the serial nature of manipulating single fibers. As a result of these constraints, it was recently proposed that long-period gratings could be implemented in planar waveguide devices [31]. This platform provides the opportunity for increasing the throughput of these devices.

Since this proposal, numerous implementations of planar long period waveguide gratings (LPWGs) have been demonstrated. Surface relief gratings have been formed by a combination of photolithography and reactive ion etching in polymer-core waveguides [32], epoxy-clad ion exchanged BK7 glass waveguides [33], and epoxy-clad BCB ridge waveguides [34]. However, this etching technique is slow and expensive. As a result, a bid for improved throughput was made by using UV exposure to simultaneously implement index contrast and surface relief gratings in the epoxy cladding on BCB waveguides [35]. A similar process has been employed in a more recent demonstration of LPWGs, where As_2S_3 chalcogenide was used as the core waveguide material [36]. An

entirely different approach has implemented distributed metal heaters as a LPWG array, to induce a thermo-optic LPG effect [37,38].

The performance of LPWG devices is good, with typical rejections of 15-25 dB at resonance, with reasonably narrow 3-dB bandwidths of approximately 10 nm. An opportunity exists with LPWGs to demonstrate a fabrication technique that is economical, has high resolution and has the potential for mass fabrication.

3.1.6 Proposal

In this chapter, the fabrication of single mode waveguides by soft imprinting is explored for the longer infra-red wavelengths that are used in telecommunications. A rib waveguide geometry is employed in an effort to exploit the residual layer that is native to imprinting techniques, and thus minimize the volume of polymer that is displaced. Optical mode profiles are obtained to assess their performance. These waveguides are then combined with a LPG in an attempt to demonstrate a LPWG device realized completely by replication. The transmission spectrum of this structure is then obtained to test for the expected optical resonance.

3.2 Planar rib waveguides

Fabrication of the planar rib waveguide devices began with the fabrication of a rib waveguide master pattern. Photolithography was employed for this task because of its status as the fundamental processing technique in the semiconductor industry. This choice greatly simplifies the master fabrication process as compared to the etching techniques that are in common use, since etching itself uses photolithography to initially define its patterns.

3.2.1 Photolithography

The fundamental concept behind photolithography is the selective exposure of a photosensitive polymer known as photoresist, to ultraviolet light. This selective exposure is achieved by illuminating the photoresist through a mask, which typically consists of

opaque chrome features on a transparent quartz backing. The result of this exposure is that localized chemical reactions are affected within the photoresist, which modulate its solubility and allow for the creation of discrete photoresist features.

Photoresists are classified as either negative or positive, wherein their solubility is either increased or decreased by optical exposure, respectively. They are typically handled in liquid form, which is derived by the inclusion of solvents, and are coated as thin films onto suitable substrates by spin coating. Here, the centrifugal forces exerted by a spinning substrate reduce its thickness to an amount proportional to the spin speed and its viscosity. Thicknesses ranging from tens of nanometers to hundreds of microns are routinely obtained. The standard substrate used within the semiconductor industry, on account of its exceptional smoothness and flatness, is the polished silicon wafer.

Photolithography was originally implemented as a contact technique in the 1960's. A contact mask aligner achieves pattern transfer by mechanically mating the photomask to the photoresist, after which the two are illuminated with a planar ultraviolet wavefront at normal incidence. However this mechanical contact is non-conformal, which limits the resolution of the transferred patterns and can also result in mechanical damage of both the mask and photoresist.

The evolution of the semiconductor industry since its inception has seen many new iterations of mask aligners since the contact design. Its successors employ optical projection techniques which eliminate mechanical contact, and use shorter wavelengths which improve resolution. Regardless of the present day implementation however, this long evolution has resulted in the global distribution of photolithographic equipment. Contact mask aligners in particular, are a near ubiquitous technology.

3.2.2 Master fabrication process

Performing photolithography requires the use of a clean-room environment. This minimizes the influence of airborne particulates on the fabrication process, which in turn allows for the routine deposition of uniform polymer films, and uninterrupted mechanical contact between photoresist films and masks.

Fabrication of the waveguide master patterns was thus conducted in a clean-room environment and began with the preparation of 3" diameter silicon substrates. These

silicon wafers were scrubbed clean with acetone to remove organic impurities, after which acetone residue was rinsed from the wafer with methanol. The wafers were then rinsed with deionized (DI) water and blown dry with a stream of nitrogen gas, after which they were dehydrated in a convection oven at 110^{o}C for 20 minutes. Finally, the adhesion promoter hexamethyldisilazane (HMDS) was spun onto the wafer.

The image reversible photoresist AZ5206E from Clarient was used for this demonstration in its capacity as a positive photoresist. A 0.3 μm thin layer was spun onto the wafer at 3000 rpm using a spinner in a closed lid configuration. A closed lid traps solvents during the spinning process and allows thinner films to be achieved than are possible with an open lid process, where the solvents are free to evaporate.

To promote uniform contact between the photoresist and mask during exposure, the thick edge-bead was next removed from the photoresist film. This was performed automatically by the spin coating unit, which dispensed solvents onto the outer limits of the substrate while spinning. A 20 minute softbake was then conducted at 90^{o}C in a convection oven. The primary effects of this bake are to expel solvents from the photoresist, which improves adhesion between the photoresist and substrate, and prevents the photoresist from sticking to the mask during exposure.

Straight line waveguides were then exposed into the photoresist film using a Karl Suss MJB3 contact mask aligner. Several widths around 7 μm were exposed using a broadband source which was derived from a mercury arc lamp. The exposed photoresist pattern was then developed in a solution of one part AZ400K developer (Clarient) and five parts deionized (DI) water. During development, the substrate and photoresist were agitated to ensure that the photoresist had constant access to fresh developer. The photoresist pattern was then rinsed with DI water to stop the developing process, and the wafer was blown dry with nitrogen gas. This completed the fabrication of the photoresist master pattern. Figure 3.2 shows an SEM image of the master structure, showing a cross section through a single waveguide rib.

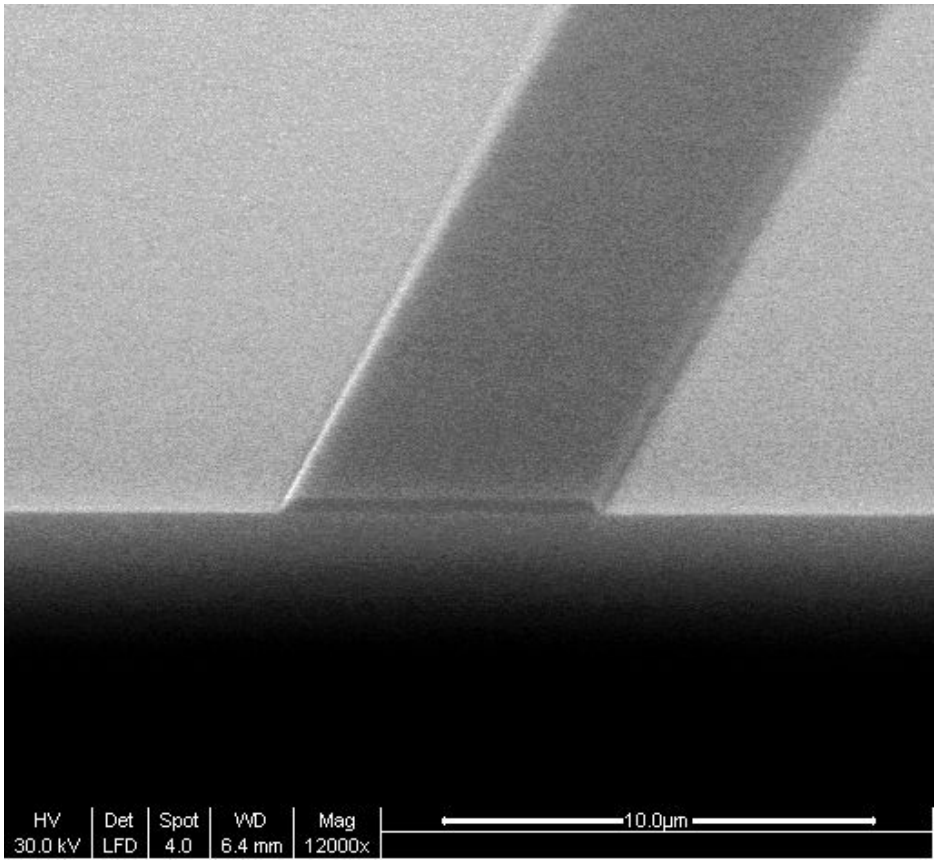

Figure 3.2: SEM micrograph of a cross section through the photoresist on silicon waveguide master structure.

3.2.3 PDMS casting

A mold was derived from this photoresist master by casting it in PDMS. This process began with the preparation of a PDMS liquid solution, which was purchased from Dow Corning (Sylgard 184 Elastomer kit) and consisted of two components – a base and a curing agent. These were dispensed in a 10:1 ratio and were mixed vigorously to ensure their homogeneous distribution. A good indication of sufficient mixing was a high concentration of bubbles distributed uniformly throughout the mixture. Inadequate mixing was liable to result in incurable regions within the bulk, later resulting in sections breaking away from the mold. This preparation was conducted in a clean-room environment in order to minimize the particle content of the PDMS bulk, and thus maximize its optical transparency.

Once prepared, the PDMS mixture was poured directly onto the master photoresist pattern to a depth of approximately 4 mm. The mixture was then degassed in a vacuum chamber for 30 minutes to remove air bubbles and was cured in a convection oven for several hours at 60°C. After curing, the PDMS was peeled from the photoresist pattern to yield a 4 mm thick elastomeric cast, holding an inverse of the master pattern, as illustrated in Figure 3.3c.

In a demonstration of the surface properties of PDMS, this PDMS cast was itself used as a master pattern, to produce a second PDMS cast. This second cast inverted the structures held by the first PDMS cast to match those held by the original photoresist master. The PDMS mixture for this second cast was prepared as described above. Before casting, the planarity of the original mold was ensured by conforming its backside to a polished 3" pyrex wafer**,** as illustrated in Figure 3.3d**.** The PDMS mixture was then poured over the cast, degassed and cured as above, after which the two molds separated cleanly along the patterned interface. Figures 3.3f and 3.3g show photographs of a completed PDMS cast. Notice its transparency and its flexibility.

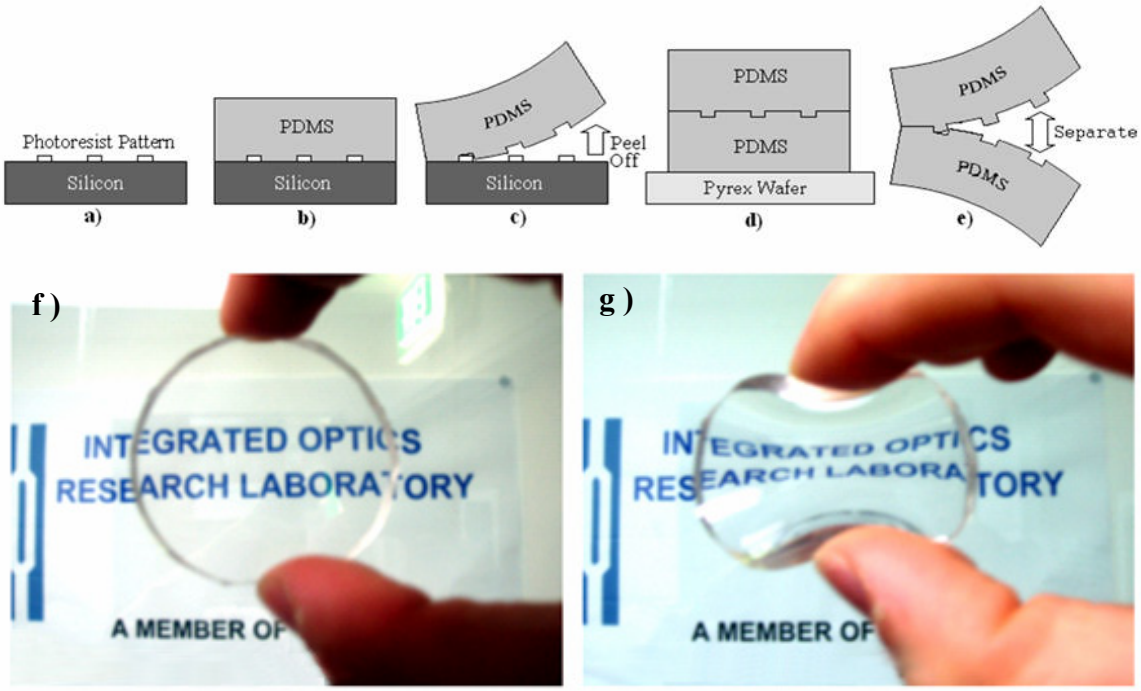

Figure 3.3: Process diagram illustrating (a-e) the derivation of PDMS molds from master patterns. Photographs of the resulting PDMS mold are shown, illustrating its (f) transparency and (g) flexibility.

As a result of the refractive index match and the conformal contact between the two slabs of PDMS, it was often difficult to identify the interface between the two, which made it difficult to initiate separation. The typical solution to this problem was to mark the face of the original mold before immersing in PDMS. This marker typically took the form of a piece of colored sticky tape.

These two molds, which hold inverse patterns with respect to one another, are intended for imprinting rib waveguides and inverse rib waveguides respectively.

3.2.4 Polymers for waveguiding

The polymers employed in this demonstration were liquid and photocurable, and were selected on the basis that they were compatible with one another, and had performed well in previous investigations [1]. The low index UV15 (n ~ 1.5080 at 1550 nm) from Masterbond was selected as a cladding layer, while the negative photoresist SU8-2 (n ~ 1.57 at 1550 nm) from Microchem was chosen as a core material.

The rigid substrates used to support these liquid polymers were polished silicon wafers (n ~ 3.5 at 1550 nm). These were selected because of their ready availability, exceptional smoothness, and their amenability to mechanical dicing without chipping. However, the high refractive index of silicon posed the problem of optical leakage from the core material into the silicon. This was prevented by using a cladding layer that was tens of microns in thickness, which acted to optically isolate the core from the cladding. The cladding was spun to ~50 μm, while the core was ~3 μm.

3.2.5 Imprinting overview

All imprinting work was performed in a clean room environment under the laminar airflow from a high efficiency particulate air (HEPA) filter. This was necessary because of the susceptibility of liquid polymers to accumulate airborne particulates, which can prevent the spin coating of uniform films, and can act as optical scatterers if they are trapped within the polymer waveguides.

Contact between the PDMS and the liquid polymer, or rather, wetting of the PDMS mold by the liquid polymer, was conducted progressively and under strict control, as

illustrated in Figure 3.4c. The mold, which was manipulated by hand, was first flexed to present a convex patterned surface, and then contact was initiated between one edge of the mold and that of the polymer coated substrate. The flexed mold was then slowly lowered onto the polymer, so that wetting progressed as a continuous front across the mold, from the point of contact to the opposite end of the wafer. In the instance that a section of mold would find itself unwet and surrounded by wetted mold, it would typically result in the formation of an air bubble at the mold/polymer interface, and prevent transfer of the pattern in that region.

This progressive imprinting inevitably resulted in the displacement of some volume of polymer across the substrate surface. This was observed to be more significant when thick layers of low viscosity polymer were employed. Additionally, the uneven pressure exerted by the manual manipulation of the mold during imprinting occasionally resulted in subtle non-planarities in the final polymer thickness. This non-planarity could be alleviated somewhat by allowing the mold/polymer/substrate stack to sit for a while before curing, thus providing the liquid polymer with some time to redistribute itself evenly. The uneven deformation of the mold during imprinting, and the redistribution of the polymer before curing, were both found to be favorably influenced by the use of a thicker mold bulk, which provided greater resistance to deformation during imprinting, and a superior tendency to maintain a planarized state while at rest on the surface of the liquid polymer.

3.2.6 Replicating the waveguides

The two molds derived previously, which hold inverse structures relative to one another, were applied to imprinting both rib and inverted rib waveguides. The mold that was derived from the photoresist on silicon pattern was used to imprint ribs into the core layer, as illustrated in Figure 3.4, while the mold derived from this PDMS cast was used to imprint inverted ribs into the cladding layer, as illustrated in Figure 3.5.

Although one can expect little difference in the performance of these two architectures, the inverted-rib device was observed to display a superior flatness as compared to the rib waveguides. This non-flatness in the latter device was caused by the edge bead in the cladding layer, which was solidified and thus locked in place when the

UV15 was optically cured, and was subsequently transferred to the core layer as shown in Figure 3.4. On the other hand, the imprinting of inverted ribs onto the cladding layer acted to planarized these edge beads, resulting in improved uniformity in both cladding and core layers, as illustrated in Figure 3.5.

Pattern transfer was achieved by curing the imprinted polymers while the molds were in place. The UV15 was cured using a single UV flood exposure of 1200 mJ/cm^2. The SU8-2 was soft-baked on a hot plate for 5 minutes at 65^{o}C and 5 minutes at 95^{o}C with a temperature gradient of 4^{o}C/min. After a 150 mJ/cm^2 UV flood exposure, the SU8-2 film was post-baked as per the soft-bake. Peeling back the mold after curing the imprinted polymer yielded the replicated waveguide patterns. The completed structures used air as the upper cladding material.

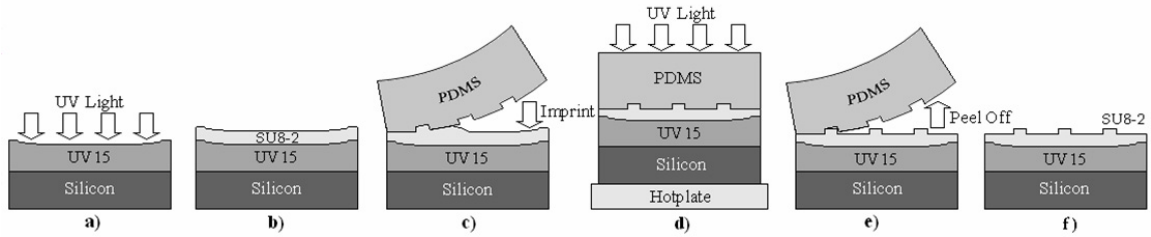

Figure 3.4: Process diagram illustrating the imprinting of rib waveguides.

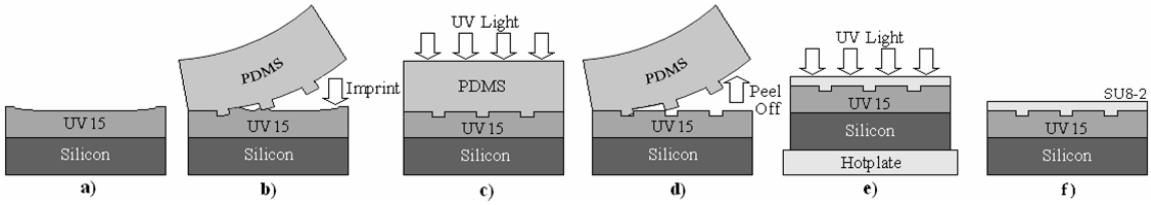

Figure 3.5: Process diagram illustrating the imprinting of inverted-rib waveguides.

3.2.7 Endface preparation

The endfaces of the imprinted waveguides were then prepared by mechanical dicing. A DISCO DAD321 dicing saw was used to simultaneously cut across the waveguides and polish their endfaces. This produced endfaces that were smooth, flat and defect free, as shown in Figure 3.6. Normally, a lapping and polishing technique is used to prepare the

endfaces of optical devices, however this is much more involved than mechanical dicing, and requires the addition of a protective polymer layer on the top of the device before the polishing can be performed.

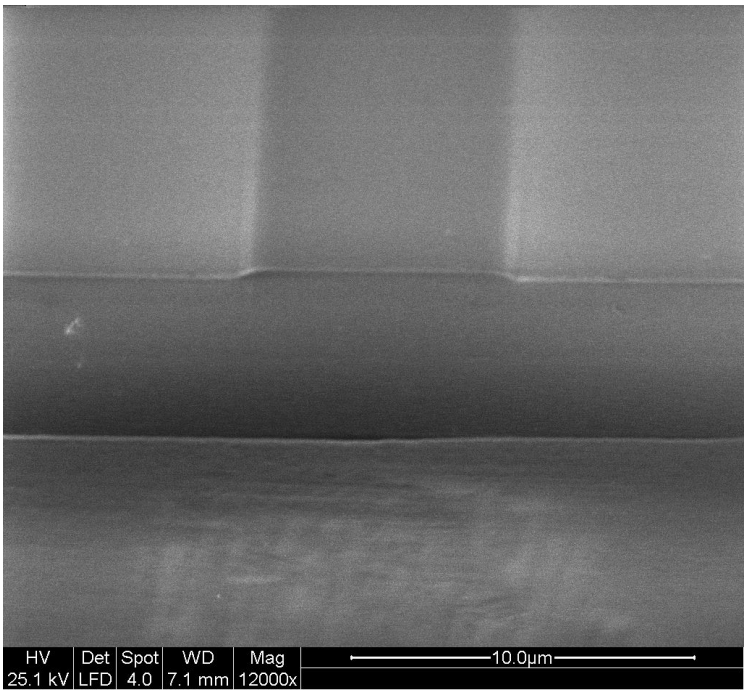

Figure 3.6: An SEM image of a typical imprinted waveguide, showing the diced endface. Notice the shallow rib height, and the smoothness of both the imprinted upper surface and the diced endface.

The completed waveguide devices were 3 cm long. Optical microscope images in Figure 3.7 show the sequence of structures involved in the fabrication of these waveguides, starting with a master photoresist pattern and progressing through a PDMS mold, to diced imprinted waveguides.

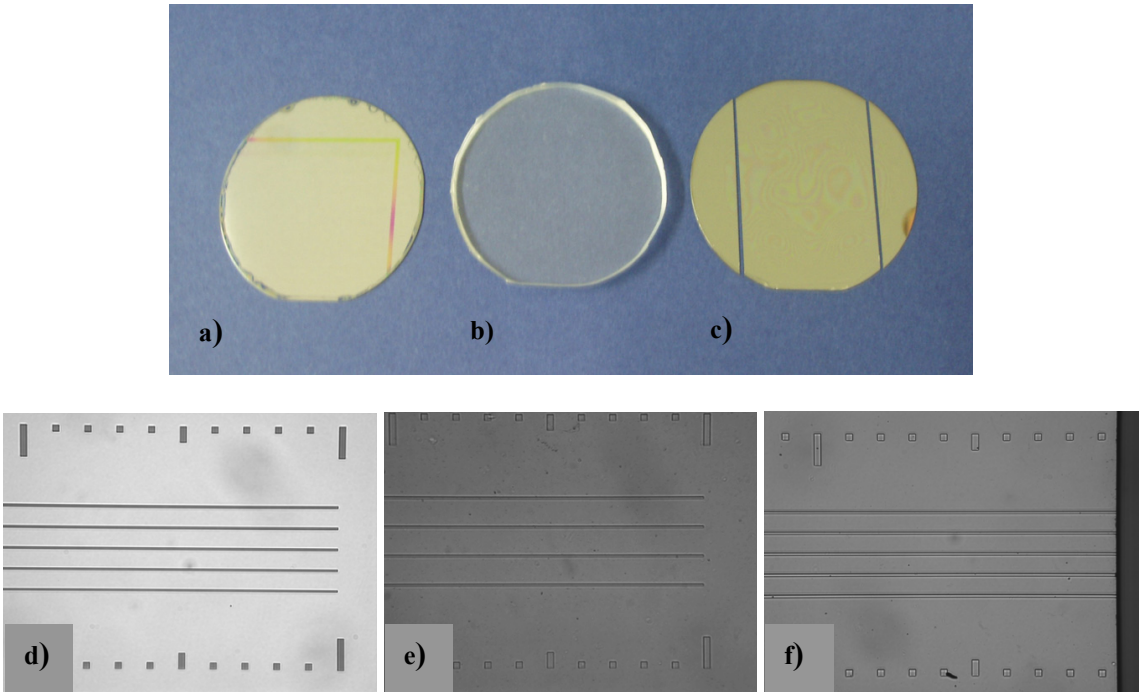

Figure 3.7: The structures involved in the replication of waveguides are shown in sequence, starting with (a) the photoresist master pattern on silicon (b) the PDMS mold and (c) the diced SU8 replica. Optical microscope images are shown of the each in (d) to (f), in the same order.

3.2.8 Optical measurements

The optical performance of these waveguides was examined by fiber coupling laser light into one endface of the device, and then imaging the light that emerged from the opposite face, as illustrated in Figure 3.8. These images allowed the power distribution within the waveguides to be observed as optical mode profiles.

These measurements were made by first mounting the diced waveguides onto a micropositioning stage. A second micropositioning stage was then used to align an optical fiber to one of the waveguide endfaces, in a technique known as butt-coupling. A 632.8 nm He-Ne laser was initially used to launch light through the optical fiber to facilitate alignment by providing a visible source. Once the light had been successfully launched into the planar waveguide, an objective lens was carefully positioned at the output of the same waveguide using a third micropositioning stage. This lens collected light leaving the waveguide, and focused it onto a CCD array camera. Image capture software displayed the mode profiles of the guided light, as shown in Figure 3.9. The

laser source was then changed from the visible spectrum, to the infra-red at 1550 nm. This wavelength was sourced from an Agilent infrared tunable laser. This change was made without disturbing the alignment of the insertion fiber, the device, or the objective lens. Mode profiles were again collected.

Both the rib and inverted rib waveguides were successful in guiding the coupled light. Single mode guiding was observed at 1550 nm for both waveguide geometries, as shown in Figure 3.9a and 3.9b, while a loss of symmetry was observed for 632.8 nm, as shown in Figure 3.9c, indicating multimode guiding.

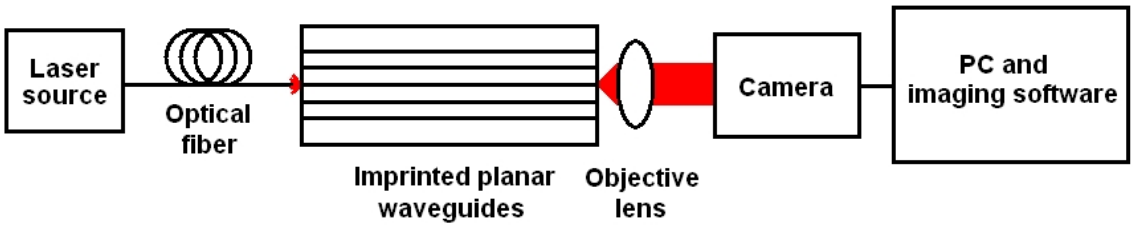

Figure 3.8: Optical testing apparatus.

It should be noted that the alignment process for testing was much simpler for the rib waveguides than for the inverted rib waveguides. This was because of the greater visibility provided by having the ribs on the top surface of the device, while the inverted ribs were buried beneath the core material, and thus difficult to locate.

For the generation of these mode profiles, the power that was coupled into the waveguides was largely set arbitrarily, with the only criteria being the power thresholds of the imaging camera. Here, the objective was to generate clear images of the guided mode profiles. It was noted that at relatively high powers, slab guided modes were observable within the core material between waveguide ribs, as discussed in [9]. This slab guiding would be a concern if cross-talk between waveguides needed to be explicitly avoided, in which case the lateral confinement provided by the rib structures would need to be improved. This could be implemented by providing higher aspect-ratio master structures, which could be very simply achieved by using a thicker layer of photoresist during fabrication of the master structure.

Rough cutback loss measurements, performed by colleagues, indicated that the waveguide losses were on the order of ~7 dB/cm. This is thought to be primarily caused

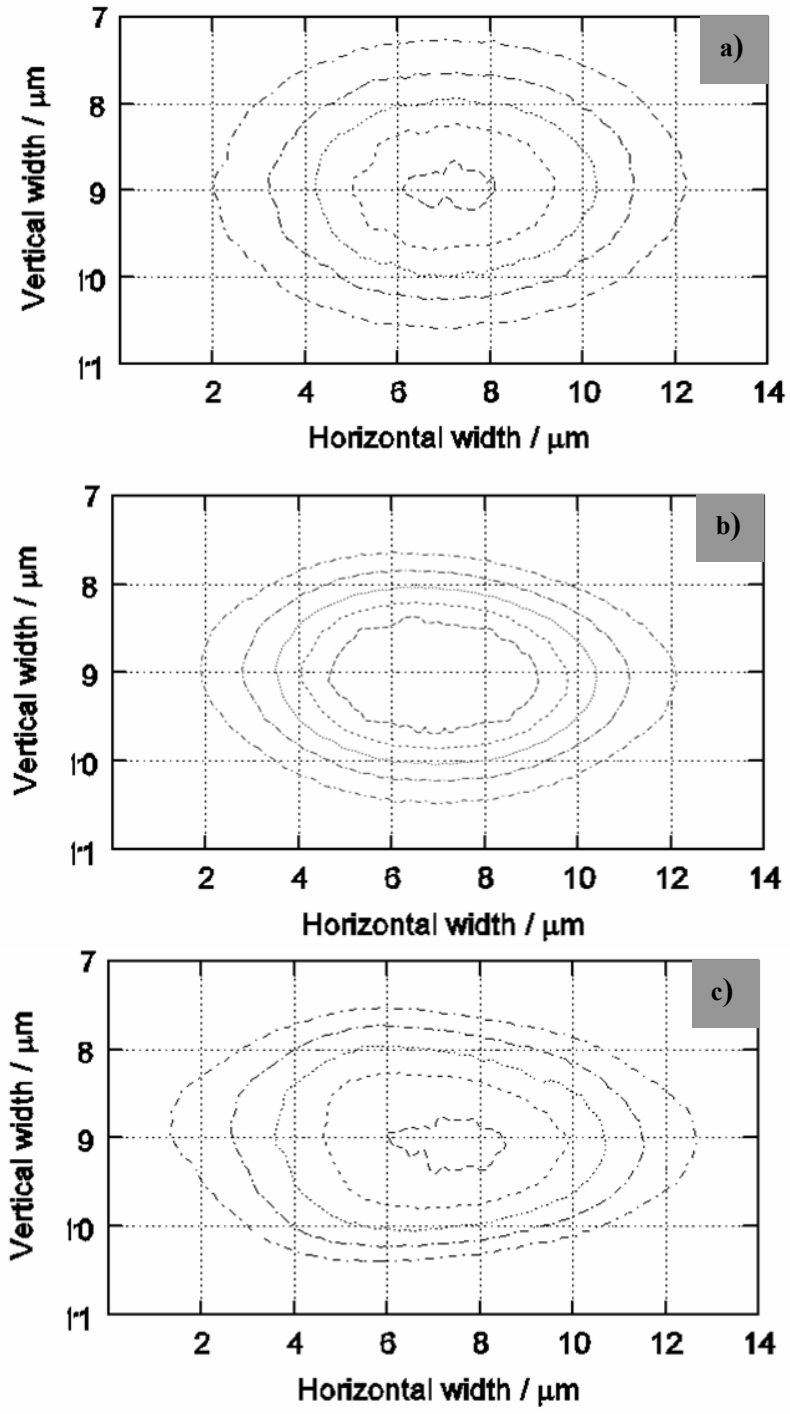

Figure 3.9: Mode profiles collected from the imprinted waveguides. Single mode guiding is shown at 1550 nm for both (a) rib and (b) inverted rib structures, while a loss of symmetry (c) is observed at 633 nm in a rib waveguide.

by polymer material absorption, and is thus not of great concern, since perfluoropolymers offer an ultra-low loss alternative [39]. Optical coupling loss is also thought to contribute to the overall losses, resulting from a mismatch in the fiber and planar waveguide geometries.

3.3 Long period waveguide gratings

Having successfully demonstrated imprinted waveguides, the next step in this proposal is to add a wavelength selective functionality. This is implemented by employing a second imprinting step to incorporate a LPG into the rib waveguide device. This work was performed in collaboration with a fellow PhD student in our group [40].

The proposed waveguide grating structure is illustrated in Figure 3.10, wherein the grating structure is imprinted at the core-cladding interface, and the waveguide rib is imprinted at the core-air interface. Light launched into the waveguide is expected to excite the fundamental mode in the core, and when the conditions for resonance are met, this is to be coupled into the first order mode which resides primarily in the cladding layer. This architecture was chosen for the simple reason that alignment during optical testing was simpler for rib rather than inverted rib waveguides.

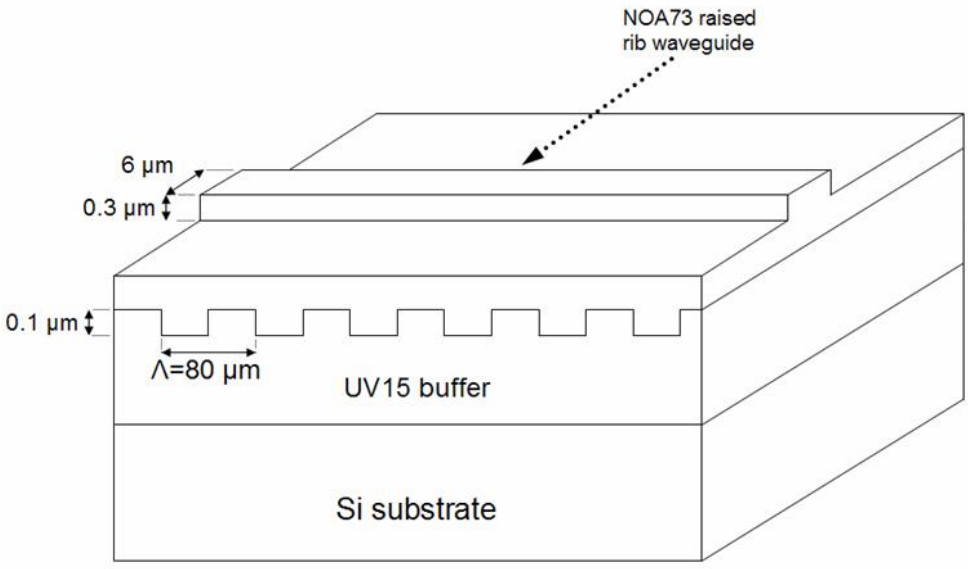

Figure 3.10: A diagram illustrating the proposed LPWG structure, showing the LPG at the cladding/core interface, and the waveguide rib on the core layer.

3.3.1 Structure design

The LPWG device was designed to achieve resonance in the vicinity of 1550 nm. Its specific geometry was derived by performing approximate calculations for a transverse-electric (TE) polarized field.

A one-dimensional finite-difference mode solver was used to calculate the effective refractive indexes $n_{eff,1}$ and $n_{eff,2}$, of the fundamental core mode and the forward propagating cladding mode, respectively. These calculations assumed a UV15 cladding layer thickness of 20 μm, and an NOA73 (Norland Optical Adhesive) core layer thickness of 3.55 μm. The TE refractive index of each layer had previously been measured to be 1.5080 and 1.585 respectively, at 1550 nm.

The effective index method was then used to calculate the appropriate grating period Λ, which is described by the phase matching condition $\lambda/(n_{eff,1}-n_{eff,2})$, where λ is the resonant wavelength. Since effective indexes were calculated to be approximately 1.508 and 1.527 at 1585 nm respectively, a grating period of 80 μm was calculated for resonance at this wavelength.

The depth of these gratings was selected to be 100 nm, on the basis that it would provide a reasonable coupling length of 3.29 mm. Within this distance, complete power transfer is expected to occur from one mode to the next. Additionally, this depth would not impose excessive radiation losses, as has been demonstrated elsewhere [33]. Over a device that is 10 mm in length, multiple couplings can be expected back and forth between the core and cladding.

For a more thorough treatment of the device simulations, the interested reader is referred to the PhD thesis of Andreas Perentos [40].

3.3.2 Grating master fabrication

The surface relief master pattern for the grating was fabricated using a combination of liftoff photolithography and electron-beam evaporation, which offers nanometer precision in deposited thickness.

Liftoff photolithography is conducted by specifically engineering the profile of a photoresist structure so that it is undercut or T-topped, as shown in Figure 3.11. These

profiles are exploited during the line of sight deposition of electron beam evaporated material so that the material is deposited in discrete regions rather than as a continuous film. When normal incidence coating is conducted on this undercut photoresist, material deposition occurs on the tops of the photoresist and on the exposed regions of substrate, but not on the sidewalls of the photoresist. This leaves the sidewalls and thus the entire photoresist feature vulnerable to dissolution by immersion in a liquid solvent such as acetone. Thus, after material has been deposited, the photoresist patterns can be 'lifted-off, leaving only the deposits on the substrate.

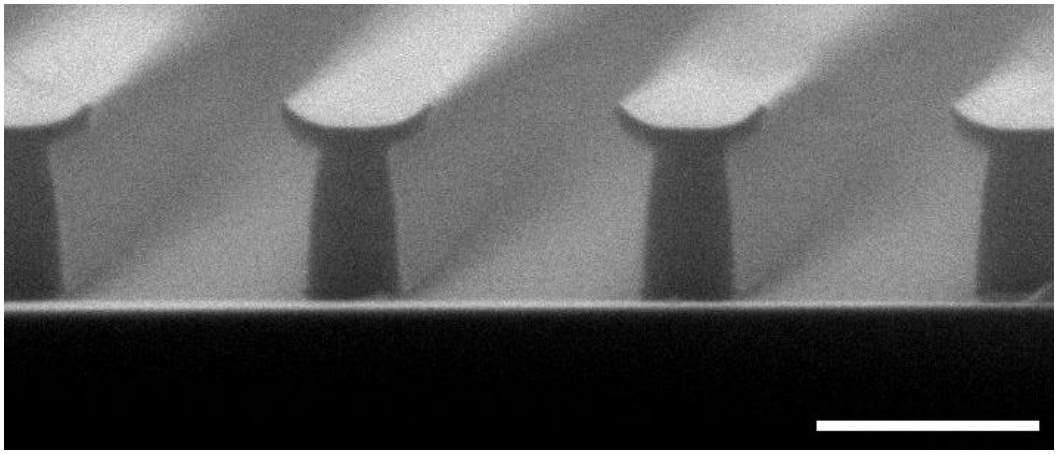

Figure 3.11: An SEM micrograph shows a cross section through an arbitrary photoresist pattern that has been soaked in chlorobenzene before developing. The undercut or T-topped profile of chlorobenzene soaked photoresist is shown. Scale bar is 2 μm.

The photolithography for fabricating the undercut photoresist templates began with spinning a 1.2 μm thick layer of AZ1512 photoresist (Clariant) on an appropriately prepared silicon substrate, which was then softbaked at 90^{o}C for 20 minutes in a convection oven. A Karl-Süss MJB3 mask aligner was then used to expose an 80 μm period grating pattern into the photoresist, as illustrated in Figure 3.12, after which undercut profiles were imposed by a 10 minute soak in chlorobenzene. The chlorobenzene soaked into the upper regions of the photoresist, where it acted to reduce the solubility of the photoresist. The photoresist was then rinsed with DI water to remove residual chlorobenzene and was developed for about 1 minute in a 1:4 dilution of AZ400K developer in DI water.

A layer of titanium was then deposited onto the photoresist template at normal incidence to a thickness of 100 nm in a Balzers / BAK 600 electron beam evaporation coating system. Titanium was selected as the deposited material simply as a means of maximizing the durability of the master structure, a property which is derived from titanium's mechanical robustness and strong adhesion properties.

Liftoff was then achieved by dissolving the undercut photoresist template in a beaker of acetone that had been heated to 80^{o}C. This left only a titanium grating pattern on the silicon substrate. Casting of this grating template in PDMS was conducted as described previously for the casting of the waveguide patterns.

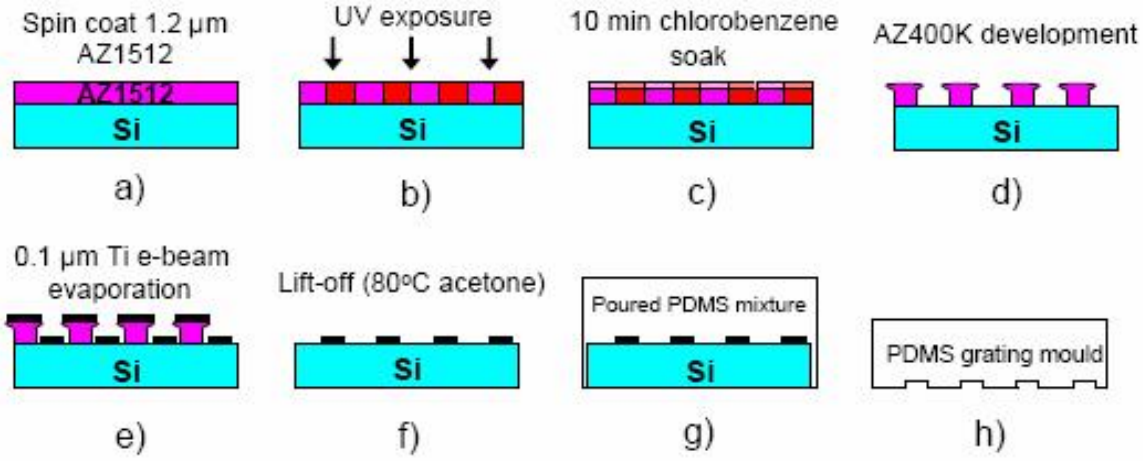

Figure 3.12: Process diagram illustrating the fabrication of a grating master pattern, from which a PDMS mold is derived.

3.3.3 Device fabrication

The second mold required for this LPWG device is that of the waveguide. The fabrication of both the waveguide master structure and its mold were performed as described in Section 3.2. Thus the imprinting of the proposed waveguide and grating structure was conducted as a sequence of spinning and imprinting steps, as illustrated in Figure 3.13, which is effectively a combination of the rib and inverted-rib imprinting sequences.

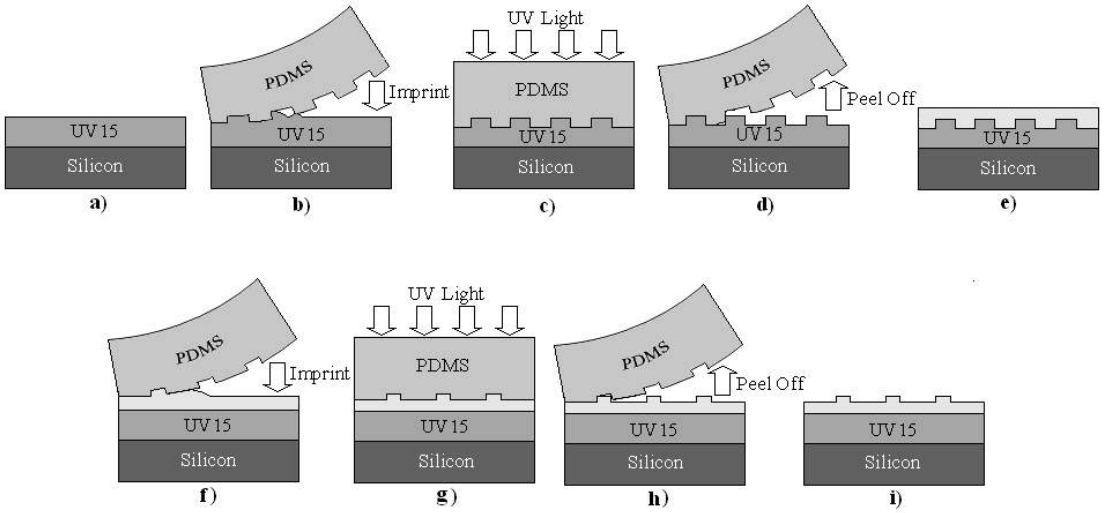

Figure 3.13: A process diagram illustrating the sequence of imprinting steps employed in fabricating the waveguide grating structure. A cladding layer of (a) UV15 is first spun onto a flat substrate and then (b-d) imprinted with the grating structure. A core layer is then (e) deposited. After the device is rotated by 90 degrees, the structure is completed by (f-h) imprinting waveguide ribs across the gratings.

First, the thick UV15 cladding layer was spun onto the silicon wafer substrate. A spin speed of 1000 rpm was used to achieve a film thickness of 20 μm, after which the grating mold was applied. This flattened out non-planarities that were induced by the edge bead, as was demonstrated with the imprinting of the inverted rib waveguides. The UV15 layer was then cured by a 5 minute ultraviolet exposure from the Karl-Süss mask aligner, after which the mold was carefully peeled away.

An Ambios XP-2 profilometer was then used to compare the quality of the grating replica to the master pattern, as shown in Figure 3.14. The depth and shape of the gratings were replicated to a reasonable degree of accuracy, however over longer distances of millimeters, the baseline of the replica was observed to fluctuate. This was attributed to the flexibility of the mold material, as was discussed in Section 3.2.5.

Next, a core layer of NOA73 was spun over the replicated grating pattern. NOA73 was used instead of SU8-2 because of the index contrast requirements of work being conducted beyond the scope of this thesis.

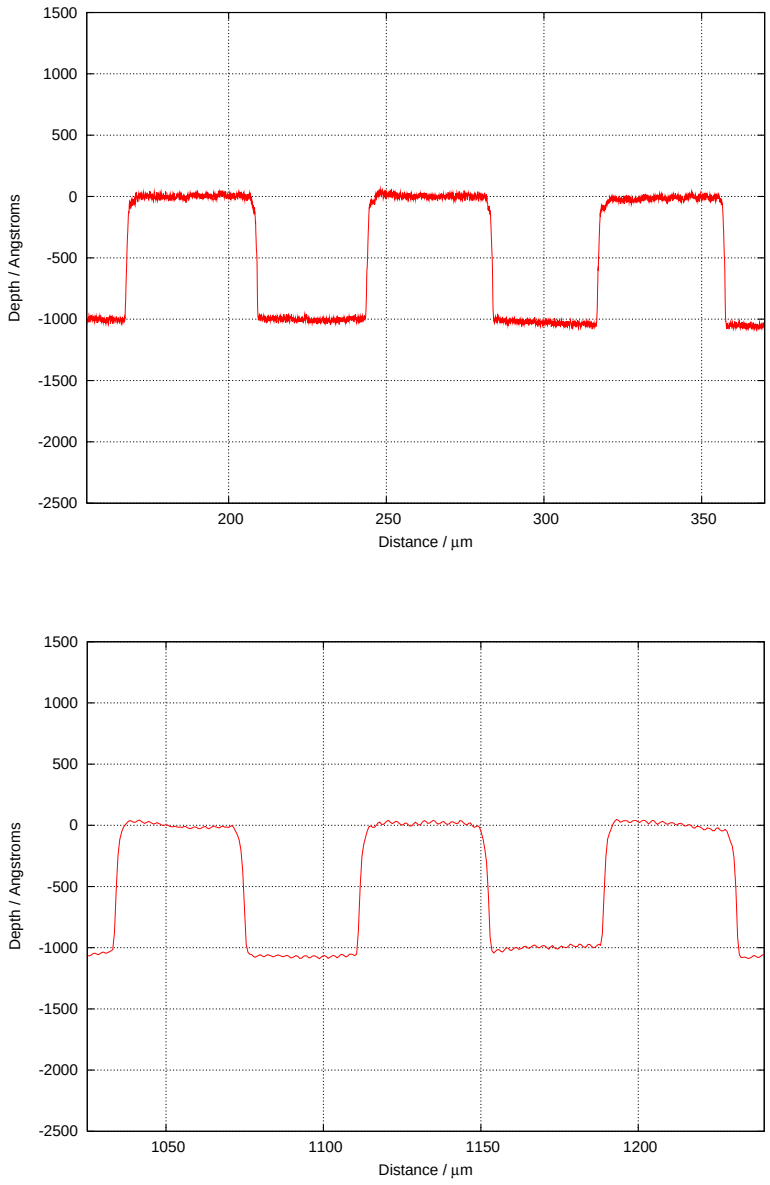

Figure 3.14: Profiles of (a) the titanium on silicon master grating structure and (b) the polymer replica.

Numerous thicknesses of core material between 3.5 µm and 3.7 µm were spun in order to account for the expected changes in thickness induced by imprinting. These were implemented by using a range of speeds between 4000 and 4500 rpm. This layer was then imprinted with the rib waveguide structure, wherein the waveguides were oriented orthogonal to the direction of the grating lines. The NOA73 was then cured using four exposures of five minutes each from the Karl Suss mask aligner. Peeling away the

waveguide mold ended the pattern transfer process. The endfaces of this structure were prepared for optical testing as per the replicated waveguides in Section 3.2.7.

3.3.4 Optical measurements

Transmission spectra of the LPWG devices were acquired using the same micropositioning apparatus that was used to test the imprinted waveguides. However, in this instance, a polarization maintaining (PM) fiber was used to launch TE mode polarized light into the device. Initial alignment was once again performed using a 632.8 nm source, after which the source was switched to the tunable infrared Agilent laser.

After alignment of the source fiber, the output light was collected by a second optical fiber, as shown in Figure 3.15, which guided the light into a Newport optical power meter. Both the Agilent laser and the power meter were interfaced with a Labview program, which tuned the input wavelength and plotted the measured output power.

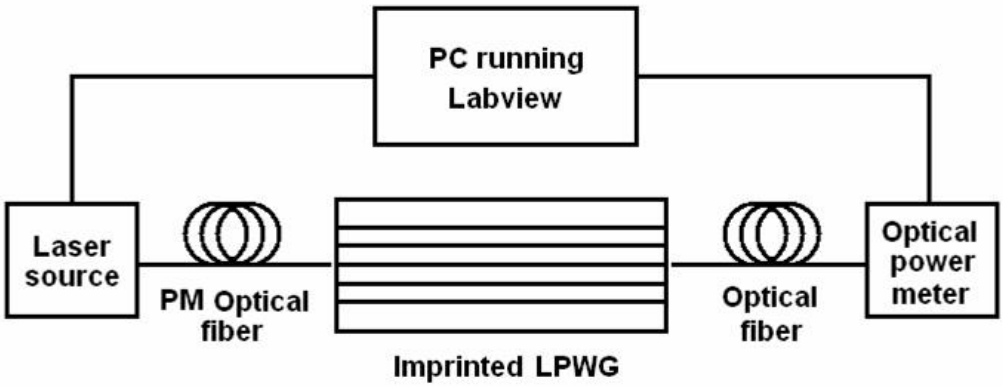

Figure 3.15: Test apparatus for obtaining the transmission spectrum of the LPWG.

The spectral response of the LPWG device for TE polarization is shown in Figure 3.16. Resonance was clearly observed at 1585 nm, with a rejection level of ~10 dB and a 3 dB bandwidth of ~12 nm, demonstrating the functionality of the device. This performance is close to the expected values discussed in Section 3.1.5.

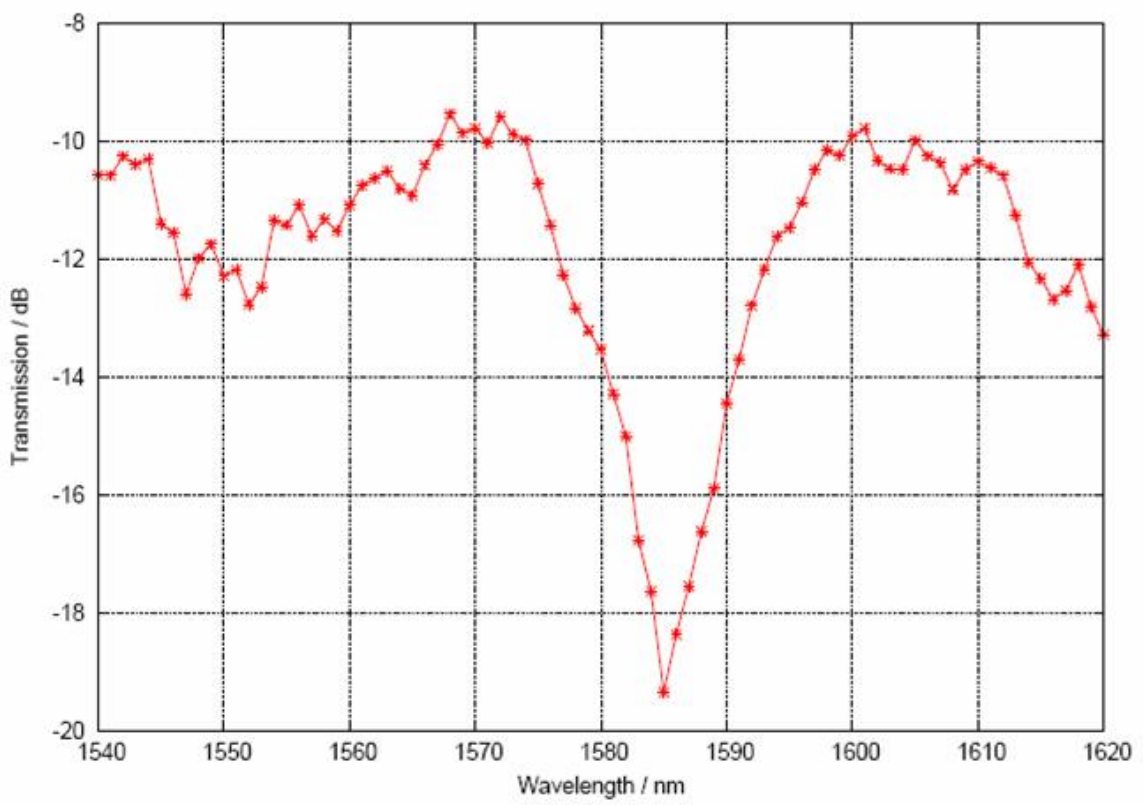

Figure 3.16: Spectral transmission of waveguide grating structure, showing resonance at 1585 nm.

3.4 Summary and conclusions

The rapid and low-cost replication of planar integrated waveguides and a LPWG has been demonstrated using soft imprint polymer replication using UV15, SU8-2 and NOA73 polymers.

These waveguides demonstrated multimode guiding at 632.8 nm, and single mode guiding in the vicinity of 1550 nm. The waveguide master patterns took the forms of photolithographically patterned photoresist and as such, this technique could be used to fabricate waveguides of almost arbitrary sizes and spacing.

The replicated gratings on the LPWG device were of very good quality. Resonance was successfully achieved at 1585 nm, with a rejection level of ~10 dB and a 3 dB bandwidth of ~12 nm. This resolution and coupling strength makes replication an attractive approach to fabricating LPWG for CWDM applications.

In regards to the suitability of this technique for mass producing waveguides and LPWG's, it should be noted that once master structures and molds had been fabricated, the replication processes took only minutes to perform. Additionally, these molds could be applied to imprinting many devices without suffering damage, while a single master structure could be used to cast many molds, such that continuous parallel fabrication becomes possible. However, further work is required to address material optical losses and material thickness fluctuations caused by polymer displacement during imprinting.

3.5 References

1. V. Balkunje, A. Holland, and A. Mitchell, *Fabrication of Polymer rib Waveguides Using SU-8*, ACOFT, Canberra, 2004.
2. A. S. Holland, P. W. Leech, and G. K. Reeves, *Reactive ion etching of organic polymers for application in waveguide trench molds*, *Journal of Materials Science*, 39, p. 3505, 2004.
3. J. Kim, C.-G. Choi and H. Sung, *Polymer planar-lightwave-circuit-type variable optical attenuator fabricated by hot embossing process*, *ETRI*, 27, p. 122, 2005.
4. S. Moynihan, R. Van Deun, K. Binnemans, J. Krueger, G. von Papen, A. Kewell, G. Crean, G. Redmond, *Organo-lanthide complexes as luminescent dopants in polymer waveguides fabricated by hot embossing*, *Optical materials*, 29, p. 1798, 2007.
5. H. -D. Bauer, W. Ehrfeld, M. Harder, T. Paatzsh, M. Popp, I. Smaglinski *Polymeric waveguide devices with passive pigtailing: an application of LIGA technology*, Synthetic Metals, 115, p. 13, 2000.
6. C.-G. Choi, S.-P. Han, B. C. Kim, S.-H. Ahn, and M.-Y. Jeong, *Fabrication of large-core 1 x 16 optical power splitters in polymers using hot-embossing process*, Photonics Technology Letters, IEEE, 15, p. 825, 2003.
7. C.-G. Choi, *Fabrication of optical waveguides in thermosetting polymers using hot embossing*, Journal of Micromechanics and Microengineering, p. 945, 2004.
8. C.-G. Choi, S.-P. Han, and M.-Y. Jeong, *Two-dimensional polymeric optical waveguides for high-density parallel optical interconnection*, Optics Communications, 235, p. 69, 2004.
9. J. Kim and C.-G. Choi, *Polymeric PLC-type thermo-optic optical attenuator fabricated by UV imprint technique*, Optics Communications, 257, p. 72, 2006.
10. X. Zhao, Y. Xia and G. M. Whitesides, *Fabrication of three-dimensionaal micro-structures: Microtransfer molding*, Advanced Materials, 8, p. 837, 1996.
11. B.-T. Lee, M. Kwon, J. Yoon, S. Shin, *Fabrication of polymeric large-core waveguides for optical interconnects using a rubber molding process*, IEEE Photonics Technology Letters, 12, p. 62, 2000.

12. BM. S. Kim, J. W. Yoon, J. H. Oh, *Fabrication of multimode polymer waveguide using new replication method*, Optical Society of America, 2004.
13. G. Splawn and F. E. Lytle, *On-chip absorption measurements using an integrated waveguide*, Anal. Bioanal. Chem., 373, p. 519, 2002.
14. R. Horvath, L. R. Lindvold, and N. B. Larsen, *Fabrication of all-polymer freestanding waveguides*, Journal of Micromechanics and Microengineering, p. 419, 2003.
15. W. Kim, J. Lee, S. Shin, B. B and Y. Kim, *Fabrication of ridge waveguides by UV embossing and stamping of sol-gel hybrid materials*, IEEE Photonics Technology Letters, 16, p. 1888, 2004.
16. J. K. S. Poon, Y. Huang, G. T. Paloczi, A. Yariv, *Soft lithography replica molding of critically coupled polymer microring resonators*, IEEE Photonics Technology Letters, 16, p. 2496, 2004.
17. G. T. Paloczi, Y. Huang, A. Yariv, J. Luo and A. K.-Y, Jen, *Replica-molded electro-optic polymer Mach-Zehnder modulator*, App. Phys. Lett., 85, p. 1662, 2004.
18. X. Zhao, S. P. Smith, S. J. Waldman, G. M. Whitesides and M. Prentiss, *Demonstration of waveguide couplers fabricated using microtransfer molding*, App. Phys. Lett., 71, p. 1017, 1997.
19. D. Kim, J. I, S. Lee, S. Ahn and K. Lee, *Polymeric microring resonator using nanoimprint technique based on a stamp incorporating a smoothing buffer layer*, IEEE Photonics Technology Letters, 17, p. 2352, 2005.
20. J. Lim, S. Lee, K. Lee, *Polymeric arrayed waveguide grating using imprint method incorporating a flexible PDMS stamp*, Optics Communications, 272, p. 97, 2007.
21. A. Kocabas and A. Aydinli, *Polymeric waveguide Bragg grating filter using soft lithography*, Optical Society of America, 14, p. 10228, 2006.
22. S. Ahn, K. Lee, D. Kim and S. Lee, *Polymeric wavelength filter based on a Bragg grating using nanoimprint technique, IEEE Photonics technology Letters*, 17, p. 2122, 2005.

23. J. A. Rogers, M. Meiere, A. Dodabalapur, E. J. Laskowski and M. Cappuzzo, *Distributed feedback ridge waveguide lasers fabricated by nanoscale printing and molding on nonplanar substrates*, App. Phys. Lett., 74, p. 3257, 1999.
24. K. O. Hill, B. Malo, K. A. Vineberg, F. Bilodeau, D. C. Johnson, and I. Skinner, *Efficient mode conversion in telecommunication fibre using externally written gratings*, Electron. Lett. 26, p. 1270, 1990.
25. A. M. Vengsarkar, P. J. Lemaire, J. B. Judkins, V. Bhatia, T. Erdogan, and J. E. Sipe, *Long-period fiber gratings as band-rejection filters*, J. Lightwave Technol. 14, p. 58, 1996.
26. A. Abramov, B. J. Eggleton, J. A. Rogers, R. P. Espindola, A. Hale, R. S. Windeler, and T. A. Strasser, *Electrically tunable efficient broad-band fiber filter*, IEEE Photon. Technol. Lett., 11, p. 445, 1999.
27. P. F. Wysocki, I. B. Judkins, R. P. Espindola, M. Andrejco, and A. M. Vengsarkar, *Broad-band erbium-doped fiber amplifier flattened beyond 40 nm using long-period grating filter*, IEEE Photon. Technol. Lett., 9, p. 1343, 1997.
28. V. Bhatia, *Applications of long-period gratings to single and multi-parameter sensing,* Opt. Express, 4, p. 457, 1999.
29. M. Das and K. Thyagarajan, *Dispersion compensation in transmission using uniform long period fiber gratings*, Opt. Commun., 190, p. 159, 2001.
30. F. Levison, *WDM Solutions*, Laser Focus World, 2000.
31. V. Rastogi and K. S. Chiang, *Long-Period gratings in planar optical waveguides*, Appl. Opt., 41, p. 6351, 2002.
32. H. C. Tsoi, W. H. Wong, and E. Y. B. Pun, *Polymeric long-period waveguide gratings,* Photonics Technology Letters, IEEE, 15, p. 721, 2003.
33. K. S. Chiang, K. P. Lor, C. K. Chow, H. P. Chan, V. Rastogi, and Y. M. Chu, *Widely tunable long-period gratings fabricated in polymer-clad ion-exchanged glass waveguides*, IEEE Photon. Technol. Lett., 15, p. 1094, 2003.
34. K. S. Chiang, C. K. Chow, H. P. Chan, Q. Liu, and K. P. Lor, *Widely tunable polymer long-period waveguide grating with polarization-insensitive resonance wavelength,* Electron. Lett., 40, p. 422, 2004.

35. K. P. Lor, Q. Liu, and K. S. Chiang, *UV-written long-period gratings on polymer waveguides*, IEEE Photon. Technol. Lett., 17, p. 594, 2005.
36. K. Finsterbusch, N. J. Baker, V. G. Ta-eed, B. J. Eggleton, D. Choi, S. Madden and B. L. Davies, *Higher-order mode grating devices in As_2S_3 chalcogenide glass rib waveguides*, J. Opt. Soc. Am. B, 24, p. 1283, 2007.
37. M. Kwon and S. Shin, *Tunable notch filter using a thermooptic long-period grating*, J. Lightwave Technology, 22, p. 1986, 2004.
38. M. Kwon and S. Shin, *Tunable polymer waveguide notch filter using a thermooptic long-period grating*, IEEE Phot. Tech. Lett., 17, p. 145, 2005.
39. A. Yeniay, R. Gao, K. Takayama, R. Gao, and A. F. Garito, *Ultra-low-loss polymer waveguides*, Journal of Lightwave Technology, 22, p. 154, 2004.
40. A. Perentos, *Polymer waveguide grating assisted directional couplers for WDM monitoring*, Thesis for degree of Doctor of Philosophy, RMIT University, Melbourne, Australia, 2005.

Chapter 4.

Nanolithography: Applications of Photolithographic Standing Waves

4.1 Introduction

In Chapter 3, the photolithographic process was demonstrated and the resulting photoresist patterns were used as master structures for PDMS replication. In this chapter an unexploited artifact in photolithography is identified and used to demonstrate two novel nanolithography techniques. These represent an evolution of the lithographic and replication processes that were employed in Chapter 3.

This chapter begins with a brief overview of existing nanofabrication technologies.

4.1.1 Nanofabrication

In December of 1959, Richard Feynman incited the scientific community to pursue the nano regime with his visionary talk "There's plenty of room at the bottom". It was around this same time that the first photolithographic mask aligners were being commercially

deployed for the production of integrated circuits. Since then, there has been remarkable progress in miniaturization.

The semiconductor industry has been the main driving force behind size reduction in its pursuit of increased transistor density, which has simultaneously increased computing power and reduced device costs. This progress was aptly predicted by Moore's law, which states that the number of transistors in an integrated circuit would double roughly every 18 months. The continual evolution of the industry's photolithographic techniques saw it first cross the 100 nm feature threshold and enter the nano-regime in 2003. Recently, this multi-billion dollar industry moved to the routine fabrication of 45 nm half-pitch features [1].

Today, nanoscale fabrication has moved out of the confines of the electronics industry and has found application in fields as diverse as biology, medicine and photonics. Unfortunately, as diverse and widespread as the demand for nanofabrication has become, the billion dollar cost of establishing a nanoscale photolithographic facility remains prohibitive, not to mention the fact that photolithography is unsuitable for the patterning of many sensitive biological materials.

Alternative technologies such as electron-beam [2] and focused ion-beam lithographies are available, and these even offer improved resolution capabilities down to <10nm, with the additional capacity for fabricating in three dimensions [3]. However the cost of this equipment is still significant, and their serial write nature makes them unsuitable for anything other than prototyping.

These scanning beam lithographies, together with photolithography, can be classified as top-down fabrication techniques, wherein material is removed from a planar bulk to reveal the desired nanostructures. The opposite approach, which has largely been dominated by the field of chemistry, is bottom-up fabrication. Here, aggregates of atoms are synthesized and coerced to self-assemble into large bulk quantities of nanostructures. The forms of these nanostructures are many and varied, and are specified by careful control of the synthesis conditions. Familiar examples are carbon nanotubes and self-assembling semiconducting oxide structures [4,5]. However, the products of self assembly are typically large disordered volumes of nanostructures, and so do not directly challenge top/down techniques.

This has created a research climate in which there is a demand for nanofabrication but unsatisfactory access to techniques which in themselves may not satisfy fabrication requirements. As a result, recent years have seen the development and the proliferation of numerous unconventional nanofabrication techniques [6,8]. While it is beyond the scope of this introduction to provide a comprehensive overview of every one of these unconventional techniques, it is illustrative to acknowledge that the contributions to this growing field are just as diverse as the demands for it.

4.1.2 Elastomeric masks

A common thread through the development of unconventional nanofabrication techniques has been their economical use of resources and ingenious adaptation of existing technologies. Prime among them has been the development of one of the conceptually simplest patterning techniques – that of molding. This development has resulted in a suite of techniques that use casts in a variety of applications. In Chapter 3, casts were used as molds for replication, however many other uses have been demonstrated, including their use as stamps for the transfer of material and as masks for photolithography. When applied as photolithographic masks, their flexibility offers functionality not provided by rigid masks. Namely, they are able to nondestructively conform to a photoresist surface, thus granting unparalleled stability between the mask and photoresist, while also providing access to the optical near-field of the mask.

Several implementations of elastomeric masks have been demonstrated already, each employing different masking mechanisms and different translations of mask pattern to photoresist pattern. The light-coupling mask [9,10] is the simplest implementation, as illustrated in Figure 4.1a, and consists of rectangular recesses which create air chambers when the mask is mated to the photoresist. Light that is normally incident on these chambers will be reflected once at the PDMS/air boundary, and again at the air/photoresist interface, resulting in low energy exposure of the photoresist below. In contrast, the raised ridges in the PDMS will conform to the photoresist, providing incident light with almost uninterrupted access to these regions. This difference in exposure energy allows a pattern to be developed from the photoresist.

A more complicated implementation is the transparent-reflective mask [11] as shown in Figure 4.1b. Here the sidewalls of the PDMS recesses are sloped at 54^{o} by casting against anisotropically etched Si(100) masters. The sloped sidewalls totally internally reflect incident light and prevent it from entering the photoresist. In transferring the mask pattern, this approach reduces its feature sizes and halves its period.

More elegantly, the elastomeric phase mask [12] has demonstrated that by tuning the depth of the rectangular air chamber in the light-coupling mask, the phases of the wavefronts that enter the photoresist through either an air gap or a PDMS coupled region can be tuned relative to one another. A high energy dose is used to overcome the energy difference between coupled and air gap regions, while a recess depth of 400 nm induces a π radian phase shift and creates intensity nulls beneath the sidewalls of the mask features, where the neighbouring wavefronts overlap. Initial implementations of this technique demonstrated 90 nm wide features [12,13], while more recent improved results have achieved 50 nm [14,15] and even 30 nm [16]. Applications of this mask include surface acoustic wave transducers [17] and light emitting diodes [18]. The mask is illustrated in Figure 4.1c.

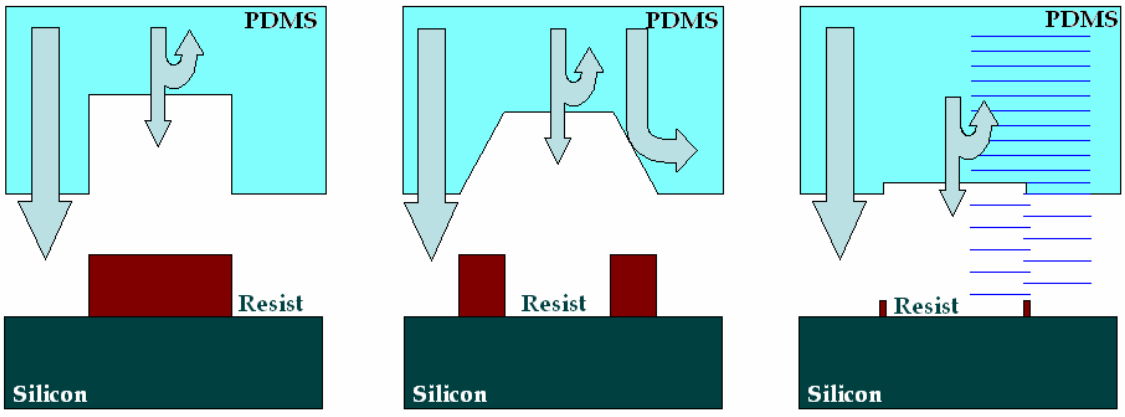

Figure 4.1: Various implementations of elastomeric photolithography mask, showing mask profiles (top) and the resulting positive photoresist structures (bottom). From left to right: (a) the light coupling mask, (b) the transparent-reflective mask, and (c) the phase mask.

4.1.3 Line of sight deposition

Another unconventional approach to nanofabrication is the use of line-of-sight shadowing templates to discretize thermally evaporated directional fluxes. Some of the most popular templates are self-assembled, of which colloidal lithography [19] is a prime example. Here, the nanoscale triangular gaps in between close-packed monolayers of nanospheres are used as deposition masks, as illustrated in Figure 4.2a. Similarly, the combination of glancing angle deposition with thin film clustering has demonstrated dense forests of nanowires [20,21] shown in Figure 4.2b. The nanostructures demonstrated by these techniques have been employed as plasmon resonators [19, 20], ultra-low index thin films [21], and graded-index antireflection layers [22].

Other shadowing templates are more precisely engineered. For instance, photolithography has been used to define closely spaced, pillar features which have been used to shadow each other from an obliquely incident collimated flux. This has limited the deposition of material to the upper sidewalls and ceilings of the posts, as illustrated in Figure 4.2c, after which they have been mechanically toppled like microdominos [23] in order to translate the nanometer thickness of the deposited material into nanometer lateral dimensions.

Recently, Melosh et al. [24] demonstrated that selectively etching a GaAs/AlGaAs superlattice cross-section would create a corrugated edge of protruding GaAs layers and recessed AlGaAs layers. Line of sight deposition could then be used to selectively coat the protruding layers to create lengths of nanowire, as shown in Figure 4.2d, that had widths and pitches as small as 8 nm and 16 nm respectively. These nanowire deposits were then mechanically transferred from the supperlattice template onto a planar substrate, where they have found numerous applications. The wires have been used as etch masks to create single crystal silicon nanowires [25], they have been transferred to flexible, transparent, elastomeric substrates [26] and they have been incorporated in transistors [27]. The scale and density of these straight-line nanowires reportedly exceeds the capabilities of electron-beam lithography.

Similar nanoscale corrugations can be found on the sidewalls of features that have been fabricated by deep reactive ion etching (DRIE). These corrugations have also been

demonstrated to be suited to nanowire fabrication. One approach created nanowires from the very silicon that was being etched. This was accomplished by defining narrow bottlenecks in between larger features. These bottlenecks were narrow enough for the corrugations on either sidewall to etch through the line and meet each other, thus turning the narrow line into vertically stacked nanowires that were suspended in between the larger features [28]. A second technique, demonstrated by Rogers et al. [29], used the sidewall corrugations in silicon as shadow masks in the path of a collimated flux of metal to create isolated metal lines, similar to the Melosh demonstration. The widths of these lines were defined by the thickness of the deposited material, while their heights were less than the vertical periodicity of the corrugations, as illustrated in Figure 4.2e. However, these deposits were only intermediaries to a further objective. They were then used as masks during the lateral wet-etching of the silicon, to create vertically stacked silicon nanoribbons that had thicknesses below 100 nm.

4.1.4 Summary

The variety and accessibility of techniques such as those described above have transformed nanofabrication into a vigorous, multidisciplinary field of research. In photonics specifically, the utility of nanostructures is derived from their subwavelength size relative to the visible spectrum. Relatively new fields in photonics that have developed due to these advances include plasmonics and surface-enhanced Raman spectroscopy.

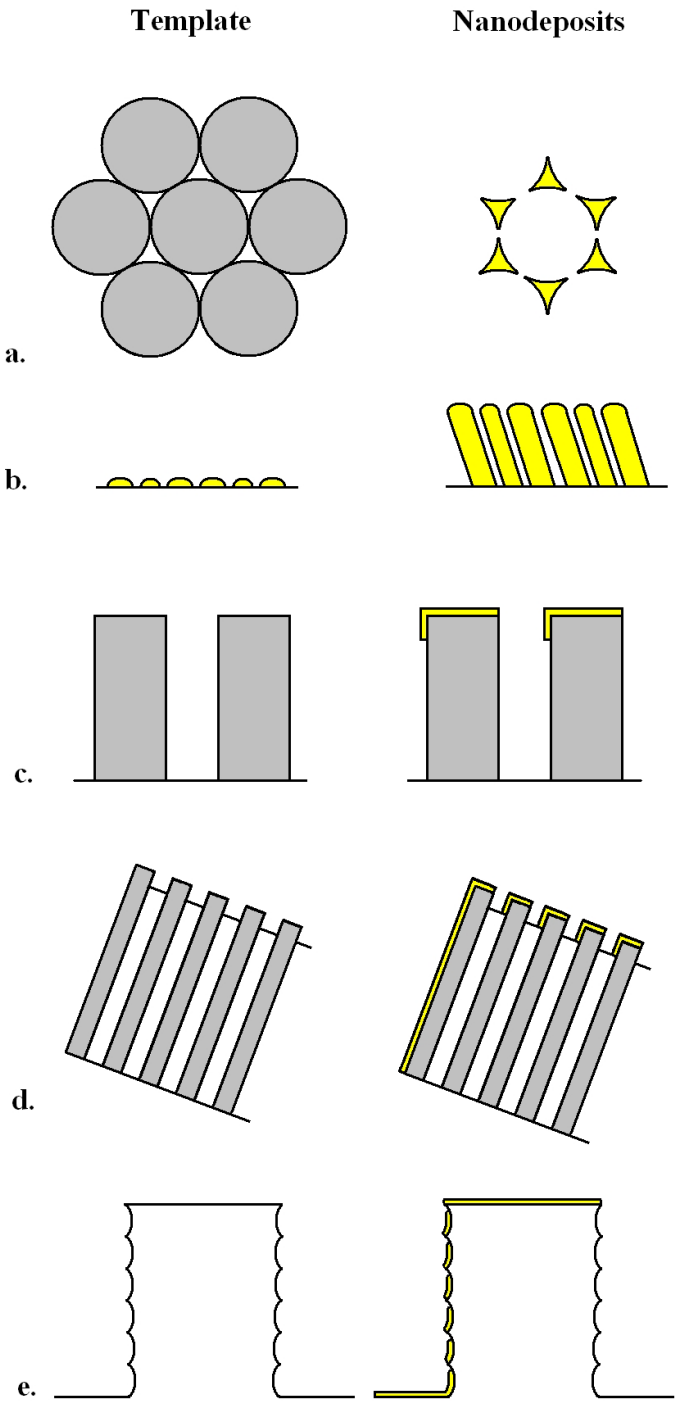

Figure 4.2: An illustration of several nanofabrication techniques that depend on the directional deposition of metals. The nanotemplates on the left are (a) colloids / nanospheres, (b) clustered thin films, (c) photolithographically defined posts, (d) selectively etched superlattice cross-section and (e) DRIE silicon lines. The right hand column shows the nanoscale deposits after directional coating with metal. The nanospheres are coated at normal incidence, while the rest are coated obliquely.

4.2 Contact photolithography

The modesty of a decades old technique like contact photolithography is acutely evident when contrasted against the nanofabrication schemes discussed in Section 4.1. Optical diffraction limits and the use of rigid masks restrict its minimum feature sizes to approximately 1 μm, and these can only be fabricated in a two-dimensional plane. Despite these limitations, contact photolithography has several outstanding attributes that have made it a mainstay of research laboratories around the world. The manual mask-aligners are often simple to maintain and operate, and as a direct result of the long evolution of the semiconductor industry, they are a ubiquitous technology. Additionally, fabrication is conducted in a parallel fashion, such that substrates that are inches in diameter can be patterned in moments with features that are completely arbitrary in shape.

4.2.1 Photolithographic standing waves

The presence of optical interference effects in photolithography is an inescapable consequence of its reliance on optical illumination. A notorious artifact of this interference is the optical standing wave corrugation.

Optical standing waves are established within thin films of photoresist during the normal incidence illumination that is necessary for pattern transfer. Standing waves are the product of interference between the incident illuminating wavefronts and the wavefronts that are reflected by the substrate [30,31]. This interference pattern distributes power within the photoresist into vertically stacked planes of alternating high and low energy, as shown in Figure 4.3. Once the photoresist is developed, this energy distribution serves to add regular structure to the photoresist that is oriented orthogonal to the plane of the transferred pattern. These corrugations are typically associated with reduced linewidth resolution and are routinely suppressed with anti-reflection coatings [32,33], post exposure bakes [34,35] and broadband exposures.

The dimensions of these standing wave sidewall corrugations are distinctly nanoscale. They have a vertical periodicity on the order of 100 nm, and a similar depth

into the sidewalls. These dimensions, combined with their natural occurrence in a technique as ubiquitous as photolithography and their routine suppression to date, makes them an attractive candidate for the development of novel nanofabrication techniques.

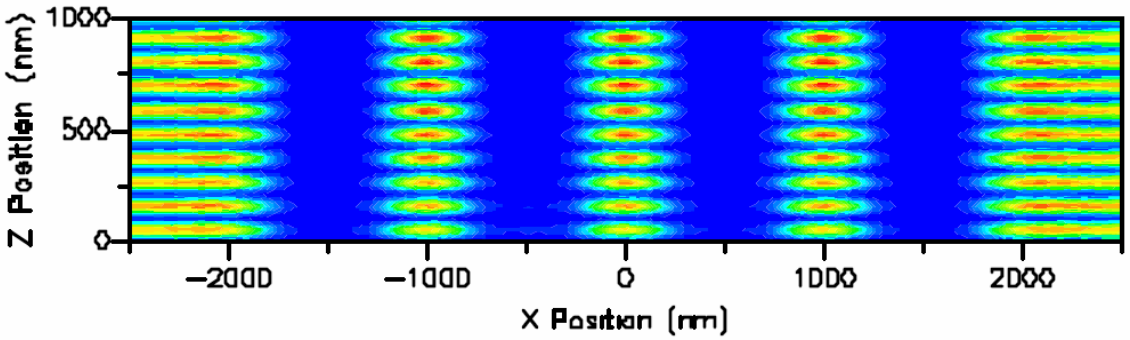

Figure 4.3: Representation of the distribution of optical power within a film of photoresist by the standing wave interference pattern [C. A. Mack, *Lithographic Simulation Review*, SPIE, 4440, p. 59, 2001].

4.2.2 Proposal

This chapter explores the potential of sidewall standing wave corrugations to be exploited as templates for unconventional nanofabrication. Two approaches are investigated. The first is a novel implementation of an elastomeric mask, which is applied to planar patterning on the nanoscale. The second adapts the concepts demonstrated by Melosh [24] and Rogers [29] to present a novel technique for fabricating nanowires in three-dimensions.

4.3 PDMS Scattering Mask

In this first investigation, a novel form of elastomeric edge-lithography mask is proposed. The functionality of this mask is derived from the elastomeric nature of PDMS, which allows it to cast undercut or re-entrant structures without damaging either the master or itself.

Dramatic examples of such casting can be found in the literature, where micron scale undercuts are found in the replication of micro-zippers [36], microresonators [37], lenses [38] and complex two-photon polymerized structures [39]. Casting of more subtle

undercuts can also be found in applications such as nanotransfer printing, where masters structures have been engineered to have t-shaped undercuts of 100 nm [40] and less than 50 nm [41]. Of similar dimensions are the submicron scallops observable on PDMS sidewalls which have been transferred from masters that are patterned by the sequential etching and passivation steps of inductively coupled plasma (ICP) etching [42]. These scallops are equivalent to those illustrated in Figure 4.2e.

This investigation examines whether undercut sidewalls such as those described in the above literature can be used as masking elements in a novel implementation of nanoscale, elastomeric, edge-lithography mask. Standing wave sidewall corrugations from a photoresist template are employed as analogs to the ICP scallops described above. Their fabrication is described, they are transferred to an elastomeric cast, and their utility as optical masking elements for nanoscale edge-lithography is examined. The proposed procedure is illustrated in Figure 4.4.

4.3.1 Corrugated master structures

The successful fabrication of distinct sidewall corrugations in photoresist depends on the selection of a substrate that is appropriately reflective. Polished silicon wafers are appropriate because of their optical smoothness and their status as the standard substrate for the semiconductor industry, which makes them readily available. These substrates are used for all of the work in this chapter.

The silicon wafers are prepared for photolithography by first scrubbing with acetone and methanol, rinsing with deionized water and then dehydrating at 110^{o}C for 20 minutes in a convection oven. The adhesion promoter hexamethyldisilazane (HMDS) is then spin coated at 1500 rpm for 20 seconds. The wafer is then coated with AZ5206E photoresist from Clarient.

Patterning the corrugated master photoresist pattern requires the selection of an appropriate photolithographic system. For this demonstration a Karl Suss MJB3 contact mask aligner with a 350W Hg lamp has been used. Additionally, for this first technique, this mask aligner is operated in broadband mode, the spectrum of which is shown in Figure 4.5. This decision to use simple equipment in the simplest of configurations has

been made in order to emphasize the accessibility of these novel nanofabrication techniques.

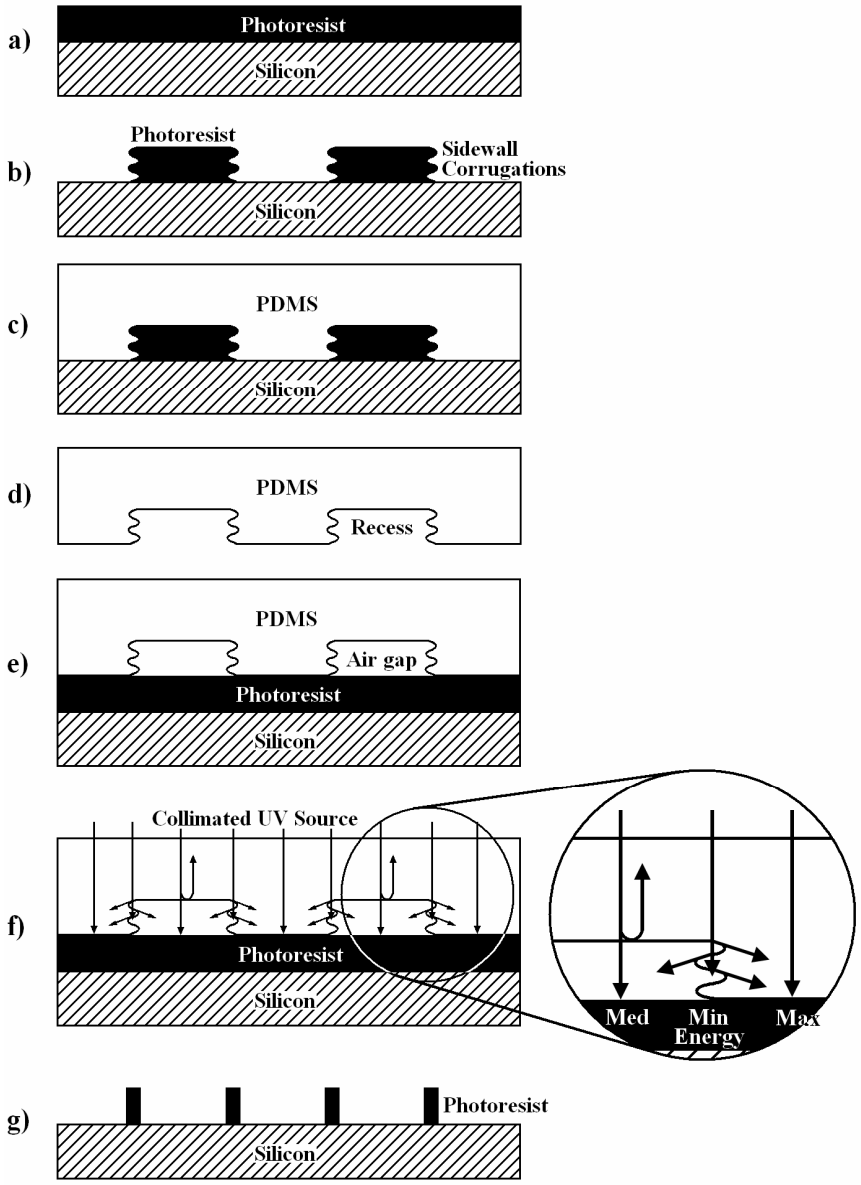

Figure 4.4: The fabrication and application of a PDMS scattering mask. (a) A master structure is realized by spinning a layer of photoresist onto a reflective substrate, in this case a polished silicon wafer, which is (b) photolithographically patterned using a quartz mask. (c) Casting PDMS against this structure realizes (d) the PDMS scattering mask. This mask is (e) applied by conforming it to the surface of a new layer of photoresist and (f) illuminating the photoresist through the scattering mask. (g) Developing produces nanometer line widths.

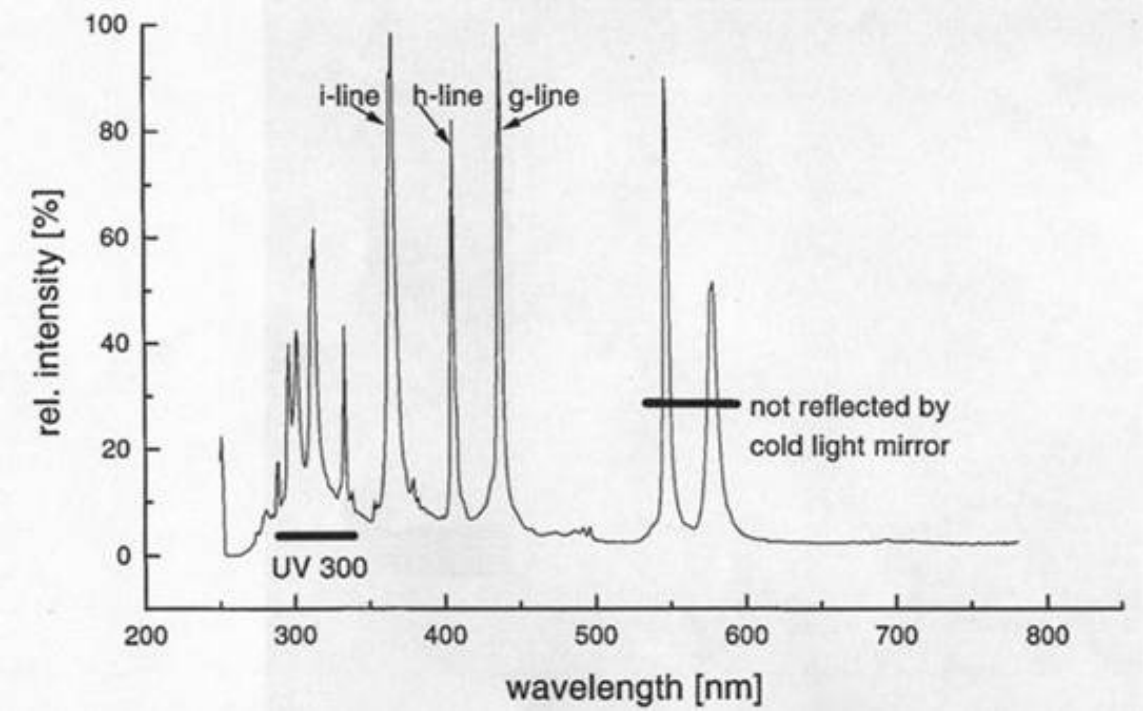

Figure 4.5: Mercury lamp spectrum, showing the peaks employed during broadband illumination, and the restricted bandwidth defined by the UV300 lens. This spectrum was provided by Coltronics.

Patterning a thicker film of photoresist reveals the character of the standing wave corrugations that are generated by broadband illumination, as shown in Figure 4.6. It is clear that the corrugations become progressively shallower as their distance from the substrate increases. After about three corrugations, the sidewall is smooth and characterized by a gentle negative slope. This decay is the result of the numerous wavelengths that are present in the broadband source, as shown in Figure 4.5, which rapidly move out of phase and dilute the standing wave as they move away from their plane of reflection.

Note that the section of sidewall that supports the corrugations has a positive slope, which acts to offsets them relative to one another. In order to minimize the nanoscale dimensions of the structures produced by this mask, the lateral confinement of these potential masking structures needs to be optimized. To this end, the thickness of the film of photoresist is limited so that it can only sustain the bottom two corrugations. This restriction will demonstrate that masking is being performed by the corrugations rather

than the sloping sidewall, which is the active element in the transparent-reflecting mask, as illustrated in Figure 4.1b.

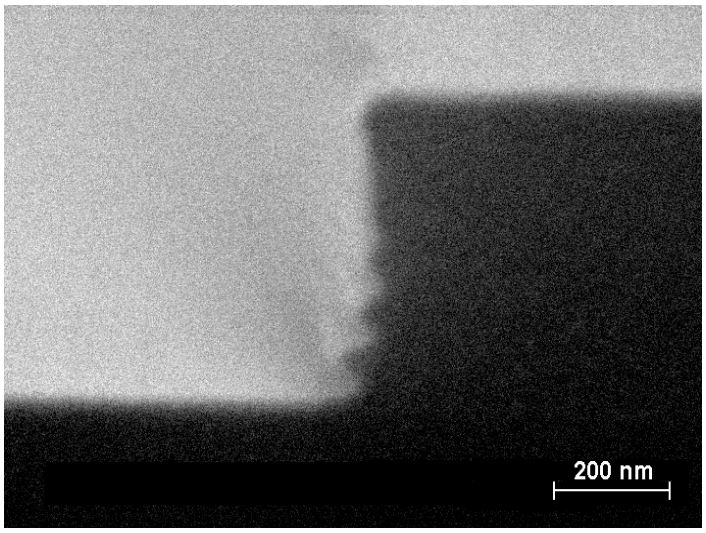

Figure 4.6: An SEM image showing a cross section through a photoresist step. The corrugations created by broadband illumination are visible.

The reduced film thickness was achieved by spinning the photoresist in a closed lid configuration at 3300 rpm for 30 seconds. The closed lid process traps solvents close to the photoresist during the spinning process, allowing in this case, the formation of a 200 nm thin film. A 5 minute softbake was then conducted at 90^{o}C on a hotplate to expel solvents. Figure 4.7a shows the silicon substrate coated with photoresist.

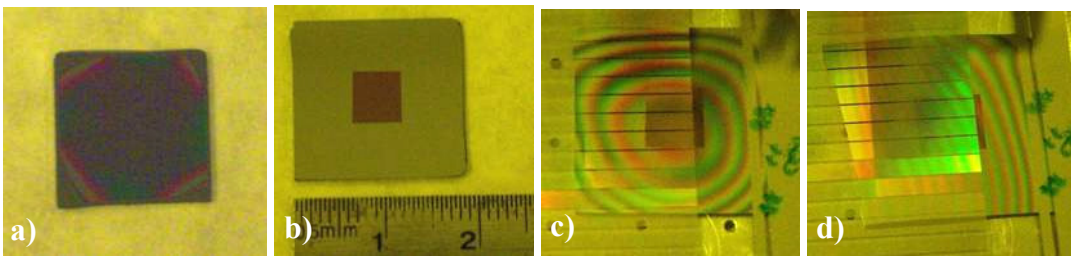

Figure 4.7: A photograph of (a) a typical silicon substrate shows complete coverage by photoresist, as well as the thick edge-beads at the corners. (b) Edge bead removal isolates the flat central region of photoresist. Near-conformal contact (desirable) with the mask (c) is indicated by the lack of interference fringes across the photoresist, while (d) a sloping gap is indicated by straight fringes across the photoresist.

Edge-bead removal was then performed to eliminate the thick photoresist edge beads from the perimeter of the silicon wafer and to isolate the flat central region of the photoresist film, as shown in Figure 4.7b. This was achieved by exposing all but the central region, and then immersing in developer. The photoresist was then loaded into the mask aligner, firmly pressed against a chrome-on-quartz mask, and a pattern of micron wide straight lines was exposed using a 10 second illumination at approximately 9mW/cm^2. The exposed photoresist was soaked in chlorobenzene for 15 seconds, rinsed with deionized (DI) water, and the patterns were developed for 10 seconds in a 1:4 dilution of AZ400K developer (Clariant) in DI water. The fabrication of the master pattern was completed by rinsing in DI water. Cross sections are shown in Figure 4.8.

While Figure 4.8a and 4.8b represent ideal cross sections in regards to vertical stacking of the corrugations, it is important to acknowledge that the sidewall slope was not always reliably eliminated. Regardless, the strategy that was employed was to use chlorobenzene, which was used in Section 3.3.2 for creating t-topped profiles, to reduce the solubility of the top corrugation and thus subtly extend its protrusion. Figure 4.9a demonstrates an instance in which the photoresist ceiling and the top corrugation are misaligned, in which case the chlorobenzene had no effect on the slope. It can be seen that the 10 second soak time in Figure 4.9b will not quite correct the slope, while the extended soak time of 60 seconds in Figure 4.9c seems to reverse it.

Although the results presented here demonstrate that the effects of chlorobenzene on sidewall slope are cumulative, it is suspected that the reason for its occasional failure to correct the slope is because both the quality of the contact between mask and photoresist and the developing time also play an important role in defining the magnitude of the sidewall slope. Neither of these parameters were investigated in detail for the preparation of the elastomeric mask. (Future investigations of this process should be aware that chlorobenzene is a toxic chemical that must be handled with care.)

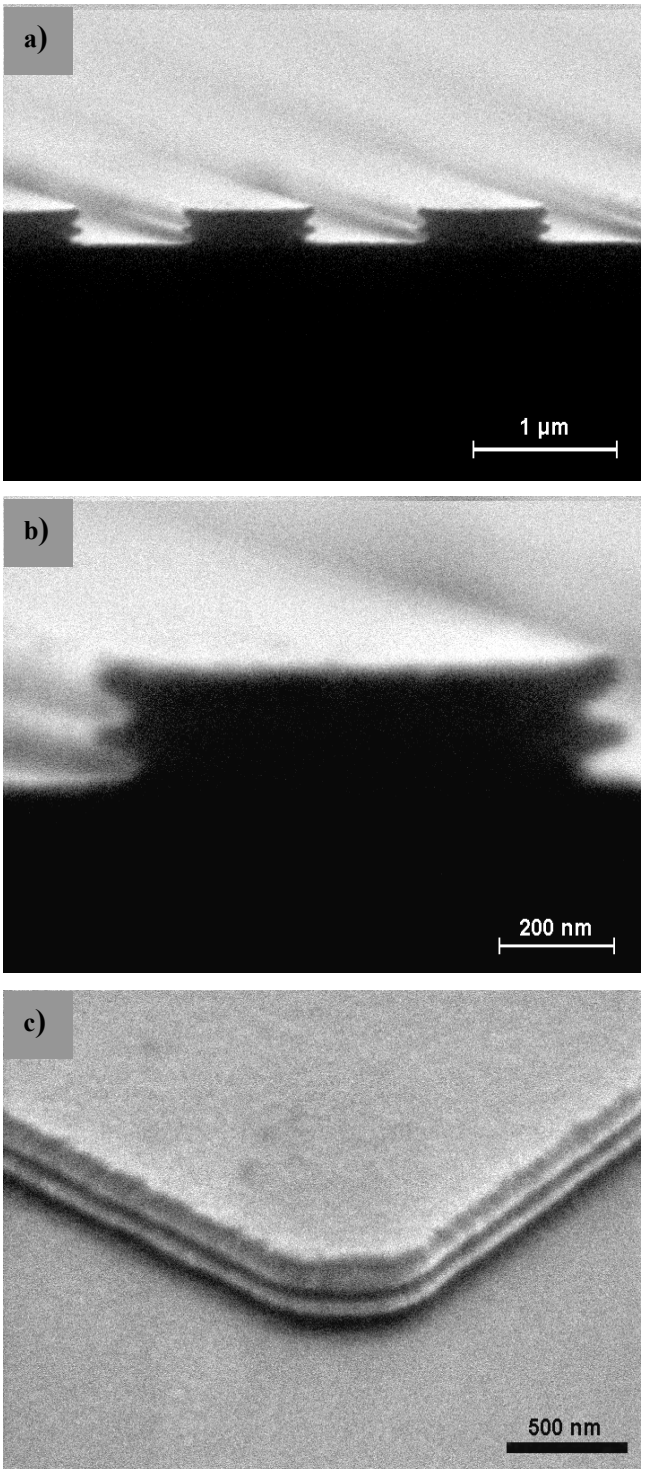

Figure 4.8: SEM images showing cross sections through the corrugated photoresist master patterns. A broad view in (a) demonstrates the regularity of the corrugations over several features, while a close up (b) demonstrates their vertical alignment and their depth. The continuity of the corrugations around corners is shown in (c).

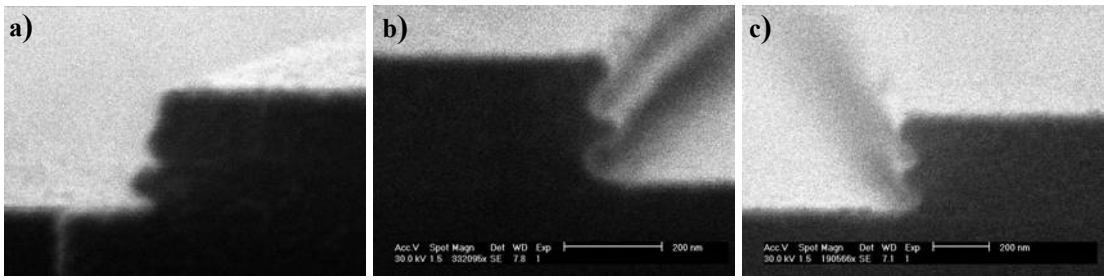

Figure 4.9: SEM images of cross sectioned master patterns demonstrate the use of chlorobenzene to manipulate the sidewall corrugations. Mismatching the top corrugation and the photoresist ceiling (a) results in a failure of the chlorobenzene to correct the sidewall slope. Conversely, a 10 second soak of an appropriately thick layer results in (b) inadequate correction, while a 60 second soak (c) overcompensates and reverses the slope.

4.3.2 Casting the corrugated photoresist

The scattering mask was produced by casting against the corrugated photoresist pattern shown in Figure 4.8a and 4.8b. A 10:1 mixture of PDMS (Dow Corning 184 Silicone Elastomer Kit) was prepared and degassed for 20 minutes before being poured over the master pattern. Degassing was then repeated to ensure complete filling of the photoresist master pattern, after which it was cured at 60^{o}C for several hours in a convection oven.

After curing, the photoresist pattern was peeled from the PDMS bulk to produce a 5 mm thick sheet of PDMS with surface recesses. The recesses corresponded to the photoresist features, and on the sidewalls of these recesses are the standing wave corrugations, as illustrated in Figure 4.4d and shown in Figure 4.10. This is the PDMS scattering mask.

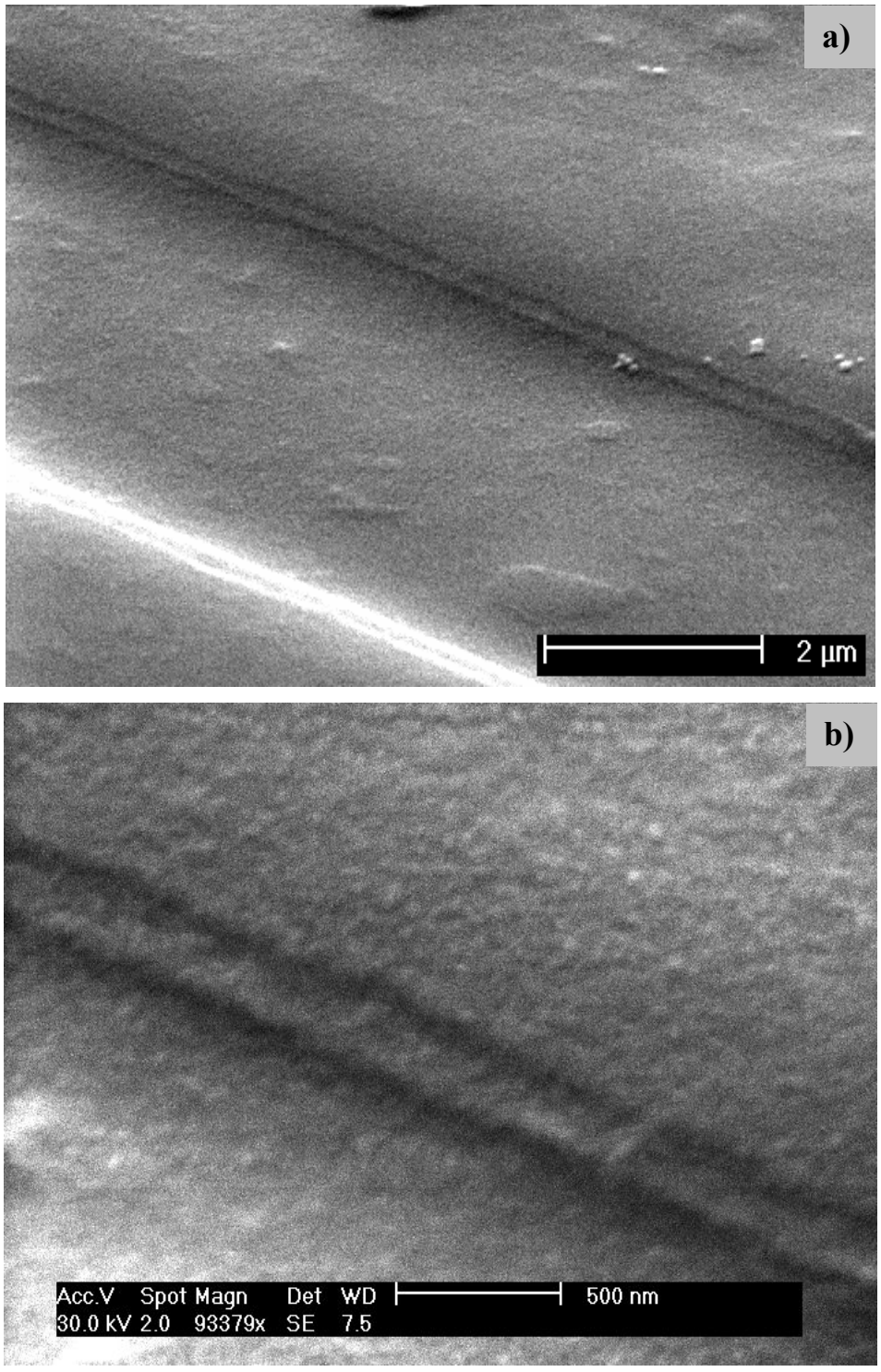

Figure 4.10: SEM images of a corrugated PDMS sidewall. Samples were sputter coated with a thin film of gold prior to imaging. A broad (a) and close-up view (b) are shown.

4.3.3 Photolithography with the PDMS scattering mask

The scattering mask was utilized by allowing it to conform to the surface of a freshly prepared layer of AZ5206E photoresist and illuminating it with the same mask aligner that was used to create the master pattern. The scattering mask presents the normally incident planar wavefront with three distinct paths to the photoresist below it, illuminating the photoresist with three distinct energies, as illustrated in Figure 4.4f.

Maximum energy is received by photoresist that is in conformal contact with the PDMS, as described in Section 4.1.2. Slightly less energy is received by photoresist directly below the PDMS recesses since incident light is presented with a PDMS/air and then air/photoresist interface. Finally, minimum energy is received by photoresist directly beneath the corrugated sidewalls since the wavefront is presented with multiple vertically stacked PDMS/air and air/PDMS interfaces. The light that intercepts these sidewall corrugations is scattered and largely prevented from entering the photoresist. Thus the sidewall corrugations are employed as the dominant masking components in an otherwise relatively transparent bulk of PDMS.

This distribution of energies has been verified by intentionally underdeveloping photoresist that has been exposed through the scattering mask to observe its progressive development, as shown in Figure 4.11. Photoresist residue is clearly observed in regions that correspond to recesses in the scattering mask, while photoresist that made contact with the PDMS is fully developed. Figure 4.11a indicates that rather than a fixed dose, there may be a distribution of energy that is received by photoresist below the air gap, as evidenced by the rib in the central region. It is suspected that the slightly larger energy received by either side of this rib may have originated from light that was deflected from the scattering sidewalls of the PDMS mask.

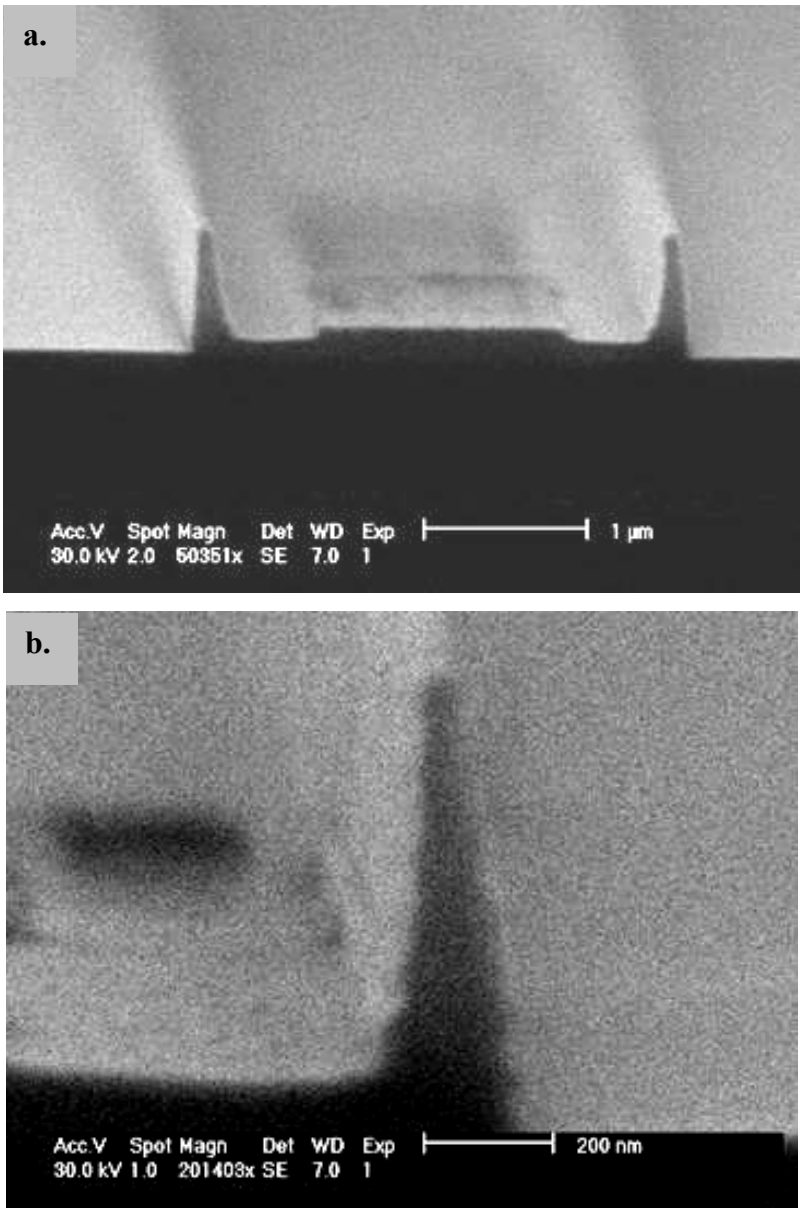

Figure 4.11: SEM micrographs showing cross sections through incompletely developed patterns that were exposed through the PDMS scattering mask. The thickness of photoresist present in each region is indicative of the transparency of the different sections of the mask. Broad view (a) and close-up views (b) are shown.

Completely developing the exposed photoresist realizes the ~80 nm wide lines shown in Figure 4.12, whose positions correspond to the sidewalls of each of the master photoresist ribs. Ironically, some broadening of the line width from ~80 nm to ~100 nm can be seen at the centre of the rib as a result of standing waves. The realized features are unbroken, and since they were realized in a 200 nm thick layer of resist, demonstrate an

aspect ratio of 2.5:1. Aspect ratios of 10:1 have been realized as shown in Figure 4.11 and Figure 4.12d, by using a scattering mask with 800 nm deep recesses, derived from the corrugated photoresist in Figure 4.6, however these features exhibit significant broadening in cross-section as they approach the substrate, The 80 nm feature width can be seen to taper to ~200 nm over a height of ~800 nm.

In order to eliminate destructive interference as a possible contributor to the masking mechanism in this scattering mask, consider that the phase shifts induced by the 200 nm and 800 nm recesses implemented here have been calculated to be $2\pi/5$ and 2π radian respectively, effecting constructive interference. This is in stark contrast with the π phase shift induced by the 400 nm recesses in the elastomeric phase mask [12].

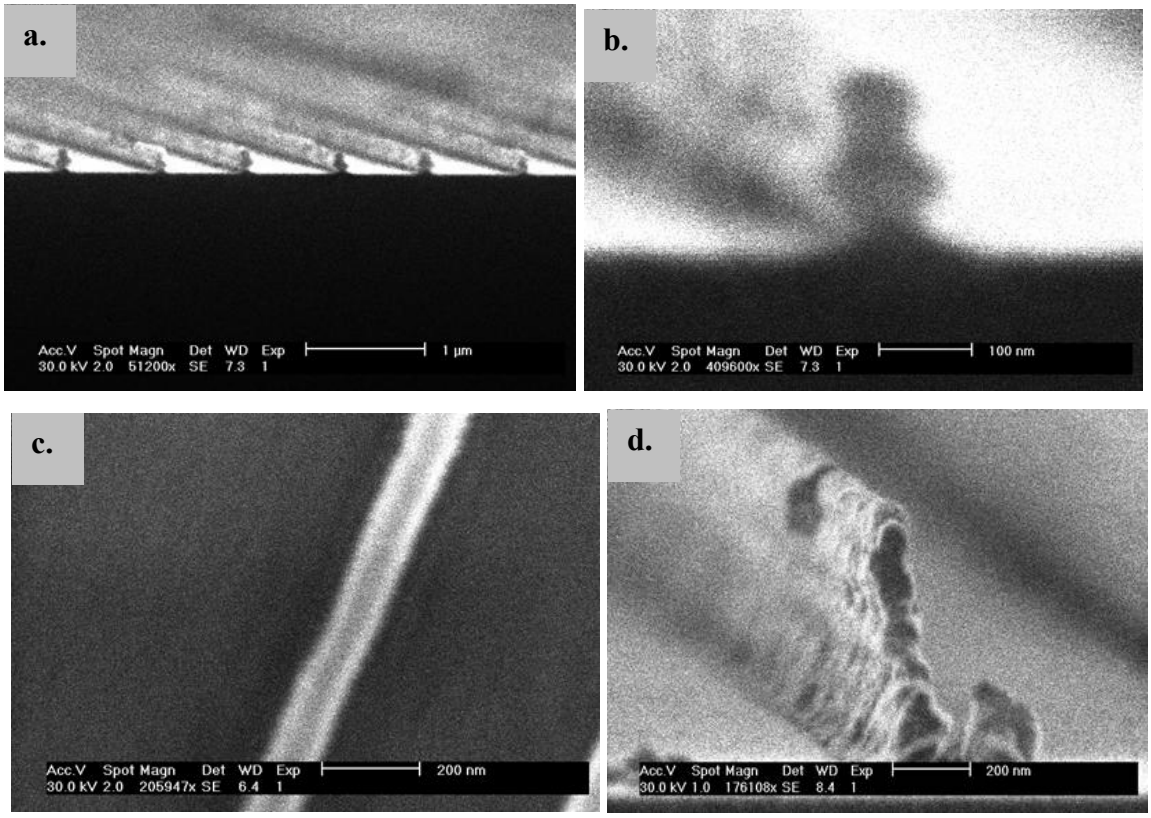

Figure 4.12: SEM micrographs showing nanometer wide lines of photoresist created by the PDMS scattering mask. Broad view and close-up are shown in (a) and (b), while (c) shows a top down view. A higher aspect ratio feature is shown in (d).

4.3.4 Lift-off with the PDMS scattering mask features

As a potential application of these photoresist features, their transfer to a metal film is demonstrated. The photoresist features in Figure 4.12 were coated with 50 nm of gold at normal incidence using a Balzers electron beam coating unit. The coated photoresist was then immersed in an acetone bath and subjected to a gentle mechanical scrub using a cotton swab. This resulted in the dissolving of the photoresist features, and the creation of nanoscale trenches in the gold, as shown in Figure 4.13. Excellent correlation is again demonstrated between the width of the gold trenches and the depths of the sidewall corrugations in the master pattern. Continuity of the trenches around corners can also be seen in Figure 4.13c. The narrower than expected line width in this curved line is attributed to overdeveloping.

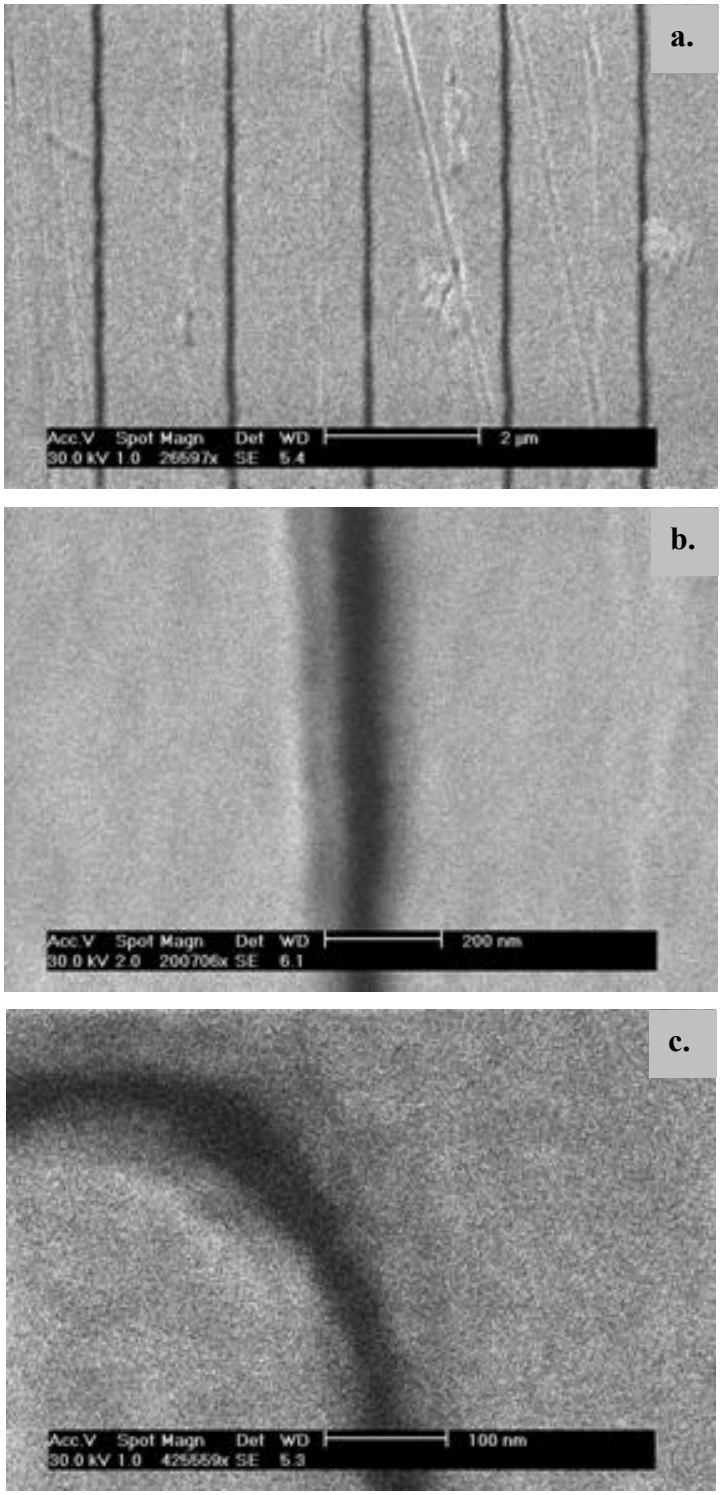

Figure 4.13: SEM micrographs showing nanometer wide channels in a layer of gold, created by coating photoresist patterns that were defined by the scattering mask, and then dissolving the photoresist. The three images show (a) a broad view and close-ups of (b) a straight line and (c) a curved line. Scale bars are 2 µm, 200 nm and 100 nm.

4.3.4 Discussion

Feature dimensions produced by the PDMS scattering mask are defined by how well the sidewall corrugations are confined horizontally, as well as the depth of the corrugations themselves. For the photoresist used in this case, it was found that the corrugations on the master pattern could be more easily stacked vertically when using a thinner film of photoresist.

Standing wave corrugations are present irrespective of photoresist film thickness, as demonstrated by a comparison of the sidewall corrugations in Figure 4.8b and those in the thicker layers of photoresist in Figure 4.6 and 4.8c. The downward reflections of the vertically traveling wavefront from the photoresist/air interface are too weak to significantly dilute the standing wave interference pattern that is generated by the normally incident and substrate reflected wavefronts. A significant advantage of this fact is that the scattering mask technique retains its functionality in the presence of processing tolerances that may lead to variations in master photoresist thickness.

Some simple limitations on master fabrication are set by the elastomeric properties of the mold material and apply to all variations of elastomeric mask. Broad ribs on the master will translate to broad recessed regions which are subject to sagging. This sagging may result in subtle deformation of the mask sidewalls, or if the recess width-to-height ratio is too great, the complete collapse of these recesses. This collapse was observed to occur at 7 μm line widths for 200 nm deep recesses in a 10:1 PDMS mix, wherein the PDMS cast loses its masking ability since the recess ceilings contact the photoresist. It is expected that the scattering mask technique would benefit from the use of a more rigid elastomer, as has been demonstrated in the evolution of the elastomeric phase mask [15,16].

It is speculated that nanofeatures that are more closely spaced than those demonstrated in Figure 4.12a could be realized if the corrugated master structures are fabricated holographically. However the optical scattering during masking may impose proximity limitations on features realizable with this technique. Furthermore, casting

structures with widths on the order of nanometers may see neighboring features in the flexible mold being drawn together if their aspect ratios are too high.

Although scattering masks are limited to fabricating structures with only one specific width, it is likely that this width can be tuned by using different photoresists and processing techniques. To this end, it is noted that sidewall corrugations in the literature have been observed with depths as shallow as ~11 nm [43].

4.4 Three dimensional nanostructures

The use of a broadband illumination source for conducting photolithography, as in the scattering mask demonstration of Section 4.3, is generally considered to be a strategy for reducing the presence of standing wave corrugations, as mentioned in Section 4.2.1. Throughout the literature, prominent corrugations are consistently attributed to the use of monochromatic illumination sources [30,34].

In the remaining sections of this chapter, it is demonstrated that by restricting the illumination bandwidth used in performing photolithography, the standing wave corrugations can be made much more numerous and prominent than those employed in the scattering mask demonstration of Section 4.3. An investigation is conducted to explore the potential of these sidewall corrugations to be exploited as templates for fabricating nanoscale structures that are distributed in three dimensions. Vertically stacked nanowires are demonstrated by employing the sidewall corrugations as vertically-stacked shadow masks in the path of an evaporative flux, as illustrated in Figure 4.14.

The resulting nanowires are expected to have widths on the order of 10's of nanometers, and since photolithography can define patterns that are completely arbitrary, these nanowires could be defined along almost any delineation, from stacks of rings, to straight lengths. Furthermore, controlling the thickness of deposited material should change the cross-sectional aspect ratio of these deposits, converting nanowires into higher aspect ratio nanoribbons. Finally, since this technique is not material specific, multilayer nanowires or nanoribbons are also expected to be possible.

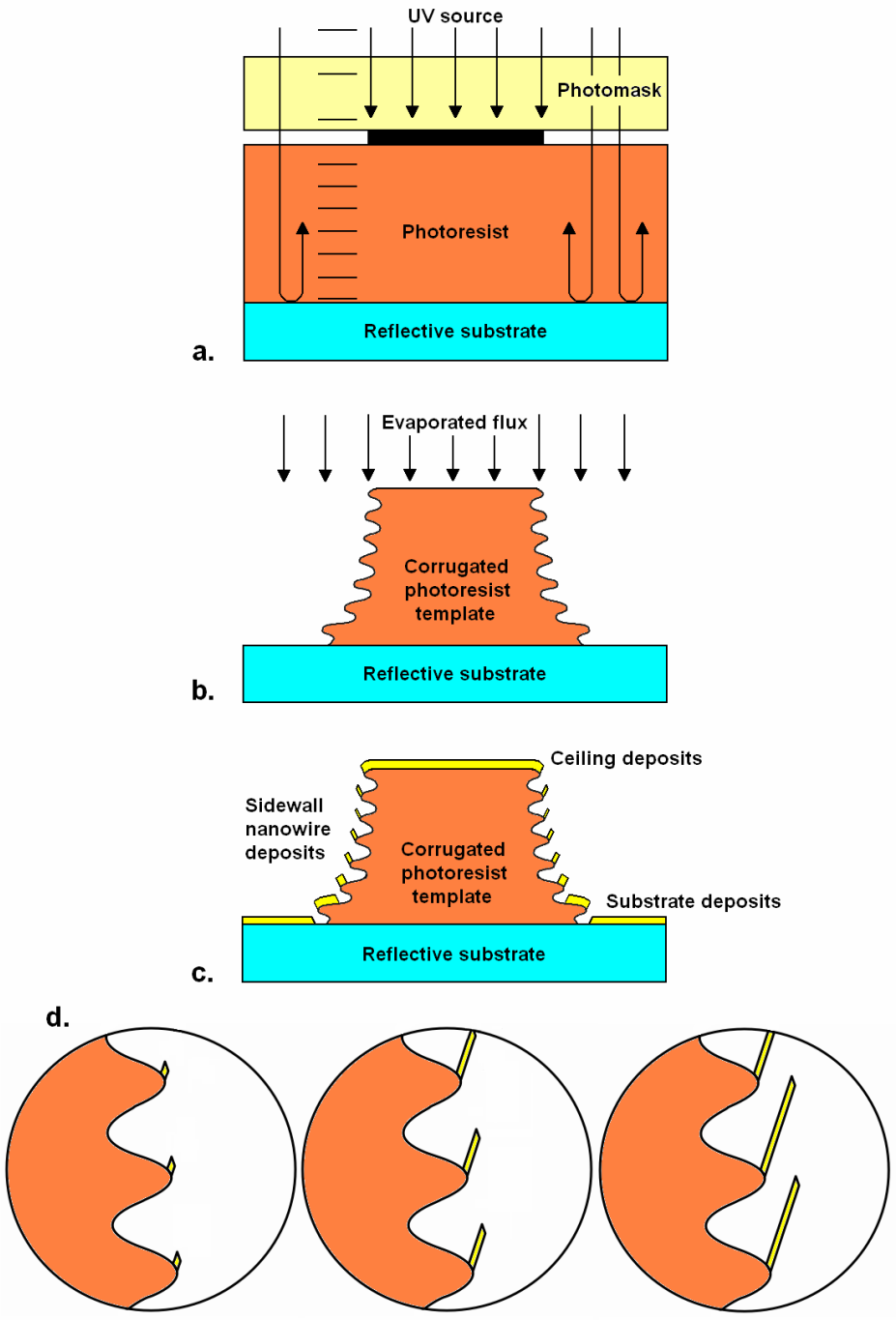

Figure 4.14: Process diagram. A film of photoresist on a reflective substrate is (a) optically exposed through a solid chrome-on-quartz mask, establishing a standing wave interference pattern. Developing the exposed photoresist produces (b) the corrugated photoresist template. Evaporating material at normal incidence results in (c) sidewall deposition and the creation of nanowires of (d) varying aspect ratios, as defined by deposited thickness.

4.4.1 Photolithography for prominent corrugations

Fabrication of the corrugated photoresist patterns began by open-lid spinning a photoresist layer at 3000 rpm to a thickness of 720 nm. A 20 minute soft-bake in a convection oven at 90^{o}C was used to dispel solvents, after which an edge-bead removal step isolated the flat central region of photoresist. This central region of photoresist had a typical surface area of ~25 mm^2, as shown in Figure 4.7b.

A Karl Suss UV300 lens filter was used to restrict the illuminating bandwidth of the Karl Suss MJB3 mask aligner to between 280 nm and 350 nm, thus approximating a monochromatic source, as shown in Figure 4.5. Mask patterns consisted of straight lines of length 2 mm and width ~1 μm and an array of 1.3 μm diameter holes. The use of a pattern of small diameter holes rather than posts was found to favorably influence the susceptibility of the photoresist pattern to overdeveloping. The larger footprint of the hole pattern, which was roughly equivalent to the 25 mm^2 surface area of the photoresist before patterning, made the hole pattern much more mechanically robust than the minute footprint of a single 1.3 μm diameter post.

The photoresist and the mask were then brought into firm contact with each other. The quality of the contact was gauged by the characteristic fringe patterns present across the surface of the photoresist. These are formed when reflections from the bottom mask face and the top of the photoresist interfere with one another. The absence of fringes across the photoresist in Figure 4.7c indicates a near conformal pressure, while the straight line fringes across the photoresist in Figure 4.7d indicates the presence of a sloping gap between the mask and photoresist. During developing, the solubility of the photoresist has been observed to vary across the photoresist surface in direct correlation with the location of these interference fringes.

4.4.1.1 Developing the corrugated photoresist template

The photoresist was exposed through the hole pattern using a 3 minute exposure. This near-saturating dose was found to be necessary for the formation of prominent corrugations, presumably because it allows for the accumulation of diffracted energy.

The exposed photoresist was then developed for 8 seconds in a 1:5 dilution of AZ400K (Clariant) in DI water, during which time the sample was agitated to avoid surface scumming of the developer. Note that agitation was a critical step in the definition of prominent corrugations, wherein omitting agitation produced very shallow sidewall features. Patterning was completed by rinsing with DI water and blow drying with Nitrogen gas. A cross section through the resulting corrugated photoresist template is shown in Figure 4.15.

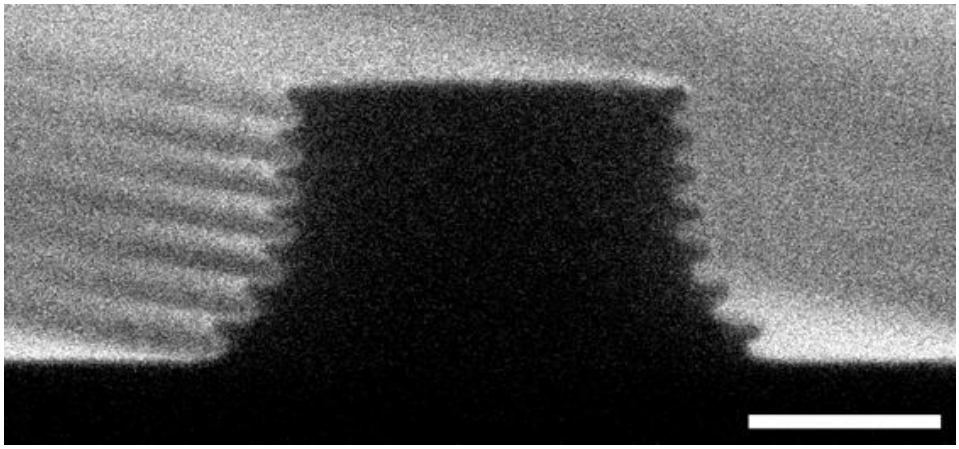

Figure 4.15: An SEM image showing a cross section through a straight line of photoresist. The prominent corrugations and the positive slope on the sidewalls are both visible. Scale bar is 500 nm.

Contrary to the requirements of the scattering mask, this three dimensional technique benefits from the presence of a sloping sidewall. As a result, developing time is a critical factor in this demonstration. When using near saturating optical energies, the positive sidewall slope originates from the top down progression of the developing process, wherein the lowest regions of photoresist are subjected to the shortest developing times.

The uniform solubility of a saturated photoresist bulk is demonstrated in Figure 4.16a. Here a photoresist film has been exposed in the absence of a mask, with the same dose that was used for producing prominent sidewall corrugations. After being exposed, this film was cross-sectioned and then briefly developed, allowing the developer to attack the exposed interior of the photoresist rather than having to progress down towards the substrate. Figure 4.16a clearly shows that the entire photoresist bulk is retreating from the

cleaved edge at the same rate. This is evidence of the uniform solubility of the saturated photoresist throughout its bulk, and emphasizes the importance of developing time in achieving positively sloped sidewalls. In contrast, Figure 4.16b shows the cross-section developing of photoresist that received a much lower exposure dose. This generates a clear positive slope that is typical of low energy positive photoresist lithography and demonstrates the presence of an energy gradient, defined by optical absorbance.

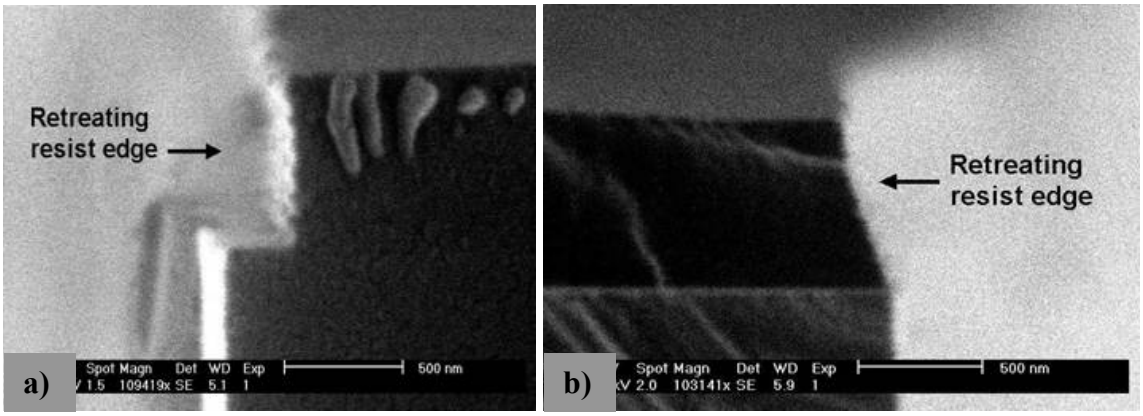

Figure 4.16: Cross section developing of flood exposed photoresist films reveals a) the uniform power distribution throughout an optically saturated film and b) the energy gradient that exists within a film when a much lower dose is used, revealed by the presence of a slope.

A technique that was used to precisely gauge the optimum developing time of every wafer is visible in Figure 4.7c. Here, one edge of the photoresist film was intentionally left outside of the patterned region of the mask, so that it received an unimpeded flood exposure. During developing, this flood exposed region was used to monitor the progress of developing, wherein its complete dissolution was taken to indicate that pattern developing was complete. The sidewalls of the optimally developed corrugated template in Figure 4.15 are a near vertical 8^{o} near the top of the photoresist, and increase to roughly 30^{o} at the substrate.

Extending developing time will produce an undercut sidewall, as shown in Figure 4.17a. This undercutting happens when developing a pattern because of the presence of a mask edge, which results in the lateral distribution of power due to diffraction. The extent to which the diffracted light is able to intrude beneath the opaque mask features is revealed by cross-sectioning the exposed photoresist pattern before briefly developing.

Figure. 4.17b shows a 3 μm wide line that has been developed in cross-section. It is clear that the standing wave pattern extends up to 400 nm beneath the mask edge.

Conversely, sidewalls have been encountered on occasion that were almost free of curvature, as shown in Figure 4.17c. It is assumed that this can be attributed to some precise developing time that is slightly short of the time that generates the curved sidewall. It should also be noted that it is not uncommon to have some subtle variety in the slope of the sidewalls, across any given wafer. This is likely due to a subtle combination of power variation across the wafer, as generated by the interference fringes between mask and photoresist, and fluid flow dynamics during developing.

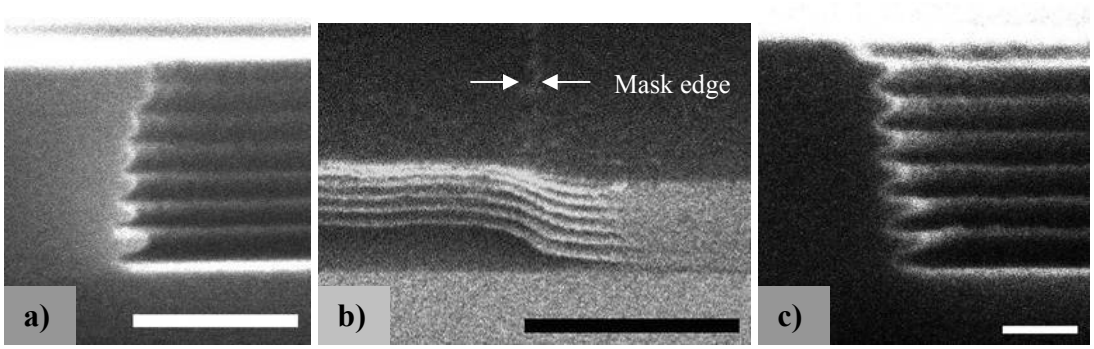

Figure 4.17: Cross section SEM images show that (a) an undercut profile results when the developing time is excessive (by 4 seconds in this case). (b) A cross-section develop reveals the presence of diffracted light below the mask edge. (c) Straight sidewall slopes are occasionally observed. Scale bars are 500 nm, 1 μm and 200 nm.

4.4.2 Depositing nanowires

These corrugated photoresist templates are used to form nanowires by coating them in a directional deposition system. Both a custom built thermal evaporator and a Balzers electron-beam evaporation system have been successfully applied to perform these depositions, with the latter producing predictably smoother and more uniform results.

Alignment of the substrate normal to the direction of the evaporated flux is important to avoid the photoresist bulk overshadowing the steep sidewalls. Depositing material creates nanometer wide deposits on the sidewall corrugations, as illustrated in Figure 4.14c, along with incidental deposits on all photoresist ceilings and exposed regions of substrate. Nanometer wide deposits are possible because of the small 100 nm vertical period of the corrugations, as well as the gentle positive slope of the photoresist

sidewalls. This offsets the corrugations relative to one another by tens of nanometers, allowing each of them to intercept the incident flux.

Figure 4.18 shows the stacked rings of nanowire that were created by evaporating 20 nm of gold at normal incidence onto the hole patterns. The widths of these wires can be seen more precisely in Figure 4.19, and range from approximately 17 nm on the steeper sections of sidewall, through intermediate widths of 22 nm, 34 nm and 37 nm, to 63 nm on the broadest bottom corrugation. These width measurements were made using the measurement function in the FEI Nova Nanosem electron microscope that was used for imaging these deposits. The straight-line ribbons in Figure 4.20a, created with a thicker film of 90 nm and imaged with a Phillips XL30 SEM, exhibit similar widths. Notice that depositing thicker layers reduces the gaps between wires.

Nanowires of gold, silicon dioxide, titanium and platinum have been successfully created, although many other materials are also expected to work. Multilayer combinations also show promise, as shown in Figure 4.20c and 4.20d. The former were composed of 10 nm layers of gold, silicon dioxide and gold, while the latter were composed of thicker layers of the same materials. Adhesion problems between the gold and silicon dioxide, which were evident in regions of both planar and nanowire deposits, made the multilayer deposits inferior to single material deposits.

After deposition, the wires are readily released from the template by dissolving the photoresist as shown in Figure 4.21. However these released wires would typically adhere to the substrate, perhaps as a result of van der Waals forces or perhaps due to photoresist residue.

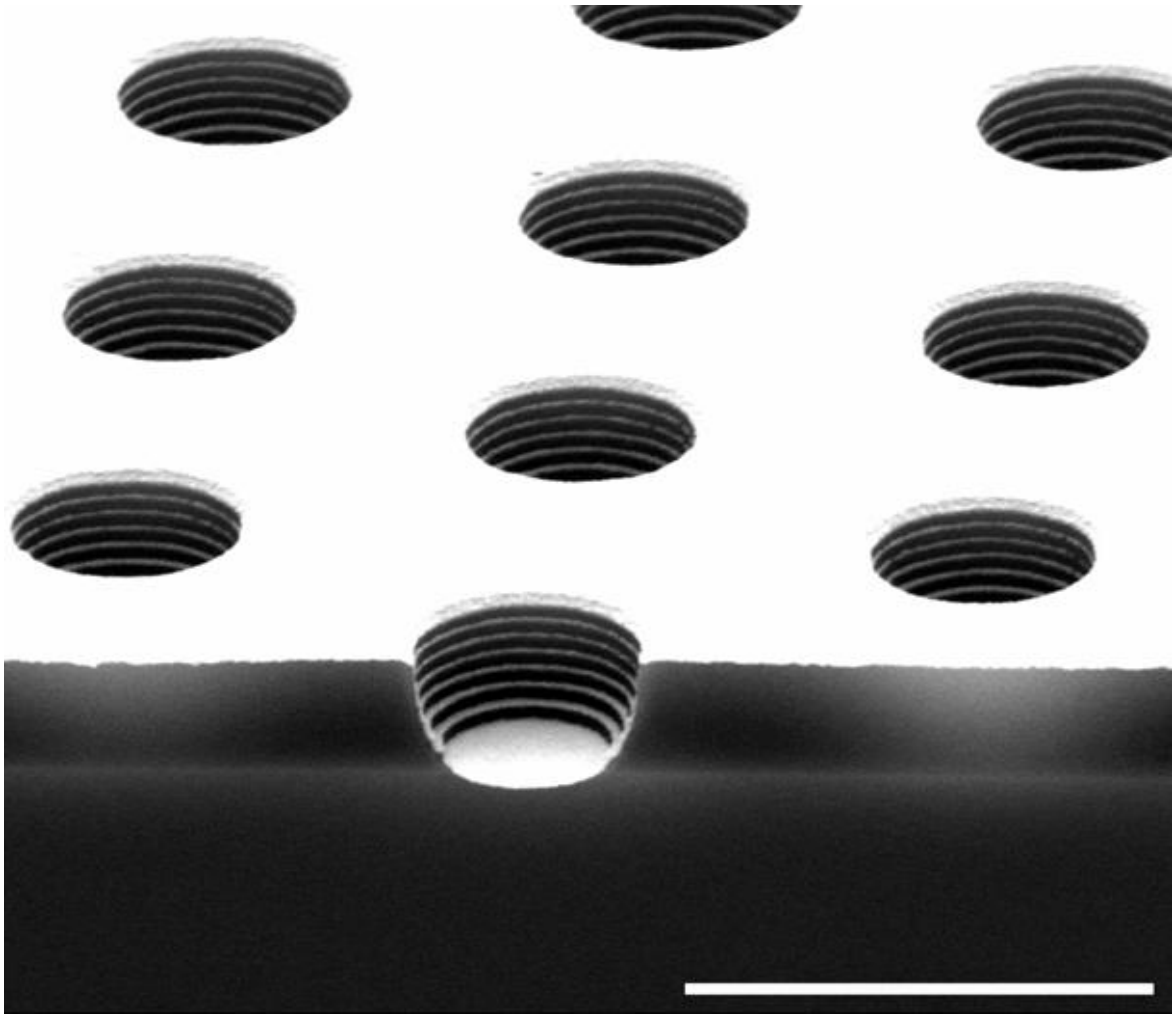

Figure 4.18: Broad view SEM image showing the distribution of the stacked rings across the substrate. These were formed by electron-beam evaporating 20 nm of gold onto a corrugated hole template. Scale bar is 3 μm.

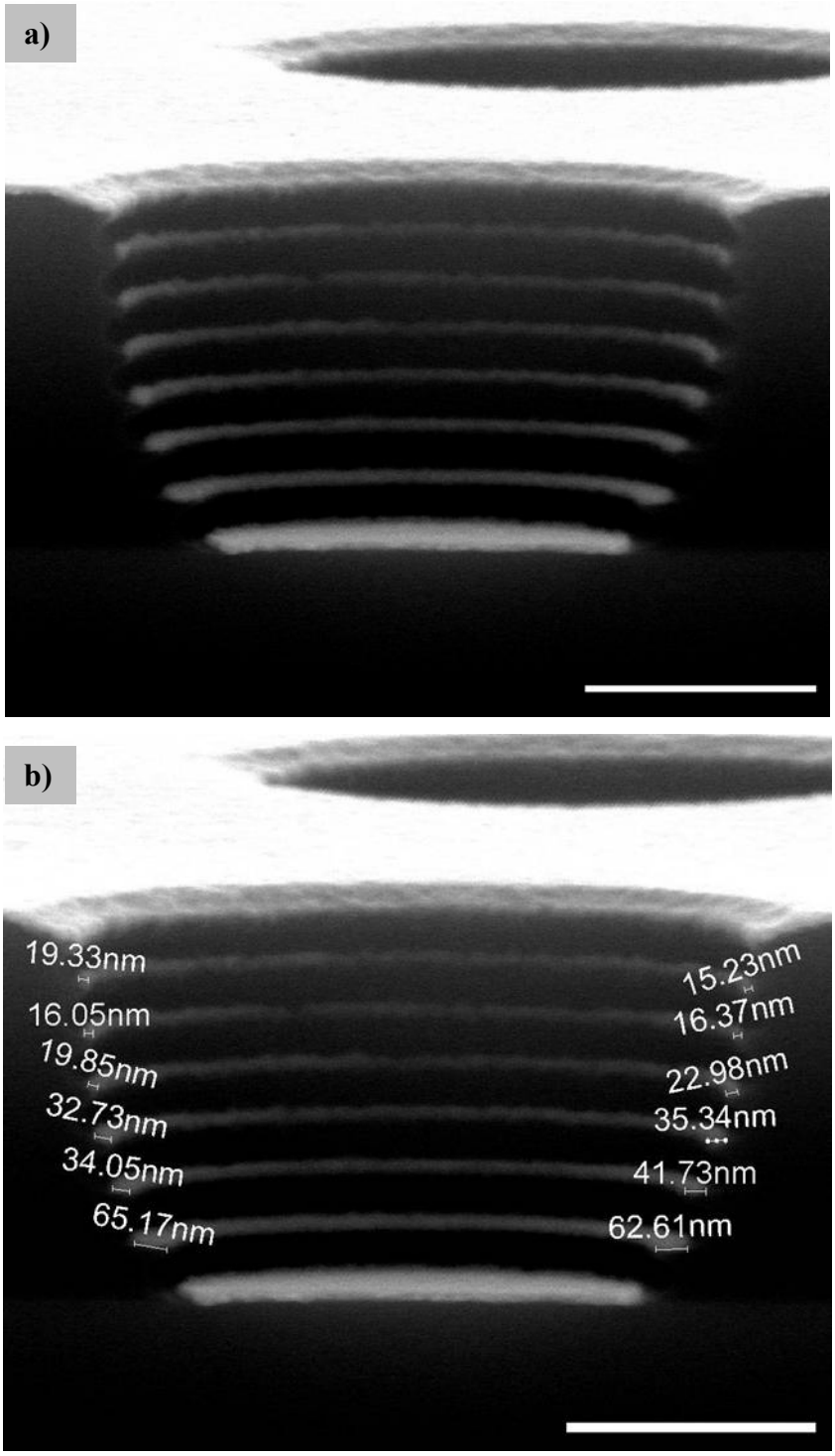

Figure 4.19: Cross section SEM images through stacked nanowire rings, formed by electron-beam evaporating 20 nm of gold at normal incidence. The change in width as a function of distance from substrate is illustrated. The same wires are shown twice, a) without and b) with width measurements. Scale bars are 500 nm.

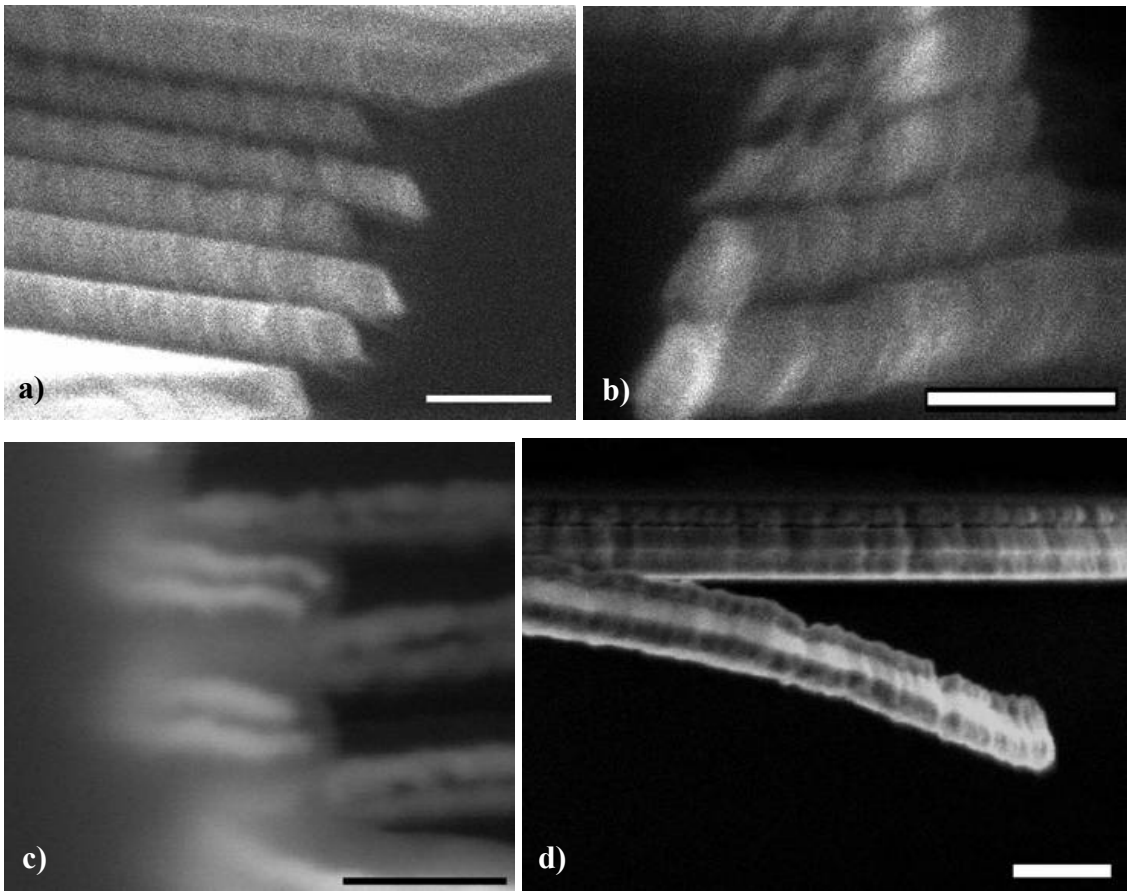

Figure 4.20: An SEM image shows a cross-section through straight lengths of high aspect-ratio gold nano-ribbons on a photoresist template, created by electron-beam evaporating (a) 90 nm of gold and (b) slightly more onto an arbitrary photoresist shape. A cross-section through (c) rings of multilayer nanowires, formed by electron-beam evaporation. These are composed of 10 nm layers of Au, SiO_2 and Au, while (d) shows a free-hanging multilayer nanoribbon, composed of thicker layers of the same materials. Scale bars are 200 nm, 200 nm, 100 nm and 200 nm.

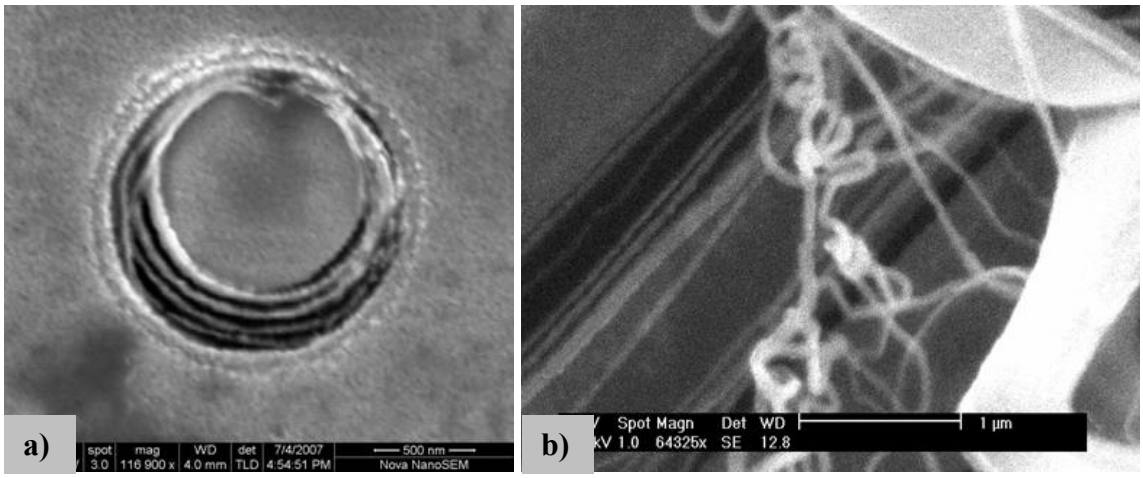

Figure 4.21: Gold nanowires that have been released from their photoresist templates. Rings (a) and straight lengths (b) are shown, some of which have become entangled. Some photoresist residue remains.

4.4.3 Number of corrugations on a sidewall

Adjusting the photoresist film thickness is a simple approach to changing the number of corrugations on a sidewall, as was clearly demonstrated in Section 4.3. However optical attenuation, diffraction and imperfect reflection from the substrate restrict the maximum number of useable corrugations. The intensities of the two interfering waves are best matched close to the substrate, which is where the deepest corrugations are found. In this demonstration, seven corrugations were reliably achievable with sufficient depth for masking, as shown in Figures 4.15 and 4.19.

4.4.4 Photoresist roughness

Discontinuities in the narrowest of wires were observed to occur on occasion. Needless to say, improper alignment relative to the evaporation source, or overdeveloping of the photoresist pattern so that the walls are undercut, will each prevent the deposition of nanowires on the sidewalls. However baring these two situations, discontinuities still occur on occasion. The dominant cause has been identified as the roughness of the photoresist, which creates width variations that can be consistently related to the wires immediately above and below any given wire, as shown in Figure 4.22. Experiments

employing a slight tilt and rotation during deposition have proven effective at combating discontinuities. Of the results presented in this chapter, only the 3x10 nm multilayer wires in Figure 4.20c were fabricated using tilt and rotation. As a general solution, it is expected that using an ultrahigh resolution photoresist would be ideal.

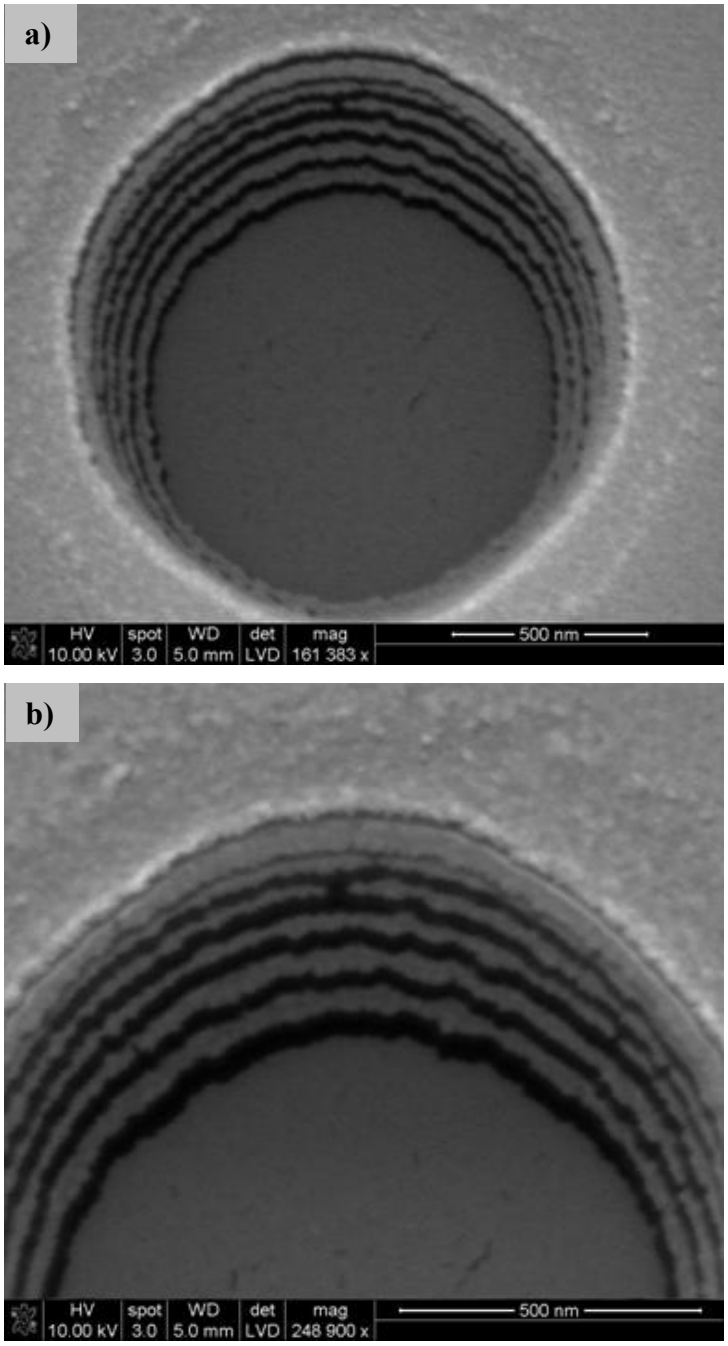

Figure 4.22: These platinum rings of nanowire demonstrate the width variation imposed by the photoresist template. Notice that these variations translate from one ring to the next, at times culminating in a discontinuity.

4.4.5 Optical diffraction and minimum line-widths

The minimum linewidth demonstrable by contact photolithography when using saturating exposure doses of the wavelengths displayed in Figure 4.5 is illustrated quite dramatically in Figure 4.23a. Here, a distribution of artifacts can be seen in between the intended hole patterns, which become less prevalent and then completely disappear as the hole separation is increased to approximately 2 μm, shown in Figure 4.23b. Although these artifacts seem to be localized to the photoresist ceiling, a closer inspection has revealed that they also impact the slope of the sidewall corrugations, reducing their usefulness as nanowire templates.

It was demonstrated in Figure 4.17b that the standing wave interference pattern can extend almost 0.5 μm beneath the mask edge. This is once again demonstrated in Figure 4.24a for the case of a very broad line of photoresist. If this linewidth is reduced in order to bring the mask edges closer together, as shown in Figure 4.24b, the photoresist directly beneath the center of the mask is exposed. It is presumed that this power distribution is the result of interference between the two regions of diffracted light. Presumably it is this lateral interference that is responsible for the artifacts evident in Figure 4.23a.

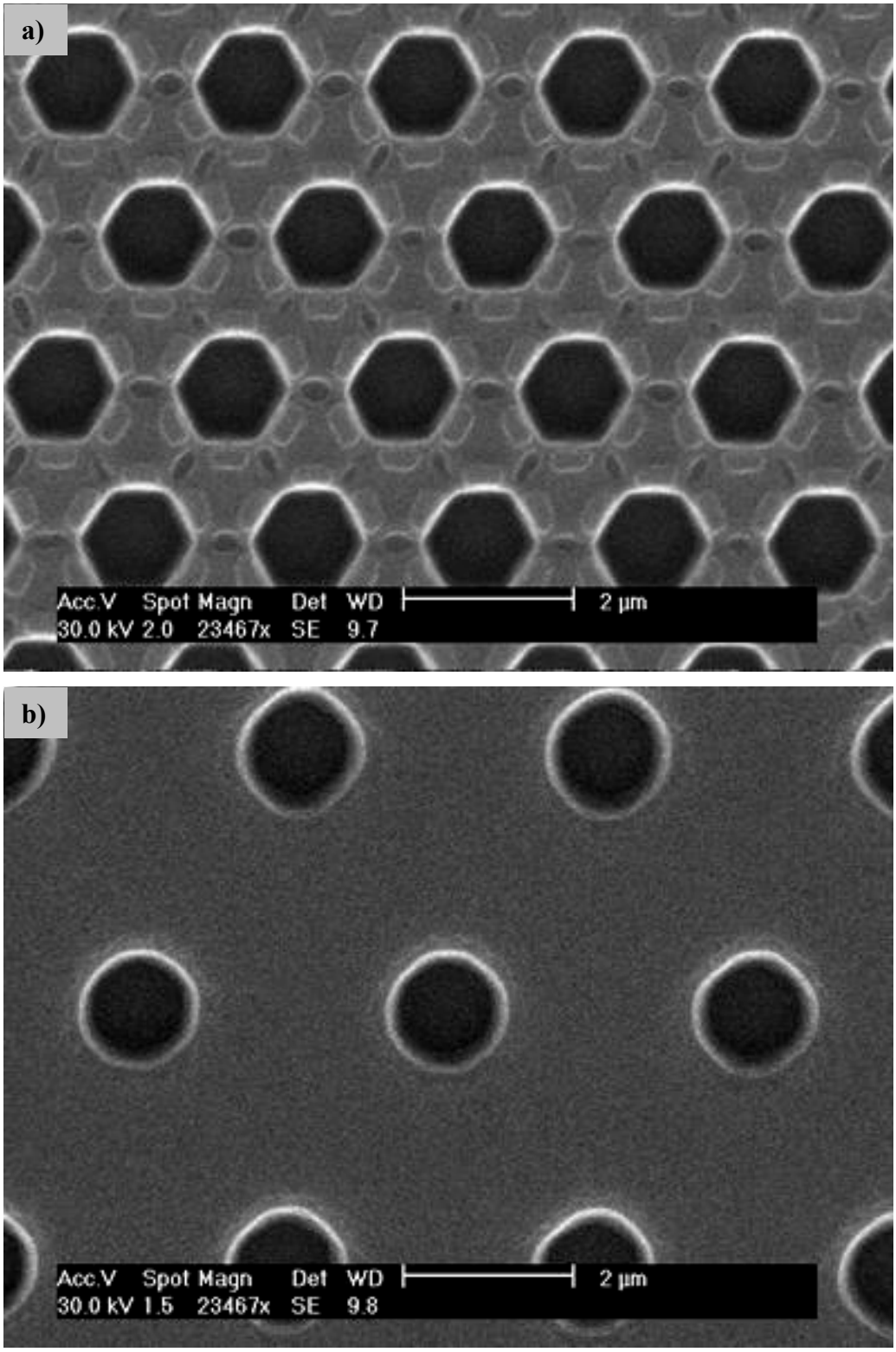

Figure 4.23: Undesirable artifacts appear in closely spaced pattern features (a), and are absent when features are more broadly spaced (b).

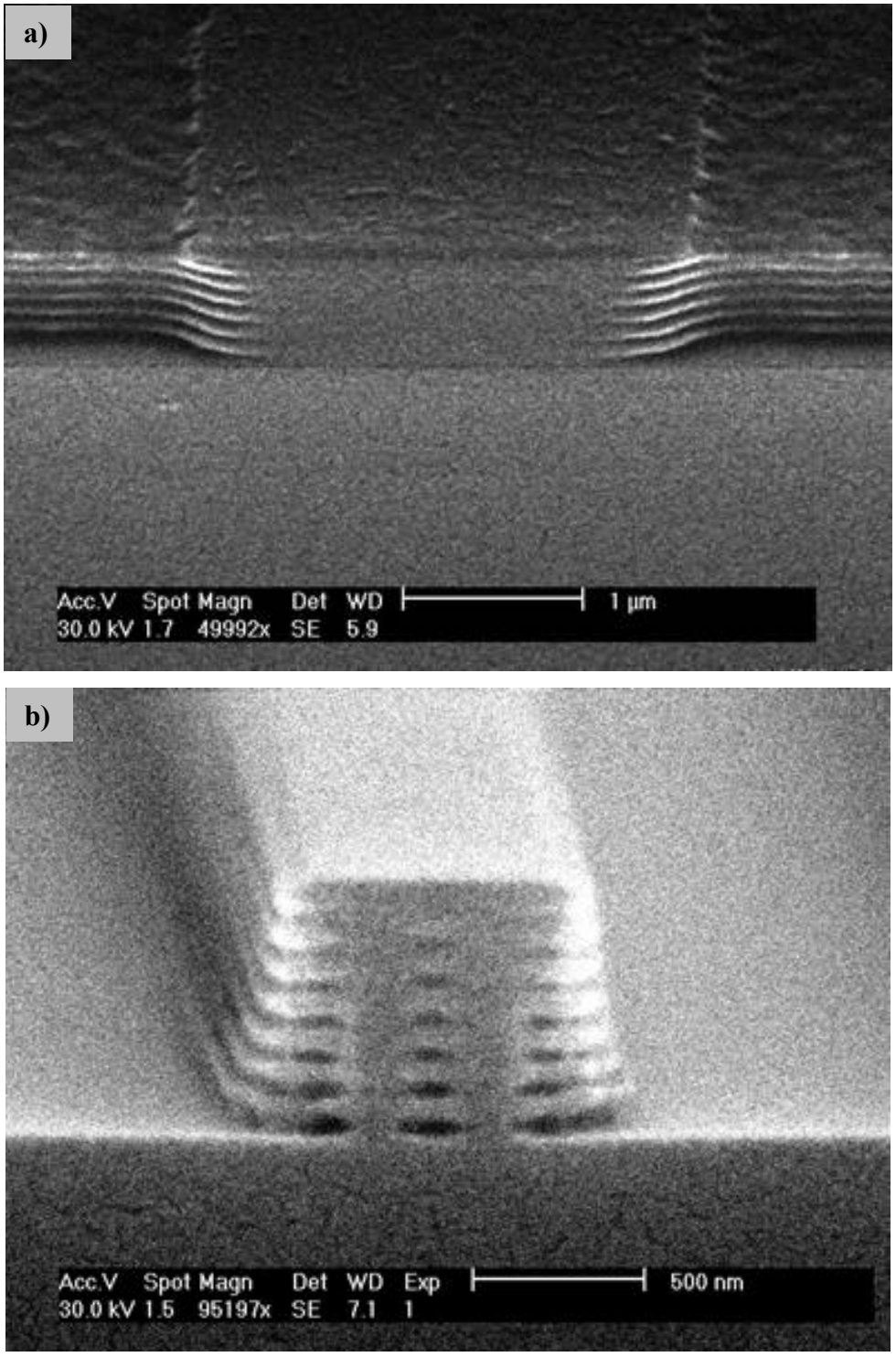

Figure 4.24: Cross-sectioning the exposed photoresist before partial developing reveals (a) the power distribution beneath the opaque mask regions. These can (b) interfere with one another when the linewidth is narrow enough.

4.5 Future work

Further improvements to these vertically stacked nanowire results, such as loop diameter reduction and a reduction in the periodicity of the corrugations, could be realized by employing a higher resolution photolithography technique such as deep UV or projection lithography. A more reflective substrate, and a narrower spectrum illumination source may also warrant investigation.

A potential application for these structures is as an ordered bulk optical material of subwavelength plasmonic resonators. This is an attractive proposition, in part because the circumference of these nanowire loops and thus their resonant frequency, could be precisely tuned by varying feature dimensions on the mask. Similarly, the shapes of the loops could be changed arbitrarily to form, for example, triangular or square loops of nanowire. In a similar vein, these nanowires could potentially be used as plasmonic waveguides.

Additionally, it is conceivable that a spiral photoresist template with micron line-width, could be used to very simply demonstrate nanowires that have lengths on the order of tens of kilometers. These great lengths would be confined to within a few square centimeters of substrate surface area.

Finally, in deference to the PDMS scattering mask demonstration, these corrugated nanowire templates could be transferred to a transparent bulk elastomer. This cast could then be used to replicate the corrugations into another material, or it could support the nanowire features itself, to demonstrate a transparent, flexible, nanowire template.

4.6 Conclusions

In closing, this chapter has demonstrated two novel nanofabrication techniques by utilizing micron sized photoresist templates that are patterned by standard photolithographic equipment. Both techniques derive their nanofeatures from sidewall standing wave corrugations and thus demonstrate applications for an artifact of photolithography that would otherwise require additional steps to eliminate it.

The first technique demonstrates a novel implementation of elastomeric edge-photolithography mask that is capable of patterning ~80 nm features in photoresist. Immediate applications include period halving of periodic structures and realizing either very narrow or very close proximity structures. Simple variations in photolithographic procedure, such as using negative photoresist, or the execution of consecutive orthogonal exposures, could be used to demonstrate both trench and post features in photoresist respectively. In a broader context, the scattering mask has again demonstrated that the technique of PDMS casting is well suited to undercut structures. These are structures that are intrinsically impossible to replicate with techniques that use rigid mold materials.

The second technique has demonstrated an extremely versatile bulk technique for three dimensional nanofabrication. The cross-sections of the demonstrated wires rival the capabilities of state of the art fabrication schemes, while their precise distribution in three dimensions is almost unchallenged. Furthermore, the ability of photolithography to define arbitrary photoresist patterns translates to an ability to fabricate closed nanowire loops of arbitrary delineation, while the range of materials that can be deposited by evaporation means that this technique can fabricate nanowires of almost any material.

Both of these techniques can claim the simplicity, reliability and parallel fabrication capabilities of contact photolithography while far exceeding its resolution capabilities. The latter technique in particular, surpasses the resolution limits of contact photolithography by a factor of roughly 50. Whatsmore, the global ubiquity of photolithographic equipment makes both of these techniques accessible to all photolithographers, everywhere.

A fitting collective term that describes both of these techniques is Sidewall Corrugation Lithography.

4.7 References

1. The international technology roadmap for semiconductors. (www.itrs.net)
2. C. Vieu, F. Carcenac, A. Pepin, Y. Chen, M. Mejias, A. Lebib, L. Manin-Ferlazzo, L. Couraud, H. Launois, *Electron beam lithography: Resolution limits and applications*, Applied Surface Science, 164, p. 111, 2000.
3. S. Matsui, T. Kaito, J. Fujita, M./ Komuro, K. Kanda, Y. Haruyama, *Three-dimensional nanostructure fabrication by focused-ion-beam chemical vapor deposition*, J. Vacc. Sci. Tech. B: Microelectronics and nanometer structures, 18(6), p. 3181, 2000.
4. Z. W. Pan, Z. R. Dai, Z. L. Wang, *Nanobelts of semiconducting oxides*, Science, 291, p. 1947, 2001.
5. X. Y. Kong, Y. Ding, R. Yang, Z. L. Wang, *Single-crystal nanorings formed by epitaxial self-coiling of polar Nanobelts*, Science, 303, p. 1348, 2004.
6. M. E. Stewart, M. J. Motala, J. Yao, L. B. Thompson, R. G. Nuzzo, *Unconventional methods for forming nanopatterns,* Proc. IMechE, Part N: J. Nanoengineering and Nanosystems, 220, p. 81, 2007.
7. B. D. Gates, Q. Xu, J. C. Love, D. B. Wolfe, G. M. Whitesides, *Unconventional nanofabrication,* Annu. Rev. Mater. Res., 34, p. 339, 2004
8. Y. Xia, J. A. Rogers, K. A. Paul, G. M. Whitesides, *Unconventional methods for fabricating and patterning nanostructures*, Chemical Review, 99, p. 1823, 1999.
9. H. Schmid, H. Biebuyck, B. Michel, *Light-coupling masks for lensless, sub-wavelength optical lithography*, App. Phys. Lett., 72(19), p. 2379, 1998.
10. O. J. F. Martin, N. B. Piller, H. Schmid, H. Biebuyck, B. Michel, *Energy flow in light-coupling masks for lensless optical lithography*, Optics Express, 3(7), p. 280, 1998.
11. D. Qin, Y. Xia, A. J. Black, G. M. Whitesides, *Photolithography with transparent reflective photomasks*, J. Vac. Sci. Technol. B, 16(1), p. 98, 1998.

12. J. A. Rogers, K. E. Paul, R. J. Jackman, G. M. Whitesides, *Using an elastomeric phase mask for sub-100nm photolithography in the optical near field,* App. Phys. Lett., 70(20), p. 2658, 1997.
13. J. A. Rogers, K. E. Paul, R. J. Jackman, G. M. Whitesides, *Generating ~90 nanometer features using near-field contact-mode photolithography with an elastomeric phase mask*, J. Vac. Sci. Technol. B, 16(1), p. 59, 1998.
14. J. Maria, S. Jeon, J. A. Rogers, *Nanopatterning with conformable phase masks*, Journal of Photochemistry and Photobiology A: Chemistry, 166, p. 149, 2004.
15. T. W. Odom, V. R. Thalladi, J. C. Love, G. M. Whitesides, *Generation of 30-50 nm structures using easily fabricated composite PDMS masks*, J. Am. Chem. Soc., 124, p. 12112, 2002.
16. T. W. Odom, J. C. Love, D. B. Wolfe, K. E. Paul, G. M. Whitesides, *Improved pattern transfer in soft lithography using composite stamps*, Langmuir, 18, p. 5314, 2002.
17. T. Hesjedal, W. Seidel, *Near-field elastomeric mask photolithography fabrication of high-frequency surface acoustic wave transducers*, Nanotechnology, 14, p. 91, 2003.
18. T. Lee, S. Jeon, J. Maria, J. Zaumseil, J. W. P. Hsu, J. A. Rogers, *Soft-contact optical lithography using transparent elastomeric stamps: application to nanopatterned organic light-emitting devices*, Advanced Functional Materials, 15, p. 1435, 2005.
19. X. Zhang, E. M. Hicks, J. Zhao, G. C. Schatz and R. P. Van Duyne, *Electrochemical tuning of silver nanoparticles fabricated by nanosphere lithography*, Nano Letters 5(7), p. 1503, 2005.
20. S. B. Chaney, S. Shanmukh, R. A. Dluhy and Y. –P. Zhao, *Aligned silver nanorod arrays produce high sensitivity surface-enhanced Raman spectroscopy substrates*, App. Phys. Lett., 87, 031908, 2005.
21. J.-Q. Xi, J.K. Kim, E. F. Schubert, *Silica nanorod-array films with very low refractive indices*, Nano Letters, 5(7), p. 1385, 2005.

22. J.-Q. Xi, Martin F. Schubert, J.K. Kim, E. F. Schubert, M. Chen, S.-Y. Lin, W. Liu & J. A. Smart, *Optical thin-film materials with low refractive index for broadband elimination of Fresnel reflection*, Nature Photonics, 1, p. 176, 2007.
23. B. D. Gates, Q. Xu, V. R. Thalladi, T. Cao, T. Knickerbocker, and G. M. Whitesides, *Shear patterning of microdominos: A new class of procedures for making micro- and nanostructures*, Angew. Chem. Int. Ed, 43, p. 2780, 2004.
24. N. A. Melosh, A. Boukai, F. Diana, B. Gerardot, A. Badolato, P. M. Petroff, J. R. Heath, *Ultrahigh-density nanowire lattices and circuits*, Science, 300, p. 112, 2003.
25. R. A. Beckman, E. Johnston-Halperin, N. A. Melosh, Y. Luo, J. E. Green, J. R. Heath, *Fabrication of conducting Si nanowire arrays*, Journal of Applied Physics, 96(10), p. 5291, 2004.
26. M. C. McAlpine, H. Ahmad, D. Wang, J. R. Heath, *Highly ordered nanowire arrays on plastic substrates for ultrasensitive flexible chemical sensors*, Nature Materials, 6, p. 379, 2007.
27. D. Wang, B. A. Sheriff, J. R. Heath, *Silicon p-FETs from ultrahigh density nanowire arrays*, Nano Letters, 6(6), p. 1096, 2006.
28. V. Milanovic, L. Doherty, D. A. Teasdale, S. Parsa and K. S. J. Pister, Micromachining technology for lateral field emission devices, IEEE Trans. Elect. Dev., 48(1), p. 166, 2001.
29. H. C. Ko, A. J. Baca, J. A. Rogers, Bulk quantities of single-crystal silicon micro-/nanoribbons generated from bulk wafers, Nano Letters, 6(10), p. 2318, 2006.
30. C. A. Mack, *Analytical expression for the standing wave intensity in photoresist*, Applied optics 25(12), p. 1958, 1986.
31. C. A. Mack, *Lithography on reflective substrates*, Microlithography World, 6(2), p. 21, 1997.
32. C. A. Mack, *Designing a bottom antireflection coating*, Microlithography World, pp.12, Feb 2003.
33. C. A. Mack, *Bottom antireflection coatings for high numerical aperture imaging*, Microlithography World, p. 12, May 2005.

34. E. J. Walker, *Reduction of photoresist standing-wave effects by post-exposure bake*, IEEE Transactions on electron devices, 22(7), p. 464, 1975.
35. A. G. Grandpierre, R. Schiwon, F. Finger, *Standing wave reduction of positive and negative I-line resists*, Proc. Of SPIE, Bellingham, WA, 5752, p. 755, 2005.
36. N.Bogdanski, H.Schutz, M.Wissen, H.Scheer, J.Zajadacz, K.Zimmer, *3D-Hot embossing of undercut structures: an approach to micro-zippers*, Microelectronic Engineering, 73-74(1), p. 190, 2004.
37. A. L. Martin, D. K. Armani, L. Yang, K. J. Vahala, *Replica-molded high-Q polymer microresonators*, Optics letters, 29(6), p. 533, 2004.
38. S. Chang, J, Yoon, *Shape-controlled, high fill-factor microlens arrays fabricated by a 3D diffuser lithography and plastic replication method*, Optics Express, 12(25), p. 6366, 2004.
39. C. N. LaFratta, T. Baldacchini, R. A. Farrer, J. T. Fourkas, M. C. Teich, B. E. A. Saleh, M. J. Naughton, *Replication of two-photon polymerized structures with extremely high aspect ratios and large overhangs*, J. Phys. Chem. B, 108, p. 12256, 2004.
40. E. Menard, L. Bilhaut, JJ. Zaumseil, J. A. Rogers, *Improved surface chemistries, thin film deposition techniques, and stamp designs for nanotransfer printing*, Langmuir, 20, p. 6871, 2004.
41. W. Jiang, N. Zhitenev, Z. Bao, H. Meng, D. Abusch-Magder, D. Tennant, E. Garfunkel, *Structure and bonding issues at the interface between gold and self-assembled conjugated dithiol monolayers,* Langmuir, 21, p. 8751, 2005.
42. M. R. Dusseiller, D. Schlaepfer, M. Koch, R. Kroschewski, M. Textor, *An inverted microcontact printing method on topographically structured polystyrene chips for arrayed micro-3-D culturing of single cells*, Biomaterials, 26, p. 5917, 2005.
43. A. K. Bates, M. Rothschild, T. M. Bloomstein, T. H. Fedynyshyn, R. R. Kunz, V. Liberman, M. Switkes, *Review of technology for 157-nm lithography*, IBM J. Res. and Dev., 45, p. 605, 2001.

Chapter 5.

Nanoarray Biotemplating: Optical Fiber Imprinting for Surface-Enhanced Raman Scattering

5.1 Introduction

In Chapter 3, micron scale planar waveguides were fabricated and characterized. In Chapter 4, two novel nanofabrication techniques were demonstrated by following the spartan philosophy of identifying and exploiting existing nanoscale phenomena.

In this chapter, the waveguiding, replication and nanofabrication principles demonstrated in the preceding chapters are combined to demonstrate a novel, optically interrogated, nanostructured chemical sensor. For the first time, nanoimprint lithography is used to pattern the end face of an optical fiber. A nanostructured biological template is used for replication, to which a sensing capability is added by line of sight coating with metal. Surface-enhanced Raman scattering (SERS) measurements are made in both direct and through-fiber interrogation modes to demonstrate the ultra-high sensitivity of this device.

This chapter begins with a brief overview of plasmons, Raman scattering, SERS and SERS sensing platforms.

5.1.1 Surface plasmons

The interaction of light with metal/dielectric interfaces is of central importance to this chapter; in particular, the nature and exploitation of surface plasmon resonances. While surface plasmons exist at planar boundaries, their utility is greatly increased when they are confined or localized to a nanoscale volume. This localization has the effect of enhancing optical near fields, which has given rise to several new fields of research [1,2], including subwavelength optics [3,4], near field subwavelength patterning [4] and ultra-sensitive detection techniques [6].

Surface plasmons, also known as surface plasmon polaritons, are established when an electromagnetic field is incident on a metal/dielectric interface. The incident field acts to establish a tightly bound evanescent field at the boundary which maintains continuity between the electric and magnetic fields across this interface, thus coupling the incident field to the sea of free conduction electrons in the metal. The result is that the incident field induces charge density oscillations within the conduction electrons, which are known as surface plasmons [7].

Surface plasmons are characterized by their exponential decay with distance into both media at a metal / dielectric interface. Into the dielectric, this decay length defines the boundary of the optical near field, while into the metal, this length can be as small as 10 nm and is known as the material skin depth. In the case of a smooth planar boundary, the plasmons will propagate along the plane of the interface as damped oscillatory waves, leading to the dissipation of the plasmon energy, which manifests as resistive heating of the metal [8]. The damping mechanism responsible for this dissipation is the material loss, as described by the imaginary component of its dielectric function. Thus a smaller loss component corresponds to a more intense and sustainable plasmon excitation. In the UV-visible spectrum, the metal with the smallest loss component is silver, followed by gold. [9]

The significance of nanoscale dimensions to surface plasmons is their equivalence to material skin depth and their subwavelength scale compared to the incident illumination. These two parameters combine to increase the coherence of the confined oscillating free electrons to the point that they are all moving in phase, allowing for the

buildup of polarization charges on the surface of the nanostructure [10]. The degree of coherence is proportional to the structure size, such that a sufficiently small structure will result in a dipolar distribution of polarization charges, while less ideal larger structures will produce higher order multipole distributions. If the illuminating wavelength is carefully matched to the nanostructure shape, dimension, distribution, material and the dielectric index of the surrounding medium, a resonance of the free electrons inside the nanostructure occurs, wherein the surface polarization charges act as a restoring force [10]. This wavelength is known as the particle dipole plasmon frequency and the associated resonance establishes a large enhancement of the optical near field intensity at the laser wavelength [2]. This enhanced field extends 10-50 nm from the metal surface into the dielectric [11].

Note that these nanoscale structures do not need to be discrete particles. Nanoscale features on a continuous film, such as sharp points and edges, exhibit similar behavior. Recent advancements in nanofabrication techniques have increased the accessibility of these subwavelength structures for the visible spectrum, driving the development of many new technologies.

5.1.2 Raman scattering

Raman spectroscopy is a widely used materials analysis technique that is commonly applied to identifying bulk chemical and biological analytes. The uniquely identifying spectral information is derived from inelastically scattered Raman light.

Although the scattering of light by molecules is typically elastic, a small percentage of interactions are inelastic and result in a change of the rotational or vibrational energy of the scattering molecule. Changes in vibrational energy occur when an electron is excited to a virtual state by the absorption of a photon, after which it returns to an energy level that differs from its origin. The difference in energy between the emitted and exciting light is characteristic of the scattering molecule, and the emitted photon is said to have been Raman scattered. The energy transfer can either be an absorption or a donation by the molecule, wherein the two events are known as Stokes and anti-Stokes scattering respectively [12].

The derivation of Raman spectroscopy from this interaction relies on the use of a monochromatic illumination source as the exciting light, such that a spectral analysis of the scattered light reveals the induced Raman shifts. The Stokes and anti-Stokes scattered lines in a Raman spectrum are symmetrically distributed about the elastically scattered laser line.

Unfortunately, despite Raman spectroscopy's ability to provide vibrational fingerprints of materials, the Raman cross-section of most molecules is quite low, and can be attributed to less than one in one million photons. This restricts the application of Raman spectroscopy to the analysis of bulk materials, and thus to the exclusion of low concentration analytes.

5.1.3 Surface-enhanced Raman scattering

Surface enhanced Raman scattering (SERS) is an ultra-sensitive implementation of Raman scattering that enhances its signal intensity by over a million times [13,14] and thus dramatically extends its utility. The enhancement is obtained when arrays of nanoscale localized plasmon resonators are used as substrates for performing Raman measurements. Analyte molecules that are either adsorbed to the surface of plasmon resonant nanostructures or are in their proximity, are subjected to the intense localized plasmon field, which increases the scattering cross section of the molecules and provides enhanced Raman spectra and thus increased sensitivity. The intensity and quality factor of the plasmon resonance and the magnitude of the SERS enhancement have been shown to be in very close qualitative agreement, and the relationship between the two is commonly described as the electromagnetic mechanism of SERS. Any part of the surface enhancement that is not accounted for by the electromagnetic mechanism is typically attributed to the chemical mechanism [15], which will not be discussed here. Within the visible spectrum, nanostructures of Ag and Au are recognized as providing the most intense SERS signals.

The pioneering work in this field was performed by Fleischmann [16], Van Duyne [17,18] and Albrecht and Creighton [19] in the 1970s. Original observations attributed the enhancements to increased surface areas. However in the years that followed, it was demonstrated that this did not sufficiently account for the enhancement,

which lead to the proposal that a new type of Raman mechanism was at play. In the thirty years that followed, a more complete picture was developed.

It was in the late 1990s that interest in this field exploded due to reports that concentrations as low as a single molecule (SMSERS) could be successfully detected [20,21]. Single molecule detection implies an enhancement factor of $>10^{13}$, which has been attributed to randomly formed particle-junction structures on the SERS substrate acting as hotspots. Unfortunately, the performance of SMSERS has been intermittent at best, which has limited its widespread application.

However, even in lieu of single molecule detection, it is difficult to overstate the importance of SERS as a sensing platform and as an emerging application of nanotechnology. It has already been applied to fields as promising as continuous glucose monitoring [22], the identification of single microorganisms [23], cancer diagnostics [24], multiplexed detection of disease markers [25] and the ultra-sensitive determination of enzyme activities [26]. However, despite these numerous important applications, the technique remains largely limited to laboratory use. More widespread application requires the development of robust, repeatable, sensitive and low cost SERS probes. This chapter attempts to address this issue.

5.1.4 SERS sensors

The range of economical approaches to fabricating SERS surfaces has been surprisingly limited. Initial planar implementations relied on electrochemical roughening [27] and spontaneous clustering in thin films [28] as per Section 4.13, to produce nanoscale plasmonic resonators. However the drive to maximize SERS enhancements required that SERS surfaces be engineered with a higher degree of precision. To this end, thin metal films deposited over self assembled nanosphere monolayers have proven to be a robust and popular solution [11,29], illustrated in Figure 4.2. However even this technique relies to some degree on self-assembly, which limits its structural uniformity and long-range coherence and thus its amenability to design.

As a general progression towards widespread adoption, optical fiber endfaces represent a class of substrates that offer significant advantages over conventional planar implementations. The optical fiber itself, as a medium for interrogating its own SERS

active endface, eliminates the need for high-precision focusing optics and confines potentially dangerous free space propagating lasers, while illuminating the active surface with diffuse rather than focused light, which reduces the likelihood of thermal damage. The low-loss length of the fiber can also be exploited to conduct both remote and in situ sampling and process monitoring. Additionally, optical fiber probes are intrinsically compatible with modern, low-cost photonic waveguide technologies, such as laser diodes, Bragg grating filters and compact spectrometers.

As a consequence of these advantages, several architectures of single-fiber SERS sensors have been demonstrated in the literature. However, their implementation has been limited to the application of the existing planar techniques described above. End face roughening [30], thin film clustering [31] and colloidal nanoparticles [32-34] have all been implemented, as illustrated in Figure 5.1. However, these are all subject to the same limitations as the planar devices. A recent fiber SERS innovation has demonstrated greater control over the regularity of its nanostructure by selectively etching drawn imaging fibers [35], however this technique has not proven suitable for through-fiber sensing.

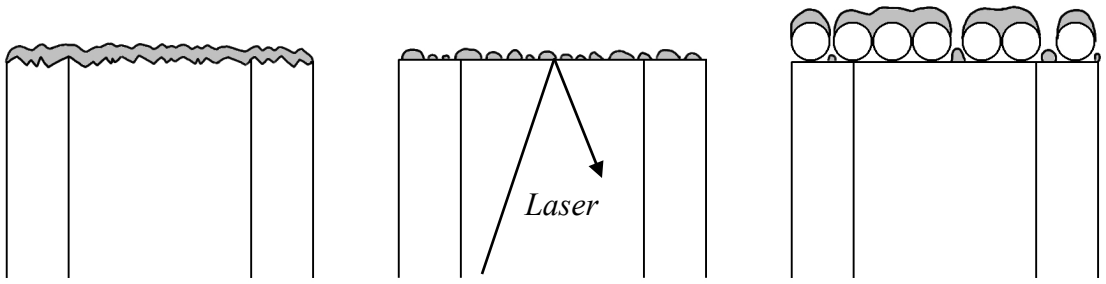

Figure 5.1: Existing implementations of fiber endface SERS probes. From left to right, mechanically roughened, thin film island formation, and thin film over nanosphere.

5.1.5 Polymer techniques for optical fiber endface patterning

In pursuing the development of a novel, low cost and robust fiber-based SERS sensor, and in keeping with the themes of this thesis, this chapter explores an alternative fabrication approach. This is the use of patterned polymers on the fiber endface.

In the optics community polymers have enjoyed considerable attention, primarily because they lend themselves readily to fabrication and property modification. Chapter 3

demonstrated this suitability with the fabrication of planar polymer waveguide devices. However, their use with fiber endfaces has been quite limited. Demonstrations have included the fabrication of lenses [36], the use of photoresists for interference lithography [37] and fiber core extensions by through-fiber illumination [38]. Polymer optical fibers have even had their endfaces depressed into lens shaped cavities [39] in a rudimentary demonstration of molding.

Notably the patterning of optical fiber endfaces by nanoimprint lithography (NIL) has not been demonstrated. A proposal to imprint onto an optical fiber endface is, for all practical purposes, a proposal to imprint onto a miniaturized substrate. To put this into perspective, note that advances in NIL have been focused primarily on patterning large planar and non-planar substrates [40,41]. This work has been driven largely by the popularity of NIL, which is derived from its versatility, high resolution, low cost, and conceptual simplicity [42]. This chapter brings NIL to an optical fiber platform.

5.2 A biological template for SERS

As was demonstrated in Chapter 3, the replication process begins with the creation of a master structure. However this is no simple task, particularly in the challenging nano-regime of SERS. It is thus serendipitous that an abundance of complex photonic structures can be found in the biological world [43]. While it has become fashionable to derive inspiration from biological structures [44], some biological structures are actually suitable for direct replication [45], while also having appropriate dimensions for SERS. These include the corneal nipple arrays of butterflies [46], the transparent wings of hawk moths [47] and the wings of some termites [48] and cicadas [49], all of which exhibit broadband antireflection properties based on planar arrays of subwavelength pillars. Stoddart et al. [49] recently demonstrated the SERS activity of the metal coated wings of the *Cicadetta celis*, paving the way for this demonstration.

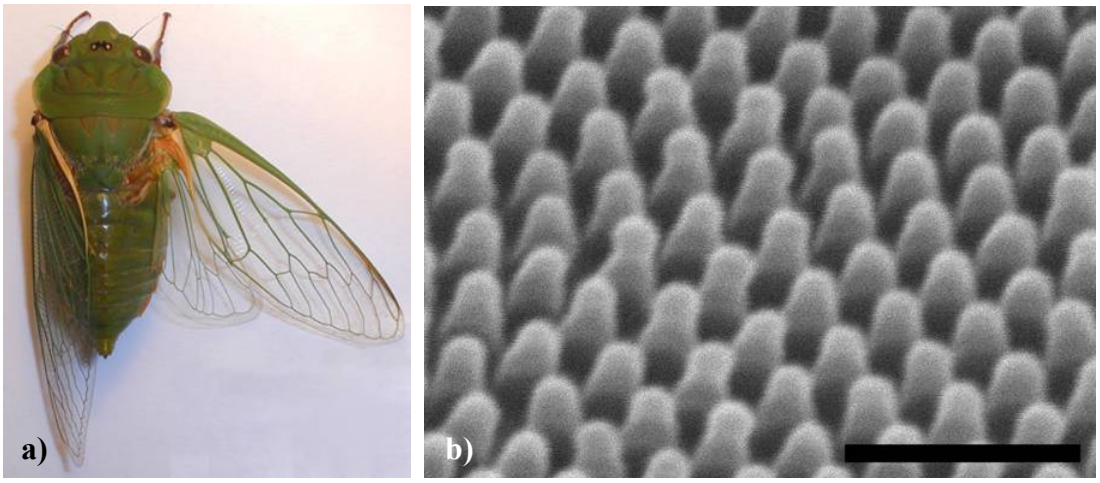

Figure 5.2: A photograph of (a) a greengrocer cicada shows its transparent wings. A high magnification SEM image (b) of these transparent regions shows that they are covered in a planar array of nanoscale antireflection features. Scale bar is 500 nm.

In this chapter, the wings of the greengrocer *Cyclochila australasiae* cicada are employed as nanostructured templates. The greengrocer is a plentiful species found along the south-east coast of Australia in the hot summer months. Their presence is advertised by their long pulsing song which can approach the pain threshold of the human ear [50]. Specimens were either captured locally or donated by the Australian Museum.

A greengrocer specimen is shown in Figure 5.2a, where its forewing of length of 55 mm, and its shorter hindwing, are clearly visible. The cicada also has a small false wing, known as the anal lobe attachment, beneath each hindwing, although its transparency limits visibility in this figure. Each wing in its entirety exhibits significant curvature which approximates the contours of the cicada body, while on the sub-millimeter scale the transparent sections display significant undulations. These transparent sections are quite flexible, dictating that the mechanical strength required for flight be contributed by rigid venation. This venation does not share the nanofeatures of the transparent chitin.

The antireflective nanostructure on the greengrocer cicada wing is shown in Figure 5.2b. It consists of a dense two dimensional array of pillars that have separations, diameters and heights of approximately 50 nm, 110 nm and 200 nm respectively,

however these dimensions vary across the wing surface. The distribution of these features is hexagonal within domains of approximately 1.5 μm.

In this work, these structures are transferred to a high resolution mold, as illustrated in Figure 5.3, which in turn is used to imprint polymer on the endfaces of optical fibers.

5.3 Deriving a mold from the cicada nanostructure

Features as small and dense as those on the cicada wing are commonly known as an acid test of any fabrication technique. Therefore, taking high fidelity casts requires the careful selection of an appropriate mold material. Although the direct casting of cicada wings was recently demonstrated by Zhang in PMMA [45], the transparency and low surface energy of the traditional soft-imprinting elastomers made them better suited to this application. Primary attempts at casting were made using the low modulus s-PDMS (Sylgard 184, Dow Corning), however high fidelity regions were sparse at best. At worst the molds were dominated by surface tension, which converted the pillars on the cicada wing into shallow dimples. As a result, the more rigid h-PDMS was used.

H-PDMS was formulated by Schmid and Michel as a higher resolution alternative to s-PDMS [51]. Its higher resolution is derived from the addition of vinyl and hydrosilane compounds which act to increase the Young's modulus of the elastomer. To date, the high resolution of h-PDMS has been demonstrated to improve the performance of elastomeric phase masks [52], contact printing, and replication [53] down to the molecular scale [54]. However despite its superior resolution, h-PDMS has not enjoyed the same widespread adoption as s-PDMS. This is primarily because its higher rigidity also makes it brittle and susceptible to fracture [51,54].

5.3.1 Fabricating the inverse cicada molds

The h-PDMS was prepared within a sealed glove box containing a nitrogen atmosphere. This was necessary as a precaution against the toxicity and susceptibility to moisture of some of its components.

The constituents of h-PDMS and their required quantities are specified in the literature [51,53], but they are reiterated here because of changes to product names.

Preparation began by decanting 3.4 g of vinyl PDMS prepolymer (VDT-731, Gelest Corp.), to which was added 18 µl of the catalyst platinum divinyltetra-methyldisiloxane (SIP6831.2LC, Gelest Corp.), 0.1 g of the modulator 2,4,6,8-tetramethyltetravinylcyclotetrasiloxane (87297, Sigma Aldrich) and 1 g of hydrosilane component (HMS-301, Gelest Corp.). This solution was mixed thoroughly, producing a low viscosity liquid.

The cicada wings were sectioned into 9 mm^2 segments before casting, as illustrated in Figure 5.3. This was made necessary by the large scale curvature of the wings. One side of these segments was drip coated with liquid h-PDMS solution and then degassed in vacuum for 10 minutes to promote filling of the nanostructure. These coated wing segments were then placed liquid side down onto a glass wafer which in turn was placed on a hotplate at 60 ^oC for more than 12h to cure the h-PDMS.

After curing, a scalpel blade was used to pry one edge of the flexible wing segment upwards, separating it from the glass backed h-PDMS. This separation process was conducted at the curing temperature in order to avoid differential thermal expansion and the associated potential for damaging the cast [51]. The wing offered very little resistance to separation, while the h-PDMS remained firmly bonded to the glass backing. This completed the fabrication of the high-resolution, low surface-energy, transparent, elastomeric mold, shown in Figure 5.4a.

The nanostructure on the mold surface is shown in Figure 5.4b, where it was sputter-coated with a thin film of gold before imaging. The pattern is clearly the inverse of the cicada pillar structure, such that it is composed of a dense array of holes. The high fidelity of this inverse replica can be qualitatively deduced from the high image contrast between the holes and rest of the h-PDMS.

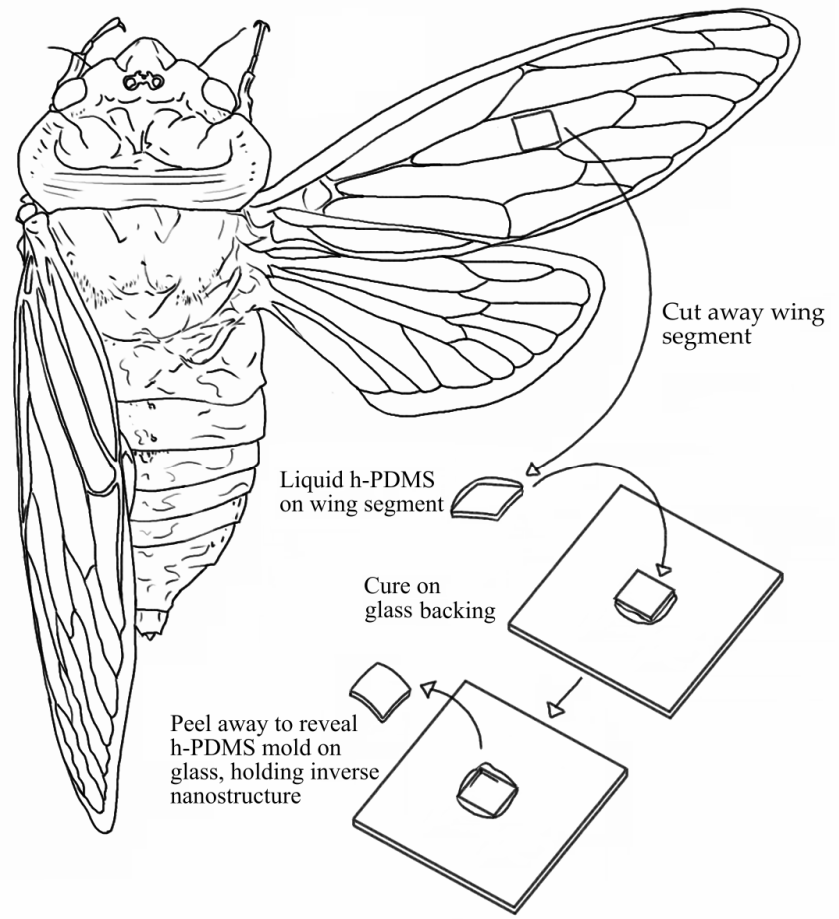

Figure 5.3: Deriving a mold from the cicada.

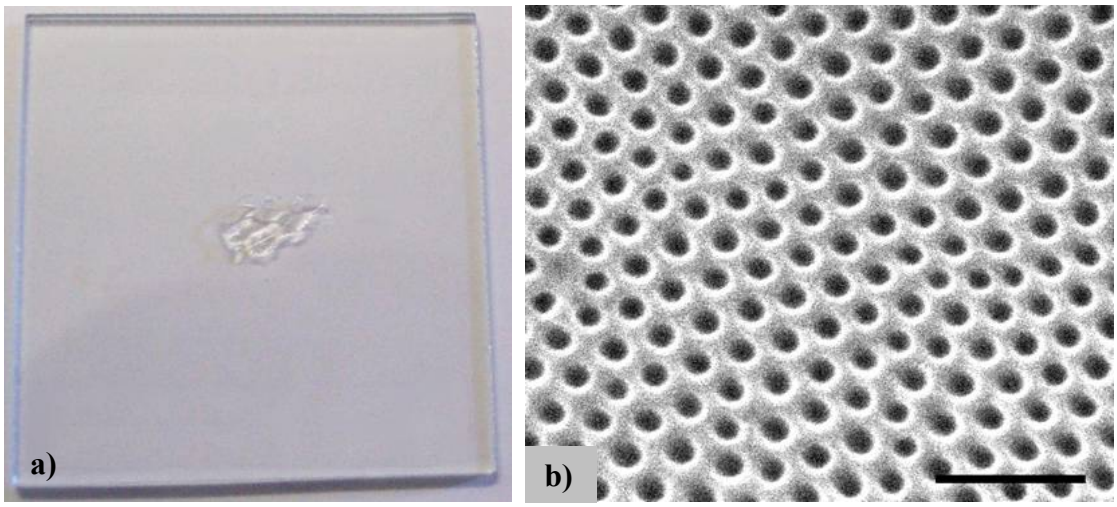

Figure 5.4: A photograph shows (a) the glass-backed h-PDMS mold. A high magnification SEM image of the h-PDMS shows (b) the inverse nanostructure that it holds. The glass slide has a 1" side length, and the scale bar is 500 nm.

5.4 Fabricating the fiber probes

The optical fiber used for imprinting was an arbitrarily selected 50/125 μm graded-index multimode fiber. Since the practical requirement from a fiber for imprinting is limited to the provision of a clean, smooth endface, its preparation was limited to the removal of its jacket, followed by cleaving into lengths of approximately 2 cm.

In Chapters 3 and 4, it was demonstrated that the conventional approach to performing imprinting is to manipulate the mold by hand. However, as stated in Section 5.1.5, the primary difference between traditional imprinting and fiber endface imprinting is one of reduced dimensions. This makes it difficult to judge the proximity of the small cross-section fiber to the mold. Additionally, large substrate imprinting typically provides an equivalent layer of liquid polymer on which the mold can float, whereas the volume of polymer on the fiber tip is minute and easily displaced. These factors are expected to make collisions between the mold and fiber difficult to avoid, and thus precludes the use hands.

As a consequence, imprinting was performed by mounting both the fiber and the mold into a device that offered suitable finesse in positioning. This took the form of a vibration isolated optical fiber alignment system (Newport Autoalign^{TM}). The elements of the autoaligner that were employed for imprinting were two x-y-z microtranslation stages, a digital camera with attached magnifying optics and a spot curing ultraviolet light source (Novacure 2100). A photograph of the AutoAlign system is shown in Figure 5.5a.

The magnified view was especially useful because even on the scale of the fiber endface diameter, the cicada wings are largely non-planar. In fact, periodic undulations of several hundred microns were generally observable in cross-section, as is evident in Figure 5.5b, which placed a considerable portion of the mold surface out of the plane of the fiber endface. As a result, it was necessary to routinely identify a suitable mold region before imprinting. These regions were typically the peaks of the undulations, and their suitability for matching the endface plane was identified by bringing the mold and fiber into close proximity and observing the orientation of the endface reflection on the mold surface. This reflection was made observable by orienting the mold at a slight tilt relative to the viewing axis of the camera.

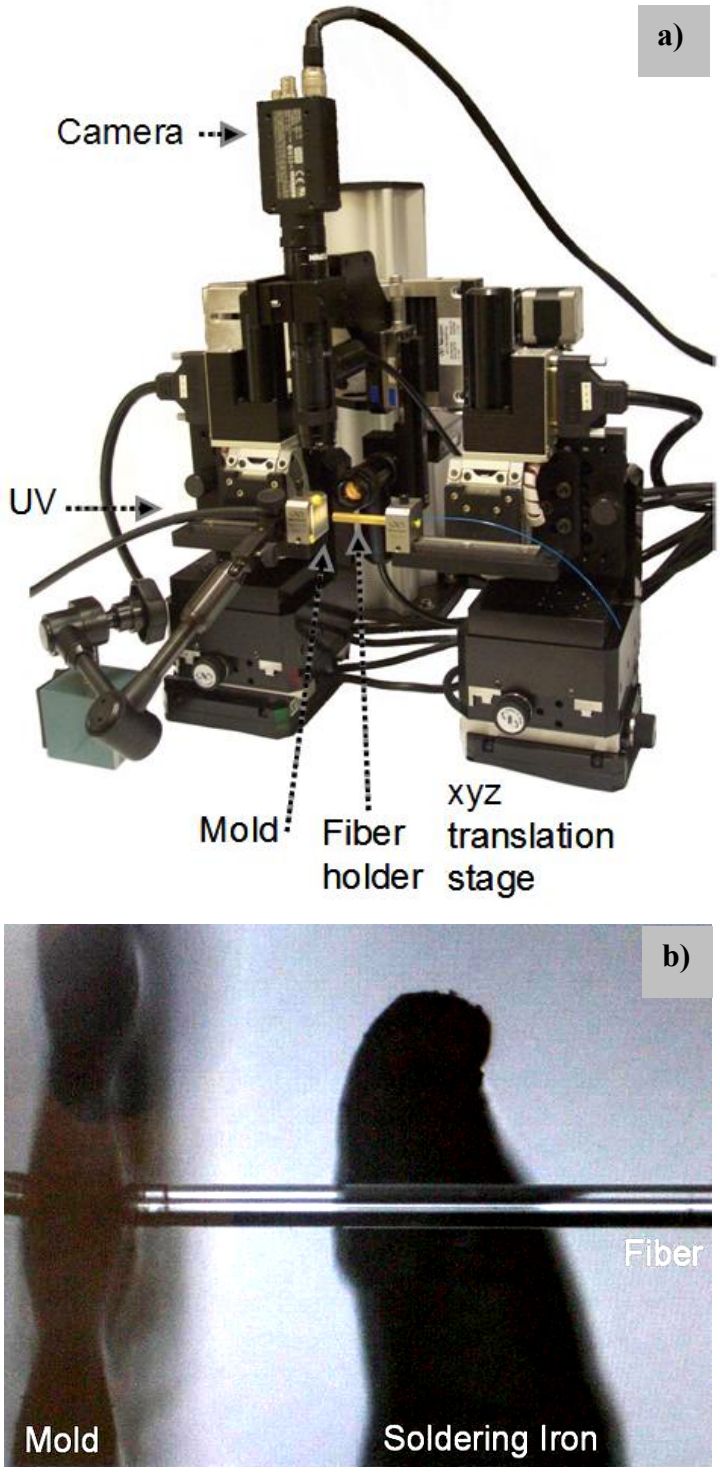

Figure 5.5: A photograph shows (a) the AutoAlign imprinting apparatus. The magnified image provided by this system shows (b) a fiber endface being imprinted against the non-planar h-PDMS mold, with the soldering iron tip in proximity. Note that the soldering iron shown in (b) is not present in (a).

5.4.1 Polymer selection and fiber coating

The negative epoxy based photoresist SU-8 2002 (Microchem) was selected for this work, because of its chemical and physical robustness. These properties are expected to provide excellent structural stability and to make it a permanent addition to the fiber endface once it is properly cured. The chemical, thermal and mechanical stability of the coating are all important parameters for the development of stable and repeatable SERS sensors.

The liquid SU8 was dispensed onto the fiber endface just before imprinting. The critical timing of coating in this instance is the direct result of the rapid evaporation of solvents from SU-8. This allowed a very short window in which to apply and imprint before it became excessively viscous.

The SU8 was dispensed onto the fiber endface by syringe which inevitably coated a section of the fiber length in addition to the fiber endface. The volume of polymer on the endface was largely dictated by surface tension and the low viscosity of SU8 2002. This distribution is visible in Figure 5.5b and is illustrated in Figure 5.6.

5.4.2 Fiber imprinting

Imprinting was conducted by bringing the coated endface into proximity with the mold so that it was wetted by the SU8, as illustrated in Figure 5.6, while avoiding physical contact between the two in order to prevent compression of the mold features. The gap between fiber and mold was reduced as much as possible, such that the final thickness of polymer that was added to the end of the fiber was typically ~15 μm, as shown in Figure 5.7. However this thickness varied between fibers and was rarely of uniform thickness across the endface.

Once the mold and the fiber endface were satisfactorily positioned with respect to one another, the SU8 film was cured. The requisite three steps are a soft bake to expel solvents, an exposure to ultraviolet light to photoinitiate cross-linking and finally a post bake to complete the cross-linking process.

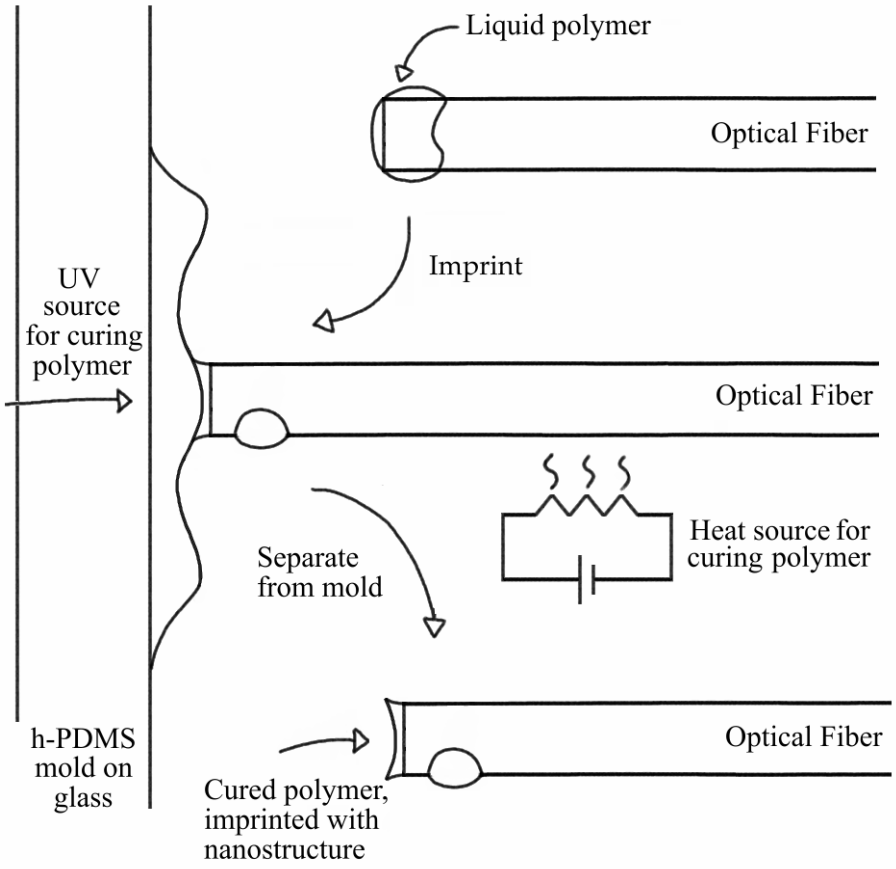

Figure 5.6: The optical fiber imprinting process.

The thermal energy was delivered to the fiber endface by means of a variable temperature soldering iron (Advanced JBC 2200), which was positioned within a fraction of a millimeter immediately below the optical fiber, at a distance of about 800 μm from the endface, as shown in Figure 5.5. The heat was transferred from the soldering iron to the fiber by convection and then by conduction along the fiber to the endface polymer, resulting in the temperature of the endface polymer being far below that of the soldering iron.

For the softbake step, the soldering iron temperature was incrementally increased up to 325^{o}C through thirty second intervals at each of 150^{o}C, 200^{o}C and 250^{o}C. This increase in temperature first forced the evaporation of solvents from the SU-8 2002 and then brought the SU-8 2002 beyond its glass transition temperature. This transition was observable as a reflow and redistribution of the SU-8 2002. This softbake temperature of 325^{o}C was maintained for five minutes to ensure complete evaporation of solvents, after

which the polymer was returned to room temperature through one minute at each of 250^{o}C, 200^{o}C and 150^{o}C.

The endface polymer was then optically exposed with UV light from a Novacure 2100 UV source. The exposure was directed through the mold, along the axis of the fiber, at a setting of 4W for a duration of four and a half minutes. This power was delivered through two 5 mm diameter optical waveguides, only one of which was directed at the fiber.

The post-bake step was then initiated by ramping the soldering iron up to a temperature of 375^{o}C, through one minute each of 150^{o}C, 200^{o}C, 250^{o}C and 325^{o}C, bringing the endface polymer up to an estimated 150^{o}C, where it was held for five minutes. This bake step acted to crosslink the SU8 and thus complete its curing. The fiber was then returned to room temperature by ramping the soldering iron temperature down through one minute each at 325^{o}C, 250^{o}C, 200^{o}C and 150^{o}C. The fiber was then separated from the mold, completing the transfer of the cicada nanostructure to the optical fiber.

On average, the entire imprinting process, from fiber stripping and cleaving to separation, took 45 minutes. The successful transfer of the cicada patterns to the optical fiber endface is shown in Figures 5.7d and 5.7e. The replicated nanostructure shows remarkably high fidelity, with excellent definition of each individual feature, and near flawlessness uniformity across the entire fiber endface.

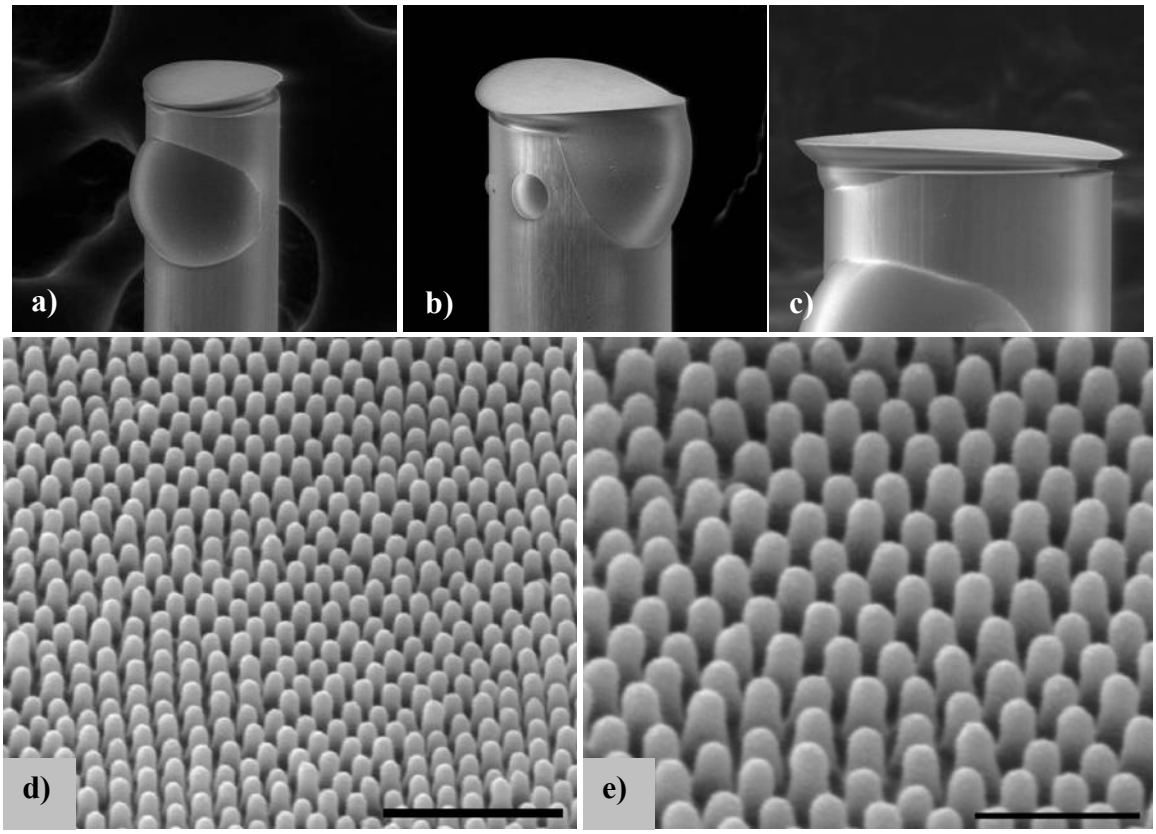

Figure 5.7: SEM images showing a-c) the imprinted endface of a 125 μm diameter optical fiber and d-e) the imprinted nanostructure. Scale bars are 1 μm and 500 nm.

5.4.2.1 Polymer behavior during thermal reflow

The thermal reflow of the endface polymer during the softbake step was the source of some activity during the imprinting process, and so a brief account of its behavior is offered here.

Two variables dominated the reflow behavior. The first was the volume of polymer that was deposited on each fiber tip, which was distributed over the endface as well as some length of fiber shaft, as illustrated in Figure 5.6. This fiber length was typically of the order of 250 μm. The second was the manual positioning of the soldering iron relative to the fiber, which subtly varied the thermal treatments received by the numerous fibers.

The polymer reflow was typically observed to begin in the polymer that was closest to the fiber hot spot, directly above the soldering iron. The polymer then exhibited progressive melting in accordance with the conduction of heat from the hotspot towards the fiber tip. This resulted in the melted polymer being drawn by surface tension, towards

any cooler or unmelted polymer, which was further away from the hotspot. Eventually the entire bulk of polymer would melt, whereupon surface tension would induce the polymer that was on the sides of the fiber, to break contact with the polymer on the fiber endface. This produced the separate regions of polymer visible in Figures 5.7a and 5.7c.

However, it was possible to reunite these separate regions of polymer by reducing the gap between fiber endface and the mold such that the endface polymer was forced to flow beyond the boundary of the fiber endface and back along the fiber, to make contact with the side polymer. This resulted in this side polymer flowing towards the endface and participating in the wetting of the mold surface, as is evident in Figure 5.7b. This sudden increase in the volume of the endface polymer could be used to wet a larger area of the mold surface, while it could also be considered to provide mechanical support to the endface polymer.

Additionally, and quite significantly, it was observed that once the polymer had been melted in this softbake step, its viscosity was low enough for it to fill the mold patterns. This was confirmed by comparing fibers that had been imprinted with freshly deposited liquid polymer, which derived its liquidity from its solvent content, and those realized by delaying imprinting until after the solvents had been evaporated and the polymer had been melted. No difference was observed in replica quality. This indicates that there is room for the optimization of this fabrication process, which will be the subject of future investigations, and that this process is somewhat of a hybrid between the soft imprinting of a liquid polymer, and the hot embossing of a thermally softened polymer.

5.4.2.2 Spontaneous separation and polymer shrinkage

Occasionally fibers were observed to have localized defects on their patterned endfaces. In considering the possible sources of these defects, it was noted that it was not uncommon for the fiber to separate spontaneously from the mold during the final two curing steps. The precise moments of separation were difficult to identify, since the associated physical displacement is assumed to be on the order of microns. Thus the spontaneous separation was observed only indirectly at the end of the curing process,

wherein the cured polymer would offer absolutely no resistance to being separated from the mold.

Previous publications have reported similar spontaneous releases during the curing of the h-PDMS on its master structure and have cited thermal and chemical shrinkage as the cause [51]. In this instance, it is expected that similar behavior within the SU-8 itself contributes significantly to this separation. This is supported by the observation of significant shrinkage of the SU8 at the end of the soft bake step, where the SU8 is cooled down and makes the transition from liquid to solid. This shrinkage is occasionally so severe that the SU8 can be observed to creep along the fiber endface towards the fiber core, although this same creep is not observed across the mold surface. This creep is observable at the edges of the fiber endfaces in Figures 5.7a and 5.7c, where the polymer has drawn away from the edge of the endface.

5.5 Coating the polymer nanoarray with metal

Once the fiber endface had been imprinted with the cicada nanostructure, a SERS capability was added by coating it with high purity silver (ProSciTech) [49]. The silver was deposited under the directional flux of a thermal evaporator (Emitech K950X) to a planar thickness of 60 nm, as reported by a quartz crystal microbalance (Emitech K150). The fiber endface was oriented so that the flux was incident at an angle of 60^{o} from the fiber axis, with the intention of employing the nanopillars as shadow masks, as discussed in Section 4.1.3 and Section 4.4, and thus creating isolated metal deposits. Cicada wings were coated in tandem with the imprinted fibers in order to provide reference surfaces for SERS measurements.

The close packing of the cicada nanofeatures largely restricted the deposition of material to the top of each nanofeature, as shown in Figure 5.8. However, a variation was observed in the amount of sidewall of each protrusion that was coated. This was attributed to the curvature of the imprinted surface, which resulted in the deposition of material over a range of angles, rather than the intended 60^{o}.

The silver deposits covered up to 75% of the plane of the substrate, as determined by histograms of the high-contrast normal incidence SEM images of Figure 5.8.

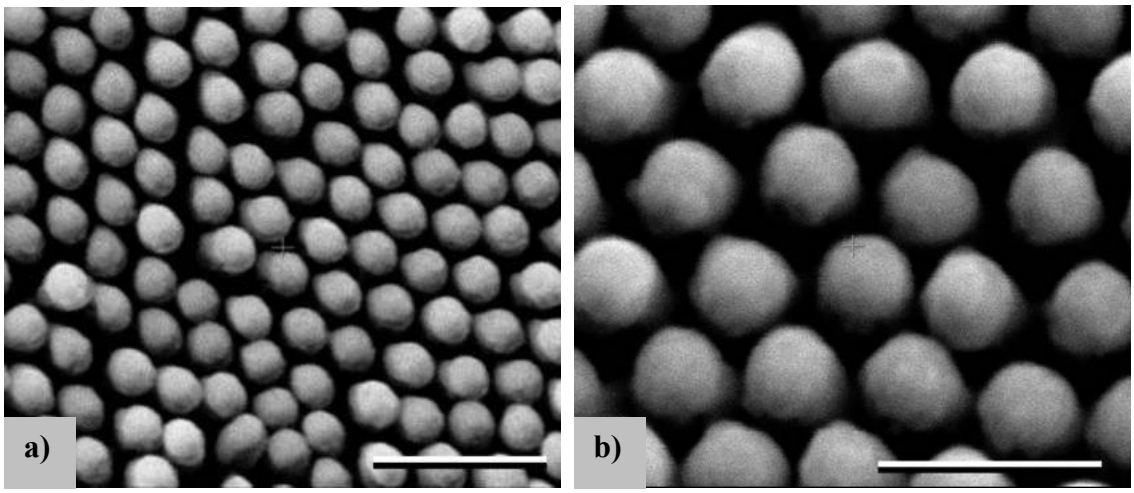

Figure 5.8: SEM images of silver coated fiber imprints. Broad (a) and close-up (b) views are shown, with scale bars of 500 nm and 300 nm respectively.

5.6 Plasmonic absorbance

As an aside to the fabrication of the fiber sensors, plasmonic absorbance measurements of gold coated cicada wings are presented here. These measurements do not have direct bearing on the SERS measurements taken from the silver coated wings and replicas, but they do serve to demonstrate the plasmonic activity of these antireflection nanotemplates when they are appropriately coated. Time constraints have prevented these measurements from being repeated with silver coatings.

The gold coating of the cicada wings was performed by a Balzers electron beam evaporation system. A thickness of 200 nm was deposited at an oblique angle of incidence. Transmission measurements were obtained by illuminating the coated wings with a tungsten source from an inverted microscope and directing the transmitted light via optical fiber to a spectrometer (Ocean Optics USB2000).

Figure 5.9 contrasts light transmitted through the coated wing, and that transmitted through a planar film of the same thickness on an adjacent glass slide. An absorbance peak is clearly visible at 513 nm in the nanostructured gold, while this peak is absent from the planar film measurement. Drip coating the wing with methanol changed the refractive index of the medium in which the gold nanodeposits were located, to induce a shift of 17 nm, from 513 nm to 530 nm. This peak was then observed to return to its

original position as the methanol evaporated. These complementary nanostructured and planar film absorbances are characteristic of each type of deposit [10].

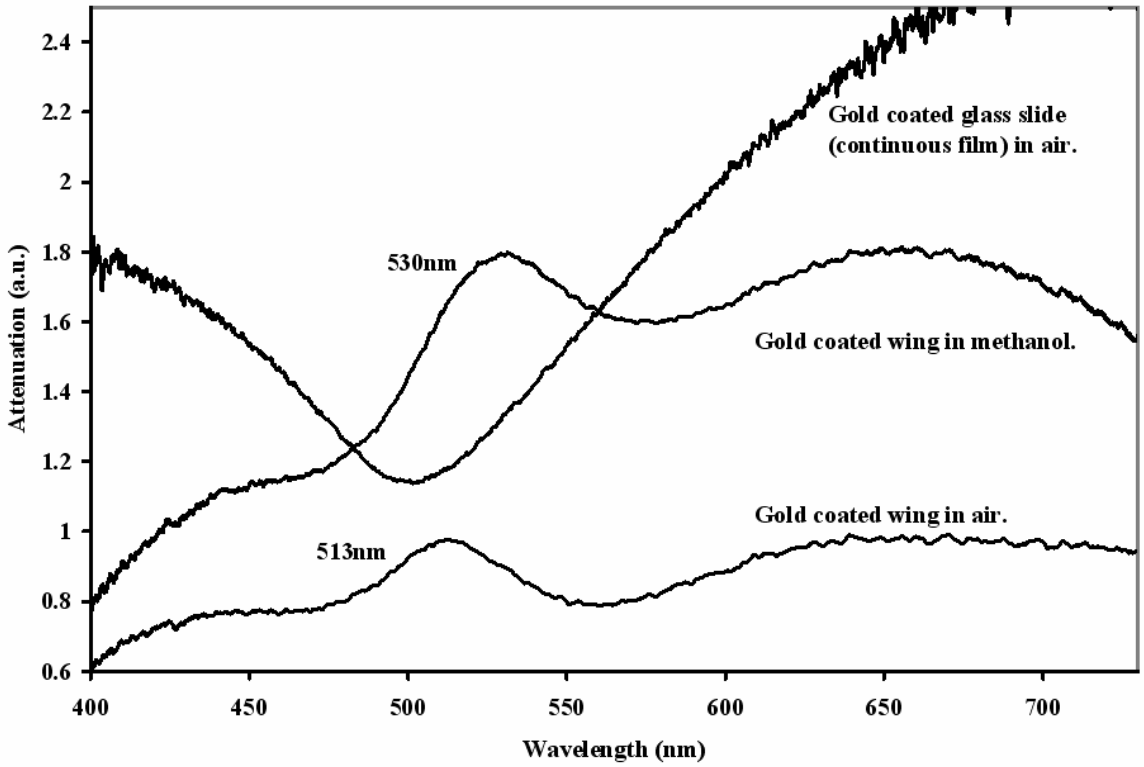

Figure 5.9: Plasmon resonances of cicada wings coated with 200 nm of Au shown in two mediums of different refractive index, and contrasted against the absorbance spectrum of a planar film of gold of the same thickness, on a glass substrate.

Knowing the precise plasmon resonance of a nanostructured surface is important in engineering a SERS substrate. An optimized SERS enhancement effect is reportedly achieved if the plasmon resonance is tuned to either match the illuminating wavelength [55], or to be between the illuminating wavelength and the raman shifted lines of interest [22], so that both are overlapped by the resonance.

Repeating these measurements with a silver coating will make it possible to tune the plasmonic behavior of the cicada nanostructure by adjusting coating conditions, thus allowing for the SERS performance of the imprinted fiber sensors to be optimized.

5.7 SERS analyte

Thiophenol was selected as the reference Raman-active analyte because it forms a stable self-assembled monolayer (SAM) on silver surfaces. Both the fiber tips and cicada wings were immersed for 10 minutes in a 10 mM solution of thiophenol (99+%, Sigma-Aldrich) in ethanol. A one minute rinse in pure ethanol was then used to remove excess thiophenol that was not attached as part of the SAM. Note that thiophenol is a highly toxic substance.

5.8 SERS measurements

While the visual confirmation of successful replication is encouraging, the real test of this endeavor is the collection of SERS spectra from the fiber endfaces, especially as collected through the fiber. To this end, SERS spectra were collected in three backscatter interrogation modes, as illustrated in Figure 5.10. The first was by direct illumination of a cicada wing, for the provision of a reference SERS spectrum. The second was the performance of this same measurement using an imprinted fiber endface, to allow direct comparison with the cicada measurement. Finally, the spectrum was collected by launching light into the opposite end of the fiber, so that the fiber guided the exciting light to the endface, and then guided the scattered light back to the objective lens.

The apparatus used for these measurements was a modular Raman microscope (Horiba Jobin Yvon), fitted with a 50x objective (0.5 N.A.). The spectra were excited using a fiber-coupled 532 nm laser (OptoTech P/L). The scattered signal was coupled to a spectrometer (Jobin Yvon Triax 320) fitted with a thermoelectrically cooled CCD detector. In all cases, 5 accumulations of 3 seconds each were averaged together.

Direct illumination of the cicada wing with 0.3 mW generated a strong SERS spectrum, plotted in the upper curve of Figure 5.11. Here it is contrasted against the same measurement taken from a replica on an optical fiber endface. Each spectrum is dominated by the same characteristic thiophenol peaks at 1572 cm^{-1}, 1071 cm^{-1}, 1021 cm^{-1}, 1001 cm^{-1}, 692 cm^{-1} and 422 cm^{-1}, conclusively confirming the successful replication of the cicada nanostructure. Increasing the illuminating power beyond 0.3 mW was found to cause thermal damage to the replica and thus prevent the acquisition of characteristic

spectra. The higher counts evident in the cicada spectrum are attributed to the secondary illumination of the cicada wings, which was contributed by reflection from the glass slides on which they were mounted.

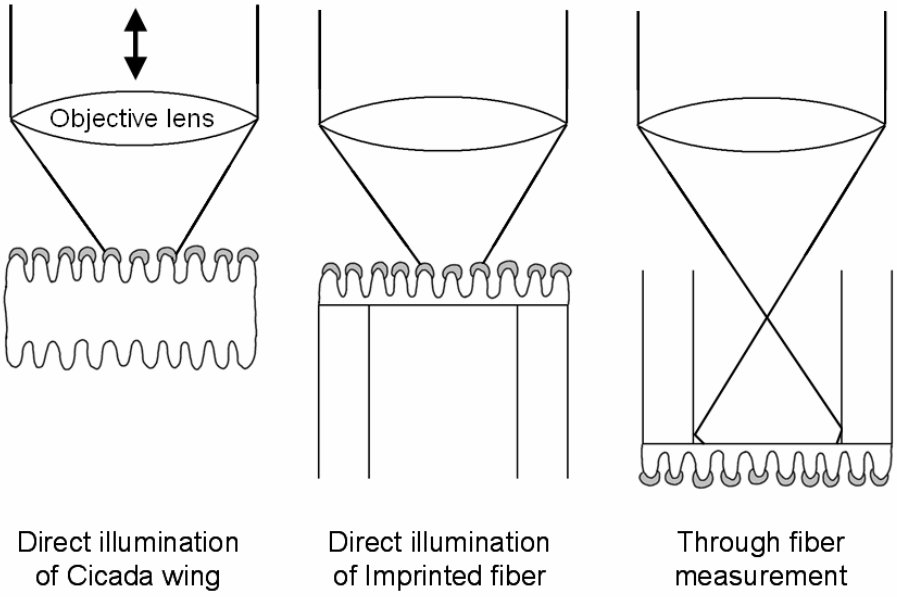

Figure 5.10: Diagram of SERS measurement orientations.

The imprinted endface was then interrogated through the fiber to generate the distinct spectra shown in Figure 5.12. The first of these spectra was acquired at 0.3 mW, the same as that used in direct illumination measurements. This power level was found to generate significantly reduced counts than in direct illumination mode, however this was attributed to the diffuse illumination and thus lower power densities that result from guiding through the fiber to illuminate the endface. The second spectrum was acquired using an increased optical power of 2.6 mW. This resulted in dramatically increased signal counts to produce impressive characteristic peaks.

Unexpectedly, these through-fiber spectra were generally observed to have flatter baselines than the direct imprint or cicada measurements. This has resulted in many of the smaller characteristic peaks becoming more evident. These peaks are observed at 1471 cm^{-1}, 1180 cm^{-1}, 1107 cm^{-1} and 470 cm^{-1}. Increasing the optical power further was found to thermally damage the cleaved silica endface, however higher powers could

potentially be used by defocusing the beam at the input face of the fiber or by using a lower power objective.

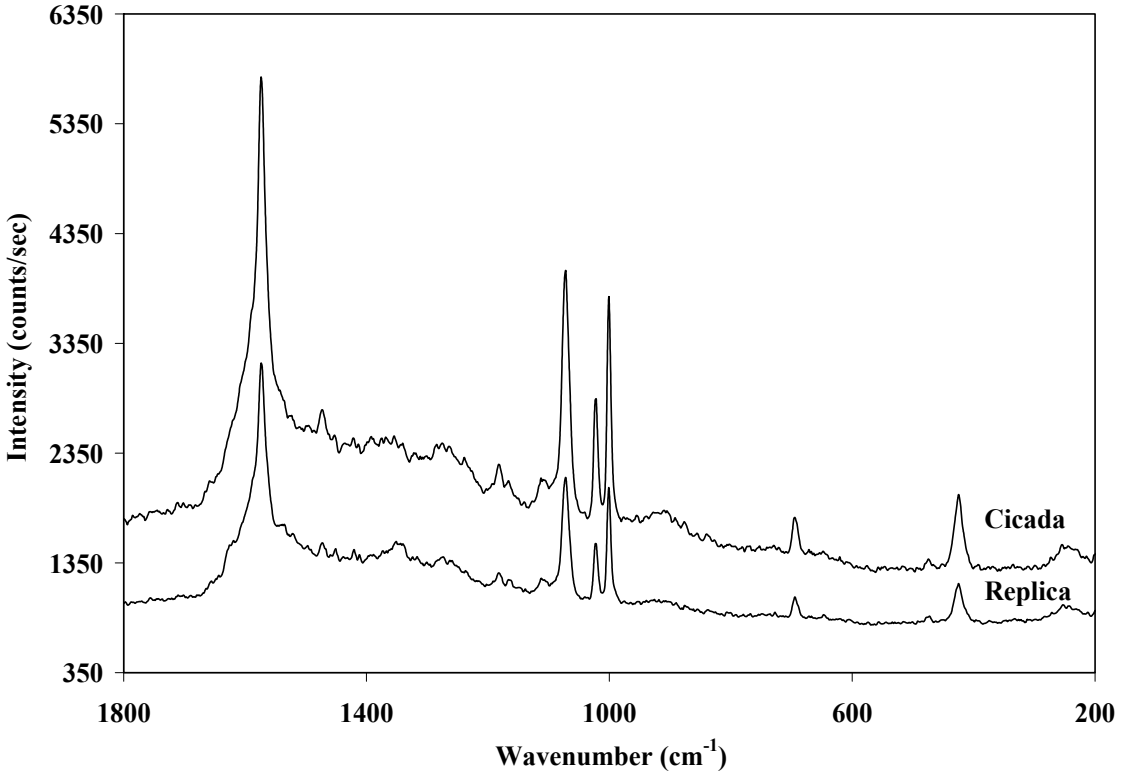

Figure 5.11: Direct illumination SERS measurements from a cicada wing and from a replica on a fiber tip are contrasted. Both spectra were taken with an illumination power of 0.3 mW.

The post-acquisition processing of these direct illumination and through fiber spectra was limited to the simple rescaling of the intensity axis to units of counts per second. This highlights the excellent signal to noise ratio of the through fiber measurements. Note that the peak at 1001 cm^{-1} in the 2.6 mW spectrum Figure 5.12 has a full-width at half-maximum of just 9 cm^{-1}.

These results demonstrate that imprinting optical fiber endfaces is a viable technique for fabricating optical fiber SERS probes. Additionally, the suitability of the cicada nanostructure as a convenient template for replication and its reliability as a high sensitivity SERS template are both reinforced.

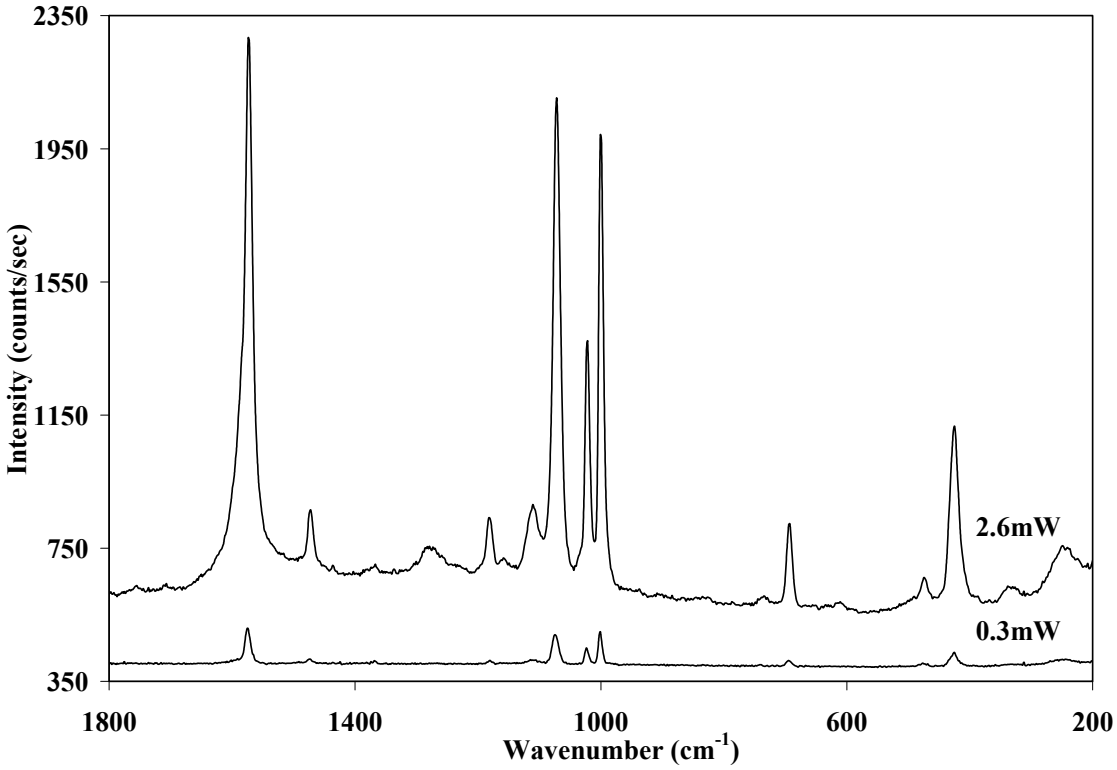

Figure 5.12: Through fiber SERS measurements demonstrating signal scaling with illuminating power for 0.3 mW and 2.6 mW.

5.8.1 Influence of optical coupling alignment

The distinctiveness of the characteristic peaks in these through-fiber spectra was found to have little dependence on whether the light was coupled into the core or cladding of the cleaved fiber endface, as shown in Figure 5.13. Although there was a change in signal counts, the primary difference was the reduction of a broad silica peak at 450 cm^{-1} when measurements were conducted through the cladding. This may be the result of different optical path lengths through the fiber or different doping concentrations. In general terms, this similarity in performance makes careful coupling of these short lengths of fiber to the laser source unnecessary, making them well suited to field applications.

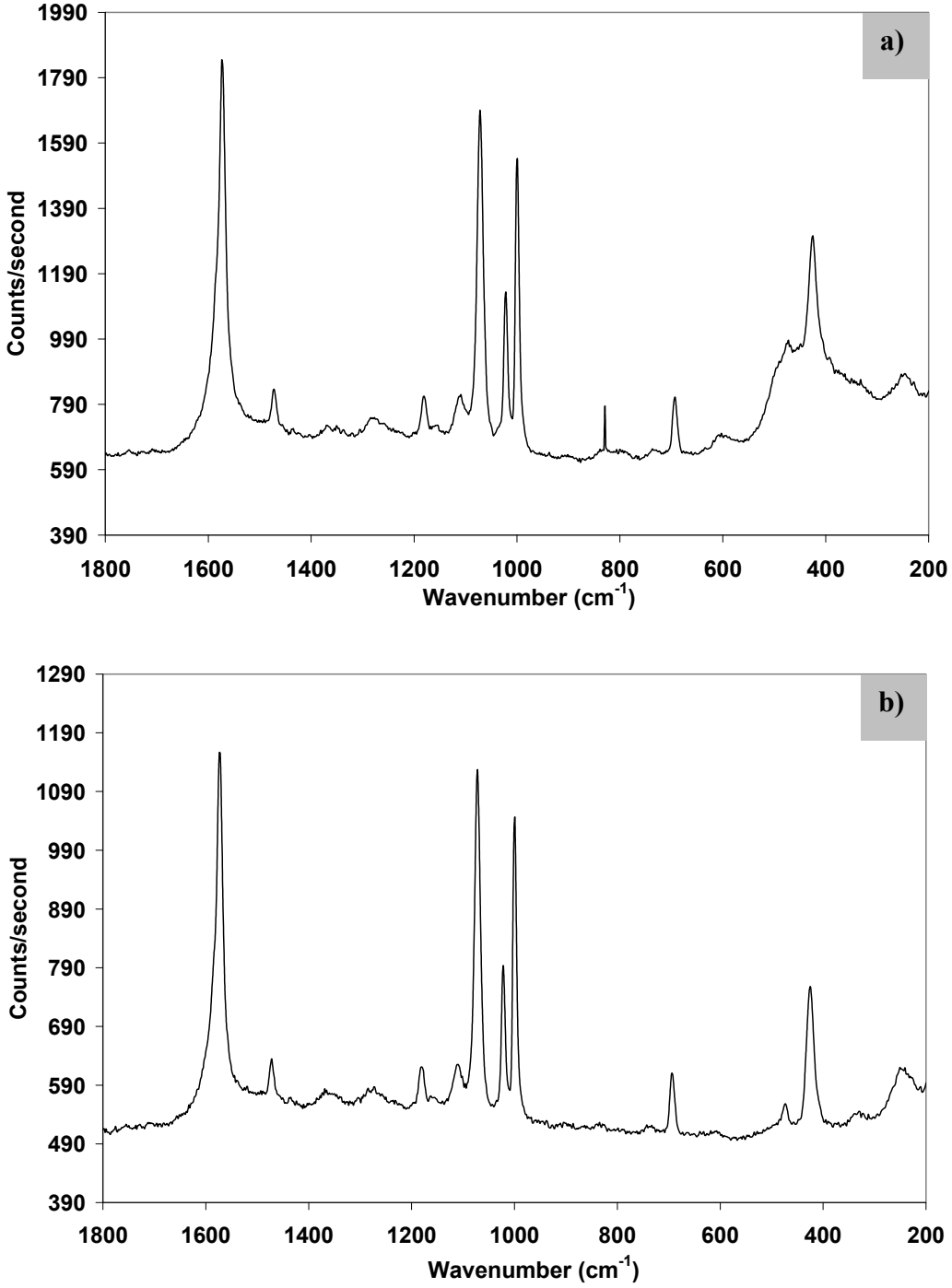

Figure 5.13: Through fiber SERS measurements showing little spectral dependence on coupling accuracy. Launches into (a) the fiber core and (b) the fiber cladding are contrasted.

5.9 Performance variations

Direct illumination of both original and replica structures has consistently demonstrated a large variation in spectrum baselines that is dependent on position. This variation is shown in Figure 5.14 for a cicada wing. However, note that direct illumination is also, on occasion, capable of producing flat baselines. Conversely, the through fiber measurements have been much more consistent in exhibiting these flat baselines. The baseline of a SERS spectrum is of interest because of its ability to obscure or elucidate characteristic peaks. A flat baseline translates to easily identifiable peaks and thus improved sensitivity. As a result, this variation warrants some attention.

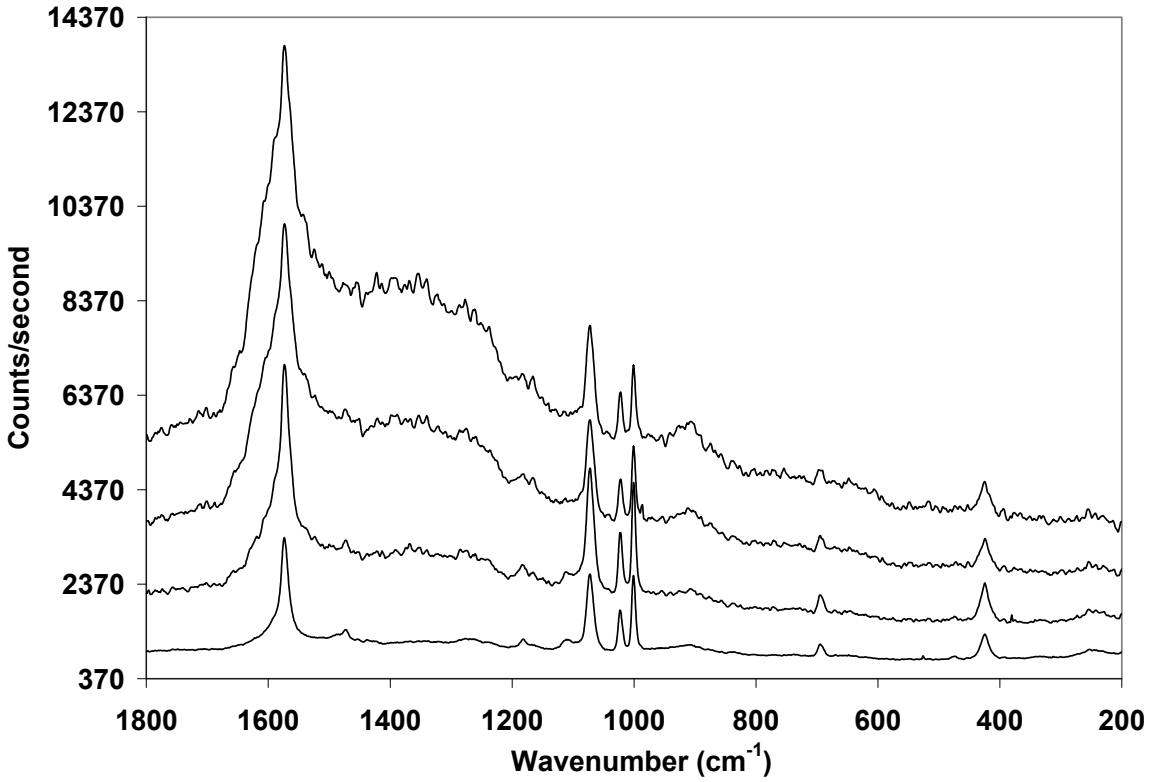

Figure 5.14: Numerous cicada wing SERS measurements taken at different locations across the surface of the wing, demonstrating spectrum variation.

Although the source of these variations has not yet been identified, and an in-depth analysis is beyond the scope of this thesis, a useful starting point is to consider sources of variation in both the active surface and the interrogation modes. To this end, note that the

hexagonal domains of the cicada structure are about 1.5 μm in size, roughly equal to the illuminated surface area in direct illumination mode using a 50x objective lens. This may bring into play preferential orientations of the hexagonal domains, relative to the polarization of the illumination source. Furthermore, the topography of the cicada wing makes it unavoidable that the nanostructures will be subjected to a range of incident angles during metal deposition, resulting in some variation in the size and shape of the metal deposits across the surface. Additionally, the topography is likely to alter the spatial distribution of the scattered light during direct illumination measurements. The focused spot size in direct illumination will be subjected to the brunt of these variations, while the large area illumination of the through-fiber interrogation will generate more of an average of all of the structures over the 50 μm diameter core endface. These are all issues that need to be investigated in the future development of this sensor.

5.10 Consequences for nanoimprint lithography

One of the main appeals of replication techniques such as this is the sheer number of replicas that can be derived from a single master pattern. In the traditional large substrate application, tens and even hundreds of replicas have been reported from a single mold with little loss in pattern fidelity. However a comparison of the surface area of a fiber endface, which has a diameter of 125 μm, with that of a mold that is millimeters across, quickly reveals that a single mold could potentially imprint hundreds of fibers without using the same surface more than once. Thus, a single mold in this application could potentially imprint thousands or even tens of thousands of fibers in its lifetime, a dramatic improvement over large substrate imprinting. This large mismatch in mold/endface surface areas could even lend itself to imprinting bundles of fibers, so that the single-run processing time of 45 minutes could conceivably yield hundreds of functional devices. This would fulfill the mass fabrication ambitions of nanoimprint lithography, albeit as a photonics platform rather than the intended silicon wafers of the semiconductor industry.

In spite of the superior resolution of h-PDMS, one of the main detractors from its widespread adoption is its susceptibility to fracture [51]. However, it should be noted that fractures only occur in the instance of flexing, something that is necessary in performing

gradual separation from a large substrate. Fortuitously, this application avoids mold flexing at all times by having a master structure that is flexible and thus capable of peeling, and an imprinted substrate of dimensions that allow instantaneous separation from the mold. Both situations obviate the need for extraneous flexing, minimizing the possibility of fracture and making fiber imprinting an ideal application of this higher resolution material.

5.11 Conclusions

In closing, the until now exclusive fields of optical fibers and nanoimprint lithography have been successfully combined to provide a quick, economical and high resolution technique for fabricating optical fiber SERS sensors. The replicated structure was biological in origin and had dimensions and density that would challenge many current state-of-the-art fabrication schemes. The imprinted fiber has demonstrated sufficiently high sensitivity in through-fiber SERS sensing to warrant further development. Some of the avenues that will be pursued in future work include up-scaling fabrication, employing longer lengths of fiber, demonstrating detection of other analytes such as glucose [22,56] and optimizing surface enhancement by e-beam master design. In fact, it is this last possibility that is the lynchpin in the potential for future work that has been elucidated by this demonstration. An e-beam system provides absolute control over the master structure design, and since the patterns replicated by nanoimprint lithography can be completely arbitrary, it opens the door to the development of entire suites of optical fiber sensors.

Finally, in the context of the present demonstration, and considering the logistics of capturing and storing the seasonally available cicada, it should be noted that an examination of cicadas that were captured in 1953 revealed that their wings were still largely usable, save for some superficial grime and mechanical abrasion. Both of these sources of damage can be avoided by more careful capture and storage. However, only freshly captured specimens were utilized in the fabrication of devices.

5.12 References

1. S. A. Kalele, N. R. Tiwari, S. W. Gosavi, S. K. Kulkarni, *Plasmon-assisted photonics at the nanoscale*, Journal of Nanophotonics, 1, 012501, 2007.
2. E. Hutter, J. H. Fendler, *Exploitation of localized surface plasmon resonance*, Advanced Materials, 16, p. 1685, 2004.
3. W. L. Barnes, A. Dereux, T. W. Ebbensen, *Surface plasmon subwavelength optics*, Nature, 424, p. 824, 2003.
4. S. A. Maier, P. G. Kik, H. A. Atwater, S. Meltzer, E. Harel, B. E. Koel, A. A. G. Requicha, *Local detection of electromagnetic energy transport below the diffraction limit in metal nanoparticle plasmon waveguides*, Nat. Mat., 2, p. 229, 2003.
5. X. Luo, T. Ishihara, *Surface plasmon resonant interference nanolithography technique,* App. Phys. Lett., 84, p. 4780, 2004.
6. A. J. Haes, R. P. Van Duyne, *Preliminary studies and potential applications of localized surface plasmon resonance spectroscopy in medical diagnostics*, Expert Rev. Mol. Diagn., 4, p. 527, 2004.
7. S. Kawata, *Near-field optics and surface plasmon polaritons*, Springer Topics in Applied Physics 81.
8. E. Ozbay, *Plasmonics: Merging photonics and electronics at nanoscale dimensions*, Science, 311, p. 189, 2006.
9. W. Knoll, *Interfaces and thin films as seen by bound electromagnetic waves*, Annual Review of Physical Chemistry, 48, p. 569, 1998.
10. S. A. Maier, H. A. Atwater, *Plasmonics: Localization and guiding of electromagnetic energy in metal/dielectric structures*, Journal of Applied Physics, 98, 011101, 2005.
11. A. J. Haes, C. L. Haynes, A. D. McFarland, G. C. Schatz, R. P. Van Duyne and S. Zou, *Plasmonic materials for surface-enhanced sensing and spectroscopy*, MRS Bulletin, Vol. 30, p. 368, May 2005.
12. D. A. Long, *The Raman effect: A Unified treatment of the theory of Raman scattering by molecules*, John Wiley & Sons, LTD, 2002.

13. C. L. Haynes, A. D. McFarland, R.P. Van Duyne, *Surface-enhanced Raman scattering*, Anal. Chem, 77, 338A, 2005.

14. T. Vo-Dinh, F. Yan, M. B. Wabuyele, *Surface-enhanced Raman scattering for medical diagnostics and biological imaging*, J. Raman Spectrosc., 36, p. 640, 2005.

15. G. C. Schatz, R.P. Van Duyne, *Electromagnetic mechanism of surface-enhanced spectroscopy*, Handbook of vibrational spectroscopy, John Wiley: New York, p. 759, 2002.

16. M. Fleischmann, P. J. Hendra, A. J. McQuillan, *Raman spectra of pyridine adsorbed at a silver electrode*, Chem. Phys. Lett, 26, p. 163, 1974.

17. R. P. Van Duyne, J. Phys., 38, (C5)239, 1977

18. D. L. Jeanmaire, R. P. Van Duyne, J. Electroanal. Chem., 84, p.1, 1977.

19. M. G. Albrecht, J. A. Creighton, J. Am. Chem. Soc., 99, p. 5215, 1997.

20. K. Kneipp, Y. Wang, H. Kneipp, L. T. Perelman, I. Itzkan, R. R. Dasari, M. S. Feld, *Single molecule detection using surface-enhanced raman scattering (SERS)*, Physical Review Letters, 78, p. 1667, 1997.

21. S. Nie, S. R. Emmory, *Probing single molecules and single nanoparticles by surface-enhanced raman scattering,* Science, 257, p. 1102, 1997.

22. C. L. Haynes, C. R. Yonzon, X. Zhang, R. P. Van Duyne, *Surface-enhanced Raman sensors: early history and the development of sensors for quantitative biowarfare agent and glucose detection*, J. Raman Spectrosc., 36, p. 471, 2005.

23. A. E. Grow, L. L. Wood, J. L. Claycomb, P. A. Thompson, *New biochip technology for label-free detection of pathogens and their toxins*, J. Microbiol. Meth., 53, p. 221, 2003.

24. T. Vo-Dinh, L. R. Allain, D. L. Stokes, *Cancer gene detection using surface-enhanced Raman scattering (SERS)*, J. Raman Spectrosc., 33, p. 511, 2002.

25. Y. W. C. Cao, R. C. Jin, C. A. Mirkin, *Nanoparticles with Raman spectroscopic fingerprints for DNA and RNA detection*, Science, 297, p. 1536, 2002.

26. B. Moore, L. Stevenson, A. Watt, S. Flitsch, N. J. Turner, C. Cassidy and D. Graham, *Rapid and ultra-sensitive determination of enzyme activities using surface-enhanced resonance Raman scattering*, Nature biotechnology, 22, p. 1133, 2004.

27. A. M. Stacy, R. P. Van Duyne, *Surface enhanced Raman and resonance Raman spectroscopy in a non-aqueous electrochemical environment: tris(2,2'-bipyridine) ruthenium(II) adsorbed on silver from acetonitrile* , Chemical Physics Letters., 102, p. 365, 1983.

28. G. J. Kovacs, R. O. Loutfy, P. S. Vincent, C. Jennings, R. Aroca, *Distance dependence of SERS enhancement factor from Langmuir-Blodgett monolayers on metal island films: evidence for the electromagnetic mechanism,* Langmuir, 2, p. 689, 1986.

29. L. A. Dick, A. D. McFarland, C. L. Haynes, R. P. Van Duyne, *Metal film over nanosphere (MFON) electrodes for surface-enhanced Raman spectroscopy (SERS): Improvements in surface nanostructure stability and suppression of irreversible loss,* Journal of Physical Chemistry B, 106, p. 853, 2002.

30. K. Mullen and K. T. Carron, *Surface-enhanced Raman spectroscopy with abrasively modified fiber optic Raman probes*, J. Am. Chem. Soc., 63, pp 2196, 1991.

31. C. Viets and W. Hill, *Fiber-optic SERS sensors*, Internet Journal of Vibrational Spectroscopy, Vol. 4, 2000, http://www.ijvs.com

32. E. Polwart, R. L. Keir, C. M. Davidson, W. E. Smith and D. A. Sadler, *Novel SERS-active optical fibers prepared by the immobilization of silver colloidal particles*, Applied Spectroscopy, 54, p. 522, April 2000.

33. D. L. Stokes and T. Vo-Dinh, *Development of an integrated single-fiber SERS sensor*, Sensors and Actuators B, 69, p. 28, 2000.

34. C. Shi, H. Yan, C. Gu, D. Ghosh, L. Seballos, S. Chen, J. Z. Zhang, B. Chen, *A double substrate "sandwich" structure for fiber surface enhanced Raman scattering detection*, App. Phys. Lett., 92, 103107, 2008.

35. D. J. White and P. R. Stoddart, *Nanostructured optical fiber with surface-enhanced Raman scattering functionality*, Optics Letters,. 30, p.598, 2005.
36. J. Kim, M. Han, S. Chang, J. W. Lee and K. Oh, *Achievement of large spot size and long collimation length using UV curable self-assembled polymer lens on a beam expanding core-less silica fiber*, IEEE Photonics Technology Letters,. 16, p. 2499, 2004.
37. S. Choi, K. R. Kim, K. Oh, C. M. Chun, M. J. Kim, S. J. Yoo and D. Y. Kim, *Interferometric inscription of surface relief gratings on optical fiber using azo polymer film*, App. Phys. Lett., 83, p. 1080, 2003.
38. R. Bachelot, C. Ecoffet, D. Deloeil, P. Royer and D. Lougnot, *Integration of micrometer-sized polymer elements at the end of optical fibers by free-radical photopolymerization* , Applied Optics, 40, p. 5860, 2001.
39. H. Sakata and A. Imada, *Lensed plastic optical fiber employing concave end filled with high-index resin*, Journal of Lightwave Technology, 20, p. 638, 2002.
40. J. A. Rogers, M. Meier, A. Dodabalapur and E. J. Laskowski, *Distributed feedback ridge waveguide lasers fabricated by nanoscale printing and molding on nonplanar substrates*, App. Phys. Lett., 74, p. 3257, 1999.
41. Xia, Y., Kim, E., Zhao, X., Rogers, J. A., Prentiss, M. and Whitesides, G. M., *Complex optical surfaces formed by replica molding against elastomeric masters*, Science, 273, p.347, 1996.
42. X. Zhao, Y. Xia and G. M. Whitesides, *Soft lithographic methods for nano-fabrication*, J. Mater. Chem., 7, p. 1069, 1997.
43. P. Vukusic and J. R. Sambles, *Photonic structures in biology*, Nature, 424, p. 852, 2003.
44. K. Jeong, J. Kim, L. P. Lee, *Biologically inspired artificial compound eyes*, Science, 312, p. 557, 2006.
45. G. Zhang, J. Zhang, G. Xie, Z. Liu, H. Shao, *Cicada wings: A stamp from nature for nanoimprint lithography*, Small, 2, p. 1440, 2006.
46. D. G. Stavenga, S. Foletti, G. Palasantzas and K. Arikawa, *Light on the moth-eye corneal nipple array of butterflies*, Proceedings of the Royal Society B, 273, p. 661, 2006.

47. A. Yoshida, M. Motoyama, A. Kosaku and K. Miyamoto, *Antireflective nanoprotuberence array in the transparent wing of a hawkmoth, Cephonodes Hylas*, Zoological Science, 14, p. 737, 1997.
48. G. S. Watson, J. A. Blach, *Characterisation of cuticular nanostructures on surfaces of insects by Atomic Force Microscopy – 'mining' evolution for smart structures*, Proc. SPIE, 4934, p. 378, 2002.
49. P. R. Stoddart, P. J. Cadush, T. M. Boyce, R. M. Erasmus and J. D. Comins, *Optical properties of chitin: surface-enhanced Raman scattering substrates based on antireflection structures on cicada wing*, Nanotechnology, 17, p. 680, 2006.
50. M. S. Moulds, *Australian Cicadas*, New South Wales University Press, January 1990.
51. H. Schmid and B. Michel, *Siloxane polymers for high-resolution, high-accuracy, soft lithography*, Macromolecules, 33, p. 3042, 2000.
52. T. W. Odom, V. R. Thalladi, J. C. love, G. M. Whitesides, *Generation of 30-50 nm structures using easily fabricated, composite PDMS masks*, J. Am. Chem. Soc., 124, p. 12112, 2002.
53. H. Kang, J. Lee, J. Park, H. Lee, *An improved method of preparing composite poly(dimethylsiloxane) moulds*, Nanotechnology, 17, p. 197, 2006.
54. F. Hua, Y. Sun, A. Gaur, M. A. Meitl,, L. Bilhaut, L. Rotkina, J. Wang, P. Geil, M. Shim and J. A. Rogers, *Polymer imprint lithography with molecular-scale resolution*, Nano Letters, 4, p. 2467, 2004.
55. G. Gauglitz, T. Vo-Dinh, *Handbook of Spectroscopy*, Wiley-vch Verlag GmbH & Co. KGaA, Weinheim, 2003.
56. K. E. Shafer-Peltier, C. L. Haynes, M. R. Glucksberg and R. P. Van Duyne, *Toward a Glucose Biosensor Based on Surface-Enhanced Raman Scattering*, J. Am. Chem. Soc., 125, p. 588, 2003.

Chapter 6.

Conclusions and Future Direction

The objective of this thesis was to explore and develop the potential of inherently low-cost elastomer based replication techniques by investigating opportunities in device applications, master structure fabrication, biotemplating and choices of imprintable substrate. These objectives have been satisfied by the demonstration of a novel implementation of planar integrated optical device, the development of two novel nanolithographic techniques, and the development of a new optical fiber based SERS sensor. A summary of each of these achievements is given below.

6.1 Outcomes of this work

Chapter 3 gave the first demonstration of photolithography and replication in this thesis, wherein a photoresist master pattern was replicated by soft imprinting into polymer to create planar dielectric rib waveguides. Mode profiles demonstrated that these waveguides exhibited single mode guiding at 1550 nm and multimode guiding at

632.8 nm. These waveguides were then integrated with a LPG in a two step imprinting process to demonstrate, for the first time, a completely replicated LPWG device. The gratings were placed at the lower cladding core interface, where a transmission spectrum demonstrated that they induced a wavelength resonance at 1585 nm with a bandwidth of 12 nm.

Chapter 4 then moved to demonstrate that the nanoscale sidewall corrugations on photolithographically patterned photoresist can be applied to scale reduction nanolithography. The first of two techniques demonstrated the transfer of the corrugations to an elastomeric cast, which was in turn used as a sidewall photolithography mask, wherein the sidewall corrugations were employed as optical masking elements. The photoresist features defined by this mask were located directly beneath the sidewall corrugations and had widths of the order of 80 nm, consistent with the depths of the corrugations.

The second technique demonstrated what is perhaps a simpler application of standing wave corrugations, although it demonstrates both a superior resolution and an inherent capacity to fabricate in three dimensions. Here, the vertical periodicity and the subtle lateral offset of one corrugation relative to the next was exploited to create a vertically stacked, nanoscale shadow template which was placed in the path of an evaporated flux. The arbitrary shapes that can be defined by photolithography and the range of materials that can be deposited by evaporation make this technique extremely versatile. Stacks of nanowire, nanoribbon and multilayer features were demonstrated, arranged into both straight lengths and circular loops. Numerous materials, including Au, Ti, SiO_2 and Pt were used to demonstrate feature widths as small as 16 nm.

Chapter 5 combined the concepts of waveguiding and nanofabrication that were employed in Chapters 3 and 4 to demonstrate a novel optical fiber based SERS sensor. Nanoimprint lithography was applied for the first time to the endface of an optical fiber, where it was used to transfer a dense array of nanopillars from a biological template. The nanopillars were cast from the wings of a cicada, where they serve as a broadband, subwavelength antireflection structure. Initial attempts at casting were made with the same PDMS that was used in Chapters 3 and 4. However, SEM analysis revealed that the density and dimensions of this pattern were too severe for the reliable use of PDMS.

Instead, the more rigid h-PDMS was successfully employed. After coating the nanostructures with metal, SERS measurements were obtained by direct interrogation from both the cicada wings and the endface replicas. These measurements were then contrasted to confirm both the fidelity of the replicas and their functionality. These replicated structures were then interrogated through the fibers, which guided both the exciting and the scattered light, to successfully obtain characteristic spectra. These spectra exhibited distinct resonances with impressive signal to noise ratios. These measurements demonstrate the successful integration of a biological nanostructure with an optical fiber to create a novel optical fiber SERS sensor with the inherent capacity for remote and in-situ sensing.

6.2 Suggestions for future work

The prospects for future work in these innovations can be divided into two areas – the refinement of these techniques, and the potential to derive further innovation from these works. These are discussed here.

The most immediate improvement that could be made to the planar integrated optical devices is their implementation using lower loss polymers. Beyond this, it would be informative to quantify the impact that variations in device geometry, caused by the imprinting process, have on the device resonance. To this end, perhaps alternative replication approaches could be investigated. The fabrication of both waveguide and grating in a single step might address these variations to some extent, while also reducing the fabrication time of the device.

The two sidewall corrugation lithography techniques have demonstrated that, in spite of the routine suppression of photolithographic standing wave corrugations, they possess a great deal of untapped potential for nanofabrication. While other templates of similar nanofeatures do exist, these photoresist corrugations are uniquely interesting because of the ubiquity of photolithography, which makes them extraordinarily accessible and thus potentially very useful.

The elastomeric scattering mask represents a convenient technique for performing sub 100 nm photolithography using little more than micron-capable photolithography equipment. The potential applications of nanometer wide lines and gaps need not be

outlined here. However, it would be interesting to explore the capacity that this technique has for further scale reduction, in conjunction with a higher resolution casting material such as h-PDMS. Investigations could explore approaches for reducing the depths of the sidewall corrugations, or they could seek out alternative sources of sidewall roughness that could be employed as optical scatterers.

The primary concern with the vertically stacked nanowire technique is the discontinuities that were created by the photoresist surface roughness. As a result, it would be pertinent to investigate the performance of an ultrahigh resolution photoresist. A potential application of this technique is the use of the stacked nanowires as plasmonic resonators, wherein the resonances could be tuned by controlling both the thickness of the deposited material and the lengths/diameters of the nanowire shapes. Additionally, this technique could be applied to fabricating nanowires that are kilometers in length, by defining a corrugated photoresist template that is shaped like a spiral, or any other densely packed continuous line. Furthermore, the corrugated template could be transferred to an elastomer, whereupon the nanofeatures would be sustained by a transparent bulk. In their capacity as electrical conduits, it is difficult to propose how any single one of these wires could be addressed, however it would be possible to address the groups of nanowires on any given sidewall by performing a subsequent metal deposition in the form of a large electrode at the ends of the nanowire.

The imprinted optical fiber endfaces require an investigation into the sources of signal variation between direct and through fiber interrogation modes, as well as variations across the surface in direct interrogation. Their performance could also be optimized by investigating coating conditions, employing different excitation wavelengths and by experimenting with different optical fibers. Opportunities for the mass fabrication of imprinted fibers could also be developed by identifying process components that can be automated, and by implementing techniques for simultaneously handling bundles of fibers. In a broader context, this work has demonstrated that optical fiber endfaces are well suited as substrates for imprinting. Given that imprinting can replicate patterns of arbitrary shape, opportunities present themselves in the form of alternative master patterns. Experimenting with different patterns will allow for the

further optimization of SERS performance, as well as for the development of completely different kinds of optical fiber sensors.

In conclusion, this thesis has conceptualized and demonstrated several innovations by investigating elastomeric replication techniques. A consideration of application, master structure and substrate has yielded innovations spanning the fields of planar integrated optics, nanolithography, biomimetics, and SERS sensors. All demonstrations were performed quickly and at low cost, and are a testament to the versatility of elastomeric replication techniques and the cross-disciplinary appeal of their potential applications.

Appendix

List of publications

Refereed Journal Articles

1. Kostovski, G., White, D., Mitchell, A., Austin, M., Stoddart, P. R., *Nanoarray Device Fabrication by Imprinting: Replication of Biological Nanostructures on Optical Fibres for Surface-Enhanced Raman Scattering*. In preparation.

2. Kostovski, G., Mitchell, A., Holland and Austin, M., *Sidewall Corrugation Lithography: Bulk fabrication of ordered nanowires, nanoribbons and nanorings*, Submitted to - Appl. Phys. Lett. 2008.

3. Kostovski, G., Mitchell, A., Holland, A., Fardin, E. and Austin, M., *Nanolithography by elastomeric scattering mask: An application of photolithographic standing waves*, Appl. Phys. Lett. 88, 133128, 2006.

4. Perentos, A., Kostovski, G. and Mitchell, A., *Polymer long-period raised rib waveguide gratings using nano-imprint lithography*, IEEE Photonics Technology Letters, 17(12), pp. 2595-2597, 2005.

Refereed Conference Proceedings

1. Kostovski, G., White, D., Mitchell, A., Austin, M., Stoddart, P. R., *Nanoimprinted Optical Fibres: Biotemplated Nanostructures for SERS Sensing*, Submitted to Australian Conference on Optical Fibre Technology (ACOFT), 2008.

2. White, D., Kostovski, G., A. Mazollini, Mitchell, A., Stoddart, P., R., Nanoimprinted *Optical Fibre for remote SERS sensing*, Submitted to International Conference on Raman Spectroscopy (ICORS), 2008.

3. Kostovski, G., White, D.J., Mitchell, A., Austin, M. and Stoddart, P.R., *Nanoimprinting on optical fiber end faces for chemical Sensing*, Nineteenth conference on Optical Fibre Sensors, Perth, April, 2008.

4. Kostovski, G., White, D.J., Mitchell, A., Austin, M. and Stoddart, P.R., *Nanoarray biotemplating: Plasmon resonances, SERS sensing and replication*, Proceedings - Tenth world congress on Biosensors, May, 2008.

5. Kostovski, G., Perentos, A., Pachoud, D., Bui, L., Holland, A., Mitchell, A. and Austin, M., *Fabrication of single-mode polymer rib waveguides by soft-imprinting*, ACOFT, Sydney, Australia, Jul 2005.

6. Holland, A. S. Balkunje, V. S. Mitchell, A. Austin, M. W. Raghunathan, M. K. Kostovski, G., *Effects of design geometry on SU8 polymer waveguides*, Proceedings - SPIE Vol. 5649(1), Smart structures, devices, and systems II, Said F. Al-Sarawi, Editor, pp. 186-194, Feb. 2005.